

ESD-TR-65-476

ESD ACCESSION LIST

ESTI Call No. AL 47765Copy No. 1 of 1 cys.A PHYSICAL LOW-CLOUD
PREDICTION MODEL

ESD RECORD COPY

RETURN TO
SCIENTIFIC & TECHNICAL INFORMATION DIVISION
(ESTI), BUILDING 1211

Joseph P. Gerrity

October 1965

433L SYSTEM PROGRAM OFFICE
ELECTRONICS SYSTEMS DIVISION
AIR FORCE SYSTEMS COMMAND
UNITED STATES AIR FORCE
L. G. Hanscom Field, Bedford, Mass.

ESSW

A00623461

Qualified users may obtain copies of this report from the Defense Documentation Center.

When U. S. Government drawings, specifications, or other data are used for any purpose other than a definitely related Government procurement operation, the Government thereby incurs no responsibility nor any obligation whatsoever, and the fact that the Government may have formulated, furnished, or in any way supplied the said drawings, specifications, or other data, is not to be regarded by implication or otherwise, or in any manner licensing the holder or any other person or corporation, or conveying any rights or permission to manufacture, use, or sell any patented invention that may in any way be related thereto.

DDC release to CFSTI is authorized.

A PHYSICAL LOW-CLOUD PREDICTION MODEL

Electronics Systems Division
Air Force Systems Command
United States Air Force
EST-TR-65-476

Joseph P. Gerrity

October 1965
7463-182

THE TRAVELERS RESEARCH CENTER, INC.
250 Constitution Plaza Hartford, Connecticut 06103

ERRATA

<u>Location</u>	<u>Error</u>	<u>Correction</u>
P. 5, line 1	Neglecting the partial derivative ...	Neglecting the derivative ... [delete the word "partial"]
P.15, Eq. (II-53)	insert minus sign in right hand side of inequality:	
	$\frac{T_h - T_i}{h - z_i} + \gamma < - \frac{u_*^2 \bar{\theta}}{4 \beta g} \left[\frac{\ln(h/z_i)}{k(h-z_i)} \right]^2$	
P.42, Fig. title	Case A: prognosis ... isotherms (°K) ...	Case A: prognosis ... isotherms (°C) ...
P.47, Fig. title	Case A: analysis of observed surface isotherms (°K) and derived 50-m wind field ...	Case A: derived 50-m wind field ... [delete first seven words]
P.111, equation on 1st line		

$$A_{\ell,m} = \frac{0.5}{Z_k - Z_i} * \sum_{k=2}^{k=K} (DZ)_K * \dots \quad A_{\ell,m} = \frac{0.5}{Z_k - Z_i} * \sum_{k=2}^{k=K} (DZ)_k * \dots$$

[Summation of (DZ)_k]

ESD-TR-65-476

A PHYSICAL LOW-CLOUD
PREDICTION MODEL

Joseph P. Gerrity

October 1965



433L SYSTEM PROGRAM OFFICE
ELECTRONICS SYSTEMS DIVISION
AIR FORCE SYSTEMS COMMAND
UNITED STATES AIR FORCE
L. G. Hanscom Field, Bedford, Mass.

FOREWORD

System 433L; project 1.0; task 1.2. This TR has been prepared for United Aircraft Corporation, East Hartford, Conn., under Subcontract No. 15107 to Contract No. AF19(628)-3437, by The Travelers Research Center, Inc., 250 Constitution Plaza, Hartford, Conn. The Research Center's publication number is 7463-182. Robert L. Houghten, Lt. Colonel, USAF, is Acting System Program Director. This report covers the period January—August, 1965, and was submitted for approval on October 6, 1965.

ABSTRACT

A physical model for the prediction of large-scale low cloudiness [ESD-TR-65-3] was modified. Results of three 12-hour forecasts (for different synoptic situations), computed with the new model, are presented.

Equations for the contact layer were derived for the forced convection, free convection, and strong inversion regimes. The requirement for upper boundary conditions is reduced; only the geostrophic wind components and upper-level cloudiness are required from a free-air model. Empirical methods were developed for computing the instrument shelter level temperature and relative humidity. The eddy diffusion coefficient for heat and water is a function of the Richardson number throughout the boundary layer. The linear geostrophic wind shear within the boundary layer is computed from the predicted temperature.

The model has not been thoroughly tested: preliminary results suggest that, given a careful analysis of routine observational data, this boundary layer model will serve operationally-meaningful diagnostic and predictive functions.

The logic used in constructing the computer program for the model is presented.

REVIEW AND APPROVAL

Publication of this technical report does not constitute Air Force approval of the report's findings or conclusions. It is published only for the exchange and stimulation of ideas.



Robert L. Houghten
Lt. Colonel, USAF
Acting System Program Director

TABLE OF CONTENTS

<u>Section</u>	<u>Title</u>	<u>Page</u>
I	INTRODUCTION	1
II	DERIVATION OF MODEL EQUATIONS	3
1.	Horizontal Equations of Motion	3
2.	The Geostrophic Wind	4
3.	The Continuity Equation	5
4.	The Heat Transfer Equation	5
5.	The Water Substance Transfer Equation	6
6.	Condensation, Evaporation, and Latent Heat Exchange	6
7.	The Coefficients of Eddy Diffusivity and Eddy Viscosity	7
8.	Boundary Conditions	7
9.	Constant Flux Hypothesis	8
10.	Contact Layer	9
11.	Surface Stress	9
12.	Geostrophic Deviation Angle	10
13.	Turbulence Regimes	11
14.	Forced Convection Relations	11
15.	Free Convection Formulas	13
16.	Determination of Regime	15
17.	Continuity of Heat Flux	16
18.	Extreme Stability	16
19.	Surface Temperature Specification	17
20.	Surface Humidity Specification	18
21.	Coordinate System and Terrain Variation	19
III	INPUT DATA ANALYSIS	23
IV	ANALYSIS OF TESTS	25
V	CONCLUSIONS AND RECOMMENDATIONS	95

<u>Section</u>	<u>Title</u>	<u>Page</u>
APPENDIX.	LOGICAL AND COMPUTATIONAL FORMULATION OF THE NUMERICAL MODEL	97
REFERENCES		133

LIST OF ILLUSTRATIONS

<u>Figure</u>	<u>Title</u>	<u>Page</u>
1	Grid network used in this study	20
2(a)	Case A, observed data: surface isobars (mb) and 700-mb contours (tens of meters) at <u>initial</u> time	33
(b)	Case A, observed data: surface isobars (mb) and 700-mb contours (tens of meters) at <u>verification</u> time	34
(c)	Case A: analysis of <u>observed</u> temperature ($^{\circ}\text{K}$) and humidity at verification time for level 500 m above terrain height	35
(d)	Case A: analysis of <u>observed</u> temperature ($^{\circ}\text{K}$) and humidity at verification time for level 1150 m above terrain height	36
(e)	Case A: analysis of <u>observed</u> temperature ($^{\circ}\text{K}$) and humidity at verification time for level 2000 m above terrain height	37
(f)	Case A: analysis of <u>predicted</u> temperature ($^{\circ}\text{K}$) and humidity at verification time for level 500 m above terrain height	38
(g)	Case A: analysis of <u>predicted</u> temperature ($^{\circ}\text{K}$) and humidity at verification time for level 1150 m above terrain height	39
(h)	Case A: analysis of <u>predicted</u> temperature ($^{\circ}\text{K}$) and humidity at verification time for level 2000 m above terrain height	40
(i)	Case A: analysis of observed surface isotherms ($^{\circ}\text{K}$) and derived 50-m wind field at verification time (arrows indicate wind direction; numbers indicate wind speed in m sec^{-1}).	41
(j)	Case A: prognosis of surface isotherms ($^{\circ}\text{K}$) and 50-m wind field valid at verification time (arrows indicate wind direction; numbers indicate wind speed in m sec^{-1}).	42
(k)	Case A: vertical cross section along grid row $M = 4$ showing predicted temperature ($^{\circ}\text{K}$) and humidity, and observed sky condition and weather (at top of figure), valid at verification time	43
(l)	Case A: vertical cross section along grid row $M = 5$ showing predicted temperature ($^{\circ}\text{K}$) and humidity, and observed sky condition and weather (at top of figure), valid at verification time	44

LIST OF ILLUSTRATIONS

<u>Figure</u>	<u>Title</u>	<u>Page</u>
2(m)	Case A: vertical cross section along grid row M = 6 showing predicted temperature ($^{\circ}\text{K}$) and humidity, and observed sky condition and weather (at top of figure), valid at verification time	45
(n)	Case A: vertical cross section along grid row M = 7 showing predicted temperature ($^{\circ}\text{K}$) and humidity, and observed sky condition and weather (at top of figure), valid at verification time	46
3	Case A: analysis of observed surface isotherms ($^{\circ}\text{K}$) and derived 50-m wind field at initial time (arrows indicate wind direction; numbers indicate wind speed in m sec^{-1})	47
4	Case A: predicted terrain-induced vertical velocity (cm sec^{-1}) at verification time	48
5	Case A: net sensible heat (Cal cm^{-2}) added to the transition layer during the forecast period	49
6	Case A: net latent heat (Cal cm^{-2}) added to the transition layer during the forecast period	50
7(a)	Case B, observed data: surface isobars (mb) and 700-mb contours (tens of meters) at <u>initial</u> time	51
(b)	Case B, observed data: surface isobars (mb) and 700-mb contours (tens of meters) at <u>verification</u> time	52
(c)	Case B: analysis of <u>observed</u> temperature ($^{\circ}\text{K}$) and humidity at verification time for level 500 m above terrain height	53
(d)	Case B: analysis of <u>observed</u> temperature ($^{\circ}\text{K}$) and humidity at verification time for level 1150 m above terrain height	54
(e)	Case B: analysis of <u>observed</u> temperature ($^{\circ}\text{K}$) and humidity at verification time for level 2000 m above terrain height	55
(f)	Case B: analysis of <u>predicted</u> temperature ($^{\circ}\text{K}$) and humidity at verification time for level 500 m above terrain height	56
(g)	Case B: analysis of <u>predicted</u> temperature ($^{\circ}\text{K}$) and humidity at verification time for level 1150 m above terrain height	57
(h)	Case B: analysis of <u>predicted</u> temperature ($^{\circ}\text{K}$) and humidity at verification time for level 2000 m above terrain height	58
(i)	Case B: analysis of observed surface isotherms ($^{\circ}\text{K}$) and derived 50-m wind field at verification time (arrows indicate wind direction; numbers indicate wind speed in m sec^{-1})	59

<u>Figure</u>	<u>Title</u>	<u>Page</u>
7(j)	Case B: prognosis of surface isotherms ($^{\circ}\text{K}$) and 50-m wind field valid at verification time (arrows indicate wind direction; numbers indicate wind speed in m sec^{-1})	60
(k)	Case B: vertical cross section along grid row $M = 4$ showing predicted temperature ($^{\circ}\text{K}$) and humidity, and observed sky condition and weather (at top of figure), valid at verification time	61
(l)	Case B: vertical cross section along grid row $M = 5$ showing predicted temperature ($^{\circ}\text{K}$) and humidity, and observed sky condition and weather (at top of figure), valid at verification time	62
(m)	Case B: vertical cross section along grid row $M = 6$ showing predicted temperature ($^{\circ}\text{K}$) and humidity, and observed sky condition and weather (at top of figure), valid at verification time	63
(n)	Case B: vertical cross section along grid row $M = 7$ showing predicted temperature ($^{\circ}\text{K}$) and humidity, and observed sky condition and weather (at top of figure), valid at verification time	64
8	Case B: south-to-north vertical cross section of temperature ($^{\circ}\text{K}$) and humidity along the coordinate line $L = 5$ (solid line indicates frontal position)	65
9	Case B: initial and predicted temperature structure at grid point $L = 9, M = 6$, and observed (at verification time) structure at a nearby radiosonde station	66
10	Case B: initial and predicted temperature structure at grid point $L = 6, M = 6$, and observed (at verification time) structure at a nearby radiosonde station	67
11	Case B: initial and predicted temperature structure at grid point $L = 5, M = 7$, and observed (at verification time) structure at a nearby radiosonde station	68
12	Case B: initial and predicted temperature structure at grid point $L = 7, M = 7$, and observed (at verification time) structure at a nearby radiosonde station	69
13	Case B: initial and predicted temperature structure at grid point $L = 2, M = 8$, and observed (at verification time) structure at a nearby radiosonde station	70
14	Case B: temperature and dew-point observations at radiosonde station 226 for initial (fine lines) and final (heavy lines) times of the forecast, and their values (medium lines) predicted at the nearby grid point	71

<u>Figure</u>	<u>Title</u>	<u>Page</u>
15(a)	Case C: observed data: surface isobars (mb) and 700-mb contours (tens of meters) at <u>initial</u> time	72
(b)	Case C: observed data: surface isobars (mb) and 700-mb contours (tens of meters) at <u>verification</u> time	73
(c)	Case C: analysis of <u>observed</u> temperature ($^{\circ}\text{K}$) and humidity at verification time for level 500 m above terrain height	74
(d)	Case C: analysis of <u>observed</u> temperature ($^{\circ}\text{K}$) and humidity at verification time for level 1150 m above terrain height	75
(e)	Case C: analysis of <u>observed</u> temperature ($^{\circ}\text{K}$) and humidity at verification time for level 2000 m above terrain height	76
(f)	Case C: analysis of <u>predicted</u> temperature ($^{\circ}\text{K}$) and humidity at verification time for level 500 m above terrain height	77
(g)	Case C: analysis of <u>predicted</u> temperature ($^{\circ}\text{K}$) and humidity at verification time for level 1150 m above terrain height	78
(h)	Case C: analysis of <u>predicted</u> temperature ($^{\circ}\text{K}$) and humidity at verification time for level 2000 m above terrain height	79
(i)	Case C: analysis of observed surface isotherms ($^{\circ}\text{K}$) and derived 50-m wind field at verification time (arrows indicate wind direction; numbers indicate wind speed in m sec^{-1})	80
(j)	Case C: prognosis of surface isotherms ($^{\circ}\text{K}$) and 50-m wind field valid at verification time (arrows indicate wind direction; numbers indicate wind speed in m sec^{-1})	81
(k)	Case C: vertical cross section along grid row $M = 4$ showing predicted temperature ($^{\circ}\text{K}$) and humidity, and observed sky condition and weather (at top of figure), valid at verification time	82
(l)	Case C: vertical cross section along grid row $M = 5$ showing predicted temperature ($^{\circ}\text{K}$) and humidity, and observed sky condition and weather (at top of figure), valid at verification time	83
(m)	Case C: vertical cross section along grid row $M = 6$ showing predicted temperature ($^{\circ}\text{K}$) and humidity, and observed sky condition and weather (at top of figure), valid at verification time	84
(n)	Case C: vertical cross section along grid row $M = 7$ showing predicted temperature ($^{\circ}\text{K}$) and humidity, and observed sky condition and weather (at top of figure), valid at verification time	85
16	Case C: observed initial-time and predicted temperature at grid-point $L = 10$, $M = 7$, and observed verification-time temperature at radiosonde station 518	86

<u>Figure</u>	<u>Title</u>	<u>Page</u>
17	Case C: regions reporting broken or overcast low cloudiness and precipitation at verification time	87
18	Case C: composite of <u>predicted</u> humidity for the 500-, 1150-, and 2000-m levels	88
19	Case C: composite of <u>observed</u> humidity for the 500-, 1150-, and 2000-m levels at verification time	89
20	Case C: initial and predicted temperature at grid point L = 6, M = 6, and observed verification-time temperature at radiosonde station 425	90
21	Case C: initial and predicted temperature at grid point L = 5, M = 3, and observed verification-time temperature at radiosonde station 311	91
22	Case C: initial and predicted temperature at grid point L = 5, M = 7, and observed verification-time temperature at radiosonde station 429	92
23	Case C: initial and predicted temperature at grid point L = 7, M = 7, and observed verification-time temperature at radiosonde station 520	93
24	Case C: initial and predicted temperature at grid point L = 7, M = 4, and observed verification-time temperature at radiosonde station 317	94
25	Major computational steps for numerical model	107
26	Logic and computations	128

LIST OF TABLES

<u>Table</u>	<u>Title</u>	<u>Page</u>
I	Map scale factor at grid points in Fig. 1	21
II	Elevation of terrain (in meters) above mean sea level at various grid points given in Fig. 1	21
III	Surface roughness parameter (in centimeters) at the grid points shown in Fig. 1	22
IV	Comparison of temperature prediction errors (°K) the model versus persistence	30
V	Average absolute error in temperature	31
VI	Definitions	100

SECTION I

INTRODUCTION

It is frequently noted that physical atmospheric prediction models rarely have merited designation as weather prediction models. Empirical investigations have shown that the interpretation of even an accurate circulation prediction in terms of weather conditions is not a trivial problem.

Some ten years ago, Smagorinsky and Collins [26] advanced a procedure for utilizing a two-parameter, quasi-geostrophic model for predicting precipitation amounts. The hypothesis that diabatic effects might have a significant role in cases of strong, baroclinic development led many investigators to develop physical prediction models that incorporated the condensation process more or less along the lines suggested by Smagorinsky and Collins. Gambo [11] has indicated recently that diabatic effects, while they may not lead to rapid deepening, can be very significant in the maintenance of accurate phase relations in multi-level circulation models. At the present time, neither the Air Force nor the National Meteorological Center (NMC) employs physical prediction models that incorporate the diabatic processes which are intimately related to weather phenomena. In general circulation research, the utilization of diabatic models is clearly essential, and in the light of the requirement for long-range weather predictions, operational prediction will have to be reoriented to the utilization of diabatic physical prediction models.

The region of the troposphere which is most greatly influenced by diabatic processes is the planetary boundary layer. Because most horizontally-extensive low cloudiness is confined to this layer, it appears desirable to approach the problem of the prediction of synoptic-scale low cloudiness through the use of a reasonably complete physical model of the boundary layer. The model which is presented in this paper is an effort in this direction.

Some work has been done previously in the formulation of subsynoptic-scale physical models of the boundary layer, notably by Fisher [8] and Estoque [7]. Their work could not be directly extended because of their requirement for non-routine meteorological observations. It was necessary, therefore, to consider the feasibility of constructing a meaningful model which would utilize only routine observational data but yet incorporate the significant physical processes.

A number of suggestions made to the writer by Drs. Árnason and Pandolfo of The Travelers Research Center, Inc. (TRC), Prof. Davidson of New York University, and Prof. Blackadar of Pennsylvania State University were helpful in indicating the extent to which certain physical approximations might be justified. Foremost among the modeling simplifications adopted in our work are:

- (a) the use of a static-diagnostic horizontal-wind equation,
- (b) the use of an empirical surface temperature prediction technique,
- (c) the use of empirical formulas for the stress and geostrophic deviation angle,
- (d) the neglect of radiative heat flux divergence,
- (e) the use of the constant-flux contact layer,
- (f) the use of an empirical surface humidity prediction technique.

The research presented in this paper was essentially oriented to a specific application, i.e., low-cloud prediction. A broader view of the framework within which this modeling approach may be applied has been indicated above, but has not yet been pursued.

After development of the model to its present form, an extensive period of careful testing is desirable. From a practical viewpoint, these tests should indicate the relative usefulness of the model in comparison with other methods for low-cloud prediction. An equally useful purpose for such tests would be to unveil the hidden characteristics of the model atmosphere. Within the scope of the effort reported here, we have been able to conduct only a few tests of the model.

SECTION II

DERIVATION OF MODEL EQUATIONS

The equations governing the model atmosphere are written in Cartesian coordinates. The horizontal coordinates, x and y , are rectangular coordinates on a polar stereographic map projection. Because the pertinent physical boundary is the surface of the ground or ocean, and not a fictitious mean-sea-level, we chose the height above the terrain as the vertical coordinate, Z .

The planetary boundary layer is decomposed into two sublayers. A shallow layer, denoted as the contact layer, occupies the region between $Z = 0$ and $Z = h$ (50 m). The bulk of the boundary layer is termed the transition layer. It has been assumed that the upper boundary of the planetary boundary layer may be set at 2 km above the terrain height.

1. Horizontal Equations of Motion

We assume that the horizontal wind components, u and v , are governed by the balance equations,

$$\frac{\partial^2 u}{\partial Z^2} = - 2 \alpha^2 (v - v_g) \quad (\text{II-1})$$

$$\frac{\partial^2 v}{\partial Z^2} = + 2 \alpha^2 (u - u_g) \quad (\text{II-2})$$

where α , the square root of the ratio of the Coriolis parameter to twice the eddy viscosity, is assumed to be independent of Z , and u_g and v_g , the geostrophic wind components, are assumed to be linear functions of Z . Under the boundary conditions,

$$\begin{aligned} u &\rightarrow u_g \\ v &\rightarrow v_g \end{aligned} \quad \text{as } Z \rightarrow \infty \quad (\text{II-3})$$

and

$$\begin{aligned} u &= U \\ v &= V \end{aligned} \quad \text{at } Z = h \quad (\text{II-4})$$

the solutions of Eqs. (II-1) and (II-2) may be given by

$$u = u_g^h + e^{-\alpha(Z-h)} \{ (U - u_g^h) \cos [\alpha(Z-h)] + (V - v_g^h) \sin [\alpha(Z-h)] \} \quad (\text{II-5})$$

$$v = v_g^h + e^{-\alpha(Z-h)} \{ (V - v_g^h) \cos [\alpha(Z-h)] - (U - u_g^h) \sin [\alpha(Z-h)] \} \quad (\text{II-6})$$

in which u_g^h and v_g^h are the values of u_g and v_g at $Z = h$. The values of U and V required in Eqs. (II-5) and (II-6) are obtained from formulas derived subsequently.

2. The Geostrophic Wind

The geostrophic wind is assumed to be a linear function of Z :

$$u_g = u_g^H + B (H-Z), \quad (\text{II-7})$$

$$v_g = v_g^H + C (H-Z). \quad (\text{II-8})$$

Using the procedure outlined in Haurwitz [14], one may relate B and C to the horizontal temperature gradient within the transition layer. Taking appropriate account of the terrain variation, we may derive the following relations:

$$u_g = u_g^H + \left[\frac{H-Z}{H-h} \right] \{ (u_g^H - \tilde{u}) \left(\frac{T_h - T_H}{T_H} \right) - \frac{\sigma g T_h}{f} \int_h^H \frac{\partial}{\partial y} \left(\frac{1}{T} \right) dZ \}, \quad (\text{II-9})$$

$$v_g = v_g^H + \left[\frac{H-Z}{H-h} \right] \{ (v_g^H - \tilde{v}) \left(\frac{T_h - T_H}{T_H} \right) + \frac{\sigma g T_h}{f} \int_h^H \frac{\partial}{\partial x} \left(\frac{1}{T} \right) dZ \}, \quad (\text{II-10})$$

in which

$$\tilde{u} = - \frac{\sigma g}{f} \frac{\partial E}{\partial y}, \quad (\text{II-11})$$

$$\tilde{v} = \frac{\sigma g}{f} \frac{\partial E}{\partial x}, \quad (\text{II-12})$$

and u_g^H, v_g^H are the geostrophic wind components at $Z = H$, T_h and T_H are the temperatures at $Z = h$ and $Z = H$, E is the height of the terrain above mean sea level and σ is the map scale factor.

3. The Continuity Equation

Neglecting the partial derivative of air density in the continuity equation leads to the simplified equation,

$$\frac{\partial w}{\partial z} = -\sigma \left(\frac{\partial u}{\partial x} + \frac{\partial v}{\partial y} \right), \quad (\text{II-13})$$

Since w must vanish at $Z = 0$ due to the viscosity of the air, we may, to good approximation, solve Eq. (II-9) using the boundary condition, $w = 0$ at $Z = h$.

$$w = -\sigma \int_h^Z \left(\frac{\partial u}{\partial x} + \frac{\partial v}{\partial y} \right) dZ. \quad (\text{II-14})$$

Due to our choice of coordinate system, the vertical velocity, w , differs from the velocity normal to surfaces which parallel mean-sea-level. If the latter is denoted by ω , we may write,

$$\omega = w + \hat{w}, \quad (\text{II-15})$$

with

$$\hat{w} = \sigma \left[u \frac{\partial E}{\partial x} + v \frac{\partial E}{\partial y} \right]. \quad (\text{II-16})$$

4. The Heat Transfer Equation

The first law of thermodynamics, the ideal gas law, and the hydrostatic equation may be combined to derive a heat transfer equation,

$$\begin{aligned} \frac{dT}{dt} = \frac{RT}{C_p p} \frac{dp}{dt} + \frac{\partial}{\partial Z} \left\{ K_H \left[\frac{\partial T}{\partial Z} + \frac{g}{C_p T} \right] \right\} \\ + \frac{g}{C_p T} K_H \left[\frac{\partial T}{\partial Z} + \frac{g}{C_p T} \right] + \left(\frac{dT}{dt} \right)_w \end{aligned} \quad (\text{II-17})$$

where

C_p	is the specific heat of air at constant pressure
R	is the gas constant for dry air
p	is the air pressure
T	is the air temperature
K_H	is the eddy conductivity
g	is the gravitational constant
$\left(\frac{dT}{dt} \right)_w$	is the heating due to water substance phase changes

We simplify Eq. (II-12) by the approximation,

$$\frac{RT}{C_p} \frac{dp}{dt} = - \frac{g}{C_p} (w + \hat{w}) \quad (\text{II-18})$$

and by neglecting the third term on the right hand side of Eq. (II-17). The resulting equation is

$$\begin{aligned} \frac{\partial T}{\partial t} = & - \sigma \left[u \frac{\partial T}{\partial x} + v \frac{\partial T}{\partial y} \right] - w \left[\frac{\partial T}{\partial Z} + \frac{g}{C_p} \right] \\ & - \frac{g}{C_p} \hat{w} + \frac{\partial}{\partial Z} \left\{ K_H \left[\frac{\partial T}{\partial Z} + \frac{g}{C_p} \right] \right\} + \left(\frac{dT}{dt} \right)_w \end{aligned} \quad (\text{II-19})$$

5. The Water Substance Transfer Equation

The ratio of the water vapor density to the total density of the mixture of air, water vapor, and liquid water is defined as the specific humidity and denoted by q . We similarly define the specific moisture, r , as the ratio of water substance (vapor and liquid) density to the density of the mixture. When precipitation is omitted from consideration, we may write the following equations for q and r .

$$\frac{\partial r}{\partial t} = - \sigma \left[u \frac{\partial r}{\partial x} + v \frac{\partial r}{\partial y} \right] - w \frac{\partial r}{\partial Z} + \frac{\partial}{\partial Z} \left[K_v \frac{\partial r}{\partial Z} \right] \quad (\text{II-20})$$

$$\frac{\partial q}{\partial t} = - \sigma \left[u \frac{\partial q}{\partial x} + v \frac{\partial q}{\partial y} \right] - w \frac{\partial q}{\partial Z} + \frac{\partial}{\partial Z} \left[K_v \frac{\partial q}{\partial Z} \right] - \left(\frac{dq}{dt} \right)_c \quad (\text{II-21})$$

where K_v is the eddy diffusivity for water vapor and liquid water. The approximation that both vapor and droplets follow the air motion is convenient and in accord with observations [21]. $\left(\frac{dq}{dt} \right)_c$ represents the rate of conversion of vapor to liquid in conversion of vapor to liquid in condensation.

6. Condensation, Evaporation, and Latent Heat Exchange

In the heat transfer equation and the water vapor transfer equation, source terms appear for which a computational procedure is required. We have adopted the method used by Fisher and Caplan [8] modified after the fashion suggested by McDonald [22]. In our technique, we use a standard pressure–height relationship to provide the air pressure value needed in the computation of the saturation value of specific humidity. This relation is given by

$$p = [1.013 - 1.065 \times 10^{-6} (Z + E)] \quad (\text{II-22})$$

in which p is in bars, and Z and E are in cm. The saturation specific humidity, q_s , at a temperature, $T(^{\circ}\text{K})$, and at a height, Z , is given to good approximation by

$$q_s = \frac{3.8 \times 10^{-3}}{[1.013 - 1.065 \times 10^{-6} (Z+E)]} \exp \left\{ 17.25 \left[\frac{T-273}{T-35.7} \right] \right\} \quad (\text{II-23})$$

7. The Coefficients of Eddy Diffusivity and Eddy Viscosity

The computational formulas used to compute the coefficients of eddy diffusivity and eddy viscosity within the transition layer are extensions of formulas which have been derived from similarity theories for the contact layer. Richardson's number, R_i , is defined as

$$R_i = \frac{g}{\Theta} \frac{\partial \Theta}{\partial Z} \bigg/ \left| \frac{\partial \vec{V}}{\partial Z} \right|^2 \quad (\text{II-24})$$

The free and forced regimes of turbulent convection are discriminated by the use of a critical value of R_i . When $R_i \leq -0.03$ we assume that free convection exists; when $R_i > -0.03$ we assume that forced convection exists.

The eddy diffusivities for heat and water (both vapor and liquid) are taken, to be equal. If free convection prevails, we write,

$$K_v = K_H = \lambda Z^2 \left| \frac{g}{\Theta} \frac{\partial \Theta}{\partial Z} \right|^{1/2} \quad (\text{II-25})$$

If forced convection prevails, we write,

$$K_v = K_H = [kZ (1-\beta R_i)]^2 \left| \frac{\partial \vec{V}}{\partial Z} \right|. \quad (\text{II-26})$$

The values computed from these formulas are adjusted to lie between 10^4 and 10^6 $\text{cm}^2 \text{sec}^{-1}$. If $R_i > 0$ and $\left| \frac{\partial \vec{V}}{\partial Z} \right| = 0$, or $(1-\beta R_i) \leq 0$, we set the coefficients to the minimum value.

The coefficient of eddy viscosity is assumed to be invariant with height and equal to the value computed for it from the contact-layer equations at $Z = h$.

8. Boundary Conditions

The equations presented above require for solution the specification of boundary and initial conditions. The initial conditions can be specified from observational data throughout the region of integration. Lateral boundary conditions are required for those

equations involving horizontal advection terms. These time-dependent conditions are needed only on those portions of the boundary through which the horizontal flow is directed into the region of integration. Errors in the specification of conditions on these boundaries will propagate into the interior of the region at approximately the speed of the air.

Boundary conditions are also required for the heat and water transfer equations on the vertical boundaries. On the lower boundary we specify the eddy flux of heat and water substance. The computation of these boundary values is carried out using the formulas derived subsequently through consideration of the properties of the contact layer. On the upper boundary q , T and r are computed from simplified forms of the basic equations. The simplification involves the neglect at this boundary of the convergence of the eddy flux.

The vertical boundary conditions needed for the complete solution of the horizontal wind equations are, first, the specification of the temporal variation of u_g^H and v_g^H , and second, the specification of U and V at $Z=h$. The first conditions may be obtained from forecasts of the geopotential made by dynamical-prediction models at appropriate pressure levels. U and V are computed from formulas derived using the contact layer equations.

9. Constant Flux Hypothesis

The rate at which meteorological properties are transferred by eddy motions within the region near the ground is so large (at least at certain times) that it is quite clear from standard observations that this eddy transport must be very nearly non-divergent. For example, the eddy heat flux has been measured to be several hundred milli-langleys per minute. If that amount of heat transfer were to converge within a layer of a few hundred feet thickness, it would produce temperature changes throughout the layer of several tens of degrees (centigrade) in an hour. Detailed measurements of the eddy transport of heat, vapor, and momentum have been made utilizing instruments mounted on towers at various heights. To the accuracy obtainable with these instruments, it has been found [19] that the convergence of the eddy flux within a depth of 100 meters is usually less than ten percent of the total flux.

Based upon this empirical evidence, it has been found useful to employ the approximation that the eddy flux of heat, vapor, and momentum is constant throughout the layer

in contact with the ground surface. The layer is referred to as the "contact layer" in this paper.

10. Contact Layer

The momentum, heat and vapor fluxes are assumed to be non-divergent within a layer of 50 m thickness in contact with the Earth's surface. The value of the temperature and specific humidity are computed over land at the level of the instrument shelter following the method outlined in Sections 19 and 20. The wind speed is assumed to vanish at the level of the surface roughness. The stress acting at the surface is estimated from the surface Rossby number and the static stability using the empirical analysis of Lettau [17] and Blackadar [3]. The mixing coefficients are computed using the appropriate formulas suggested by the theories of Monin [23] and Priestley [25]. The eddy Prandtl number is taken to be a constant: $K_H = K_M$, in forced convection, and $K_H = 1.3 K_M$, in free convection. When free convection is indicated to prevail in the contact layer, we continue to utilize the forced convection wind profile between the surface roughness height and 1 m. A minus 1/3 power law applies throughout the remainder of the contact layer.

The role of the contact layer within the model is to provide lower boundary conditions for the equations governing the model atmosphere in the deeper transition layer. For temperature and specific humidity, we compute the eddy flux within the contact layer and use this quantity as a boundary condition. For the wind equations, we use the wind profile equations to specify the wind speed and the angle of geostrophic deviation at the base of the transition layer. We assume that no eddy flux of liquid water occurs within the contact layer.

11. Surface Stress

The friction velocity, u_* , is related to the surface stress τ_0 , and the air density, ρ , by the expression

$$|\tau_0| = \rho u_*^2 \quad (\text{II-27})$$

Lettau [17] has shown that if one defines a geostrophic drag coefficient, C , by

$$C = u_* / G \quad (\text{II-28})$$

in which G is the surface geostrophic wind speed, then an empirical relationship between C and the surface Rossby number, R_0 , may be derived from observational data. R_0 is defined in terms of G , the Coriolis parameter, f , and the surface roughness, Z_0 , by

$$R_0 = G / (fZ_0). \quad (\text{II-29})$$

In Lettau's analysis, u_* was evaluated for neutral stratification. When the temperature lapse rate departs from neutral, systematic departures from the previous estimates of C occur. For lapse stratification, the new drag coefficient is about twenty percent greater; for moderately strong inversion conditions, the new drag coefficient is some twenty percent smaller.

Using the data presented in Blackadar's paper [3], we obtained, by least-squares fitting, the relation,

$$u_{*n} = G(0.07625 - 0.00625 \log R_0). \quad (\text{II-30})$$

The subscript, n , indicates that this estimate is appropriate for neutral conditions. According to Blackadar, some deviation of u_* about the value given in the equation above can be attributed to the presence of a geostrophic wind-shear within the boundary layer. The fitted relation [Eq. (II-30)] agrees very closely with Lettau's analysis [17, Fig. 3, p, 246].

12. Geostrophic Deviation Angle

The angle of deviation between the surface geostrophic wind and the wind in the contact layer was shown to be a function of the surface Rossby number, R_0 , by Blackadar [3]. Using the method of least squares we fitted the following expression to his data;

$$\psi = a [\log R_0]^2 + b \log R_0 + c \quad (\text{II-31})$$

where ψ is the deviation angle in degrees and the logarithm is to the base 10. The coefficients were computed to be,

$$a = 0.625$$

$$b = -12.750$$

$$c = 80.625$$

ψ varies between 32.5° for $R_0 = 10^5$ and 15.6° for $R_0 = 10^{10}$.

13. Turbulence Regimes

We have used the expressions forced and free convection. In forced convection, both inertial and buoyancy forces act to promote turbulent eddying of the air. In free convection, buoyancy forces are alone significant.

At all times in the real atmosphere there is some air motion and, as a consequence of viscosity, there must always be significant inertial influence present close to the air-ground interface. With strong insolation, it is quite common under inactive synoptic conditions to find very strong thermal lapse conditions near the ground. In these cases, the role of the buoyancy forces may dominate in the excitation and maintenance of turbulent heat exchange, but only at some distance above the interface.

We have found it to be necessary to allow for the occurrence of the free convective regime within the model. Within the contact layer, the transition to free convection is assumed to occur throughout its depth when the Richardson's number reaches a value near -0.03 [25].

14. Forced Convection Relations

Under forced convective conditions, Monin's similarity theory [23] may be shown [24] to be consistent with the following expression for the mixing coefficient, K,

$$K = [kZ (1-\beta R_i)]^2 \frac{\partial S}{\partial Z} \quad (\text{II-32})$$

where

k is von Karman's constant

Z is height

β is an empirical constant

R_i is Richardson's number

S is the wind speed

In the derivation of this expression, the mixing coefficient was assumed to be identical for both heat and momentum.

The assumption of constant flux may be expressed in the equations,

$$-\frac{H}{C_p \rho} = K \frac{\partial \Theta}{\partial Z} = u_* \Theta_* , \quad (\text{II-33})$$

$$-\frac{Q}{\rho} = K \frac{\partial q}{\partial Z} = u_* q_*, \quad (\text{II-34})$$

$$\frac{\tau}{\rho} = K \frac{\partial S}{\partial Z} = u_*^2 \quad (\text{II-35})$$

where

- H is the eddy heat flux
- C_p is specific heat at constant pressure of air
- ρ is the air density
- Θ is the potential temperature
- u_* is the friction velocity
- Θ_* is a constant with dimensions of temperature
- Q is the vapor flux
- q is the specific humidity
- q_* is a dimensionless constant (gm/gm)

Using the approximation

$$\frac{\partial \Theta}{\partial Z} = \frac{\partial T}{\partial Z} + \gamma \quad (\text{II-36})$$

where γ is the dry-adiabatic lapse rate, and the boundary conditions,

$$\begin{aligned} q &= q_i & \text{at} & \quad Z = Z_i, \\ T &= T_i & \text{at} & \quad Z = Z_i, \\ S &= 0 & \text{at} & \quad Z = Z_0, \end{aligned} \quad (\text{II-37})$$

we may integrate the constant flux equations to obtain

$$S(Z) = \frac{u_*}{k} \ln \left(\frac{Z}{Z_0} \right) + \frac{\Theta_* \beta g}{\bar{\Theta} u_*} (Z - Z_0), \quad (\text{II-38})$$

$$T(Z) = T_i - \gamma (Z - Z_i) + \frac{\Theta_*}{k} \ln \left(\frac{Z}{Z_i} \right) + \frac{\beta g \Theta_*^2}{\bar{\Theta} u_*^2} (Z - Z_i) \quad (\text{II-39})$$

$$q(Z) = q_i + \frac{q_*}{k} \ln \left(\frac{Z}{Z_i} \right) + \frac{\beta g q_* \Theta_*}{\bar{\Theta} u_*^2} (Z - Z_i) \quad (\text{II-40})$$

in which $\bar{\Theta}$ is the mean temperature of the layer, which is taken to be a constant.

If, at the top of the contact layer, the values of T and q , say T_h and q_h , are known, we may solve the profile equations for Θ_* and q_* . Using the temperature profile, one has a quadratic equation in Θ_* . Of the two roots, the correct value for neutral stratification is given by only one root,

$$\Theta_* = \frac{-u_*^2 \bar{\Theta} \ln (h/Z_i)}{2\beta g k(h - Z_i)} \left[1.0 - \left\{ 1.0 + \frac{4\beta g}{u_*^2 \bar{\Theta}} \left[\frac{T_h - T_i}{h - Z_i} + \gamma \right] \right. \right. \\ \left. \left. \left[\frac{k(h - Z_i)}{\ln (h/Z_i)} \right]^2 \right\}^{1/2} \right] \quad (\text{II-41})$$

From the profile equation for q , one easily obtains the solution for q_*

$$q_* = (q_h - q_i) / \left(\frac{\ln [h/Z_i]}{k} + \frac{\beta g \Theta_*}{u_*^2 \bar{\Theta}} [h - Z_i] \right) \quad (\text{II-42})$$

The wind speed at the top of the contact layer, S_h , may be readily evaluated from the wind speed profile equation,

$$S_h = \frac{u_*}{k} \ln \left(\frac{h}{Z_0} \right) + \frac{\Theta_* \beta g}{\bar{\Theta} u_*} (h - Z_0) \quad (\text{II-43})$$

15. Free Convection Formulas

Priestley's similarity theory for free convection [25] yields the following expression for the mixing coefficient for heat,

$$K_H = \lambda Z^2 \left[\frac{g}{\bar{\Theta}} \left| \frac{\partial T}{\partial Z} + \gamma \right| \right]^{1/2} \quad (\text{II-44})$$

in which λ is an empirical constant.

Utilizing this expression in the equation for constant heat flux, one obtains,

$$- \lambda Z^2 \left(\frac{g}{\bar{\Theta}} \right)^{1/2} \left| \frac{\partial T}{\partial Z} + \gamma \right|^{3/2} = u_* \Theta_* \quad (\text{II-45})$$

This expression may be integrated using the boundary condition, $T = T_i$ at $Z = Z_i$, to get the profile formula

$$T(Z) = T_i - \gamma (Z - Z_i) - \frac{3 u_* \Theta_*}{\lambda^{2/3} |u_* \Theta_*|^{1/3}} \left(\frac{\bar{\Theta}}{g} \right)^{1/3} \left[Z^{-1/3} - Z_i^{-1/3} \right] \quad (\text{II-46})$$

If one assumes that the mixing coefficient for water vapor is identical to that for heat, the specific humidity profile equation becomes,

$$q(Z) = q_i - \frac{3u_*q_*}{\lambda^{2/3} |u_*\Theta_*|^{1/3}} \left(\frac{\bar{\Theta}}{g} \right)^{1/3} \left[Z^{-1/3} - Z_i^{-1/3} \right] \quad (\text{II-47})$$

Under the assumption that the mixing coefficient for heat is thirty percent larger than that for momentum, one may derive a wind profile for free convection, vis.,

$$S(Z) = - \frac{3.9u_*^2}{\lambda^{2/3} |u_*\Theta_*|^{1/3}} \left(\frac{\bar{\Theta}}{g} \right)^{1/3} \left[Z^{-1/3} - Z_0^{-1/3} \right] \quad (\text{II-48})$$

We have adjusted this equation by assuming that a near-neutral forced convective regime exists between Z_0 and $Z_0 + 1$ m. This yields the wind profile,

$$S(Z) = \frac{u_*}{k} \ln \left(\frac{Z_0 + 1 \text{ m}}{Z_0} \right) - \frac{3.9u_*^2}{\lambda^{2/3} |u_*\Theta_*|^{1/3}} \left(\frac{\bar{\Theta}}{g} \right)^{1/3} \left[Z^{-1/3} - (Z_0 + 1 \text{ m})^{-1/3} \right] \quad (\text{II-49})$$

Now if the temperature and specific humidity are known at $Z = h$, the top of the contact layer, we may solve the profile equations for Θ_* and q_* ,

$$\Theta_* = - \left\{ \frac{\lambda^{2/3}}{3u_*} \left(\frac{g}{\bar{\Theta}} \right)^{1/3} \frac{(h - Z_i)}{(h^{-1/3} - Z_i^{-1/3})} \left[\frac{T_h - Z_i}{h - Z_i} + \gamma \right] \right\}^{3/2} \quad (\text{II-50})$$

$$q_* = - (q_h - q_i) / \left\{ \frac{3u_*}{\lambda^{2/3} |u_*\Theta_*|^{1/3}} \left(\frac{\bar{\Theta}}{g} \right)^{1/3} \left[h^{-1/3} - Z_i^{-1/3} \right] \right\} \quad (\text{II-51})$$

The wind speed at the top of the contact layer is readily computed to be given by

$$S(h) = \frac{u_*}{k} \ln \left(\frac{Z_0 + 1 \text{ m}}{Z_0} \right) - \frac{3.9u_*^2}{\lambda^{2/3} |u_*\Theta_*|^{1/3}} \left(\frac{\bar{\Theta}}{g} \right)^{1/3} \left[h^{-1/3} - (Z_0 + 1 \text{ m})^{-1/3} \right] \quad (\text{II-52})$$

16. Determination of Regime

The two sets of results derived above may be applied, provided that the appropriate convective regime is determined. We discovered that the forced convection formula for Θ_* , which involves a radical, can be used to determine the character of the regime. We note that the quantity Θ_* will be complex if

$$\frac{T_h - T_i}{h - Z_i} + \gamma < \frac{u_*^2 \bar{\Theta}}{4\beta g} \left[\frac{\ln(h/Z_i)}{k(h - Z_i)} \right]^2 \quad (\text{II-53})$$

Upon utilizing the forced convection heat flux, evaluated at a temperature difference for which the radical vanishes in the formula for Θ_* , we can evaluate the Richardson's number (R_i) as a function of height, and the parameter, β . Using $h = 50$ m, $Z_i = 1$ m, $\beta = 2.0$, and $Z = 1.5$ m, we found [12] that $R_i = -0.032$. This value agrees well with the critical Richardson's number quoted by Priestley [25]. We concluded that the satisfaction of the inequality above was a sufficient condition for deciding that a free convection regime prevailed.

A further test of regime was subsequently developed from the formula for the forced convection mixing coefficient evaluated at the top of the contact layer,

$$K_h = h k u_* / \left[1.0 + \frac{\beta g k h u_* \Theta_*}{\bar{\Theta} u_*^3} \right] \quad (\text{II-54})$$

This is equivalent to

$$K_h = k u_* h (1 - \beta R_i) \quad (Z = h) \quad (\text{II-55})$$

and it is clear that the factor $(1 - \beta R_i)$ must be positive. This leads to a condition

$$1.0 + \frac{\beta g k h u_* \Theta_*}{\bar{\Theta} u_*^3} > 0 \quad (\text{II-56})$$

The existence of this added condition reflects the possible existence of a mixture of free and forced convective regimes within the contact layer of a more complex nature than that indicated in our treatment of the wind profile in free convection. The description of this situation is beyond the scope of our model. We have, of course, been forced to recognize the constraint imposed by the last inequality, which is more stringent than the inequality given earlier. In practice, we have gone a step further and employed the free

convection formulas in lapse conditions whenever the free convection heat flux exceeds that given by the forced convection formula.

17. Continuity of Heat Flux

It seemed reasonable to require the heat flux to be continuous at the critical Richardson's number. We found [12] that this condition was adequate to relate the value of the parameter, λ , to the value of β . The resulting expression is of the form

$$\lambda = k^2 c \sqrt{\beta} \quad (\text{II-57})$$

The symbol, c , stands for a constant dependent solely upon the levels Z_i and h .

Using $k = 0.38$, we found

$$\lambda = 0.85 \sqrt{\beta} \quad (\text{II-58})$$

For $\beta = 2.0$, $\lambda = 1.2$, a value between those given for this parameter by Priestley [25] and Dyer [6].

18. Extreme Stability

In addition to the limit on the applicability of the Monin forced convection formulas in lapse conditions indicated above, we note that the formulas become invalid when the Richardson number becomes larger than β^{-1} . In this case, we assume that the quantities Θ_* and q_* may be computed using the constant minimal value for the mixing coefficient, K_{\min} ($\sim 10^2 \text{ cm}^2 \text{ sec}^{-1}$).

In this way, one obtains,

$$\Theta_* = \frac{K_{\min}}{u_*} \left[\frac{T_h - T_i}{h - Z_i} + \gamma \right] \quad (\text{II-59})$$

and

$$q_* = \frac{K_{\min}}{u_*} \left[\frac{q_h - q_i}{h - Z_i} \right] \quad (\text{II-60})$$

To compute the wind speed at $Z = h$, we assume that the wind is a fixed fraction of the surface geostrophic wind speed, G ,

$$S(h) = 0.176 G. \quad (\text{II-61})$$

The constant (0.176) was estimated from the "Ekman Spiral" using $K = 10^4 \text{ cm}^2 \text{ sec}^{-1}$, $f = 10^{-4} \text{ sec}^{-1}$, and the assumption that the wind vanishes at $Z = 0$ and becomes geostrophic as $Z \rightarrow \infty$.

19. Surface Temperature Specification

By surface temperature, we mean air temperature measured within an instrument shelter located 1.22 m above the ground. In the case of points located over the ocean, we consider the sea surface temperature to be the appropriate surface temperature.

The temporal variation of the surface temperature over the land must be computed within the model. This variation can be attributed to four physical processes: divergence of radiative heat flux, divergence of eddy heat flux, thermal advection, and latent heat exchange. In an effort to evaluate the influence of the first two processes, we made use of an empirical technique for specifying the temporal variation of surface temperature. This technique, developed by Bryan [5], involves the use of the equation

$$\frac{\partial}{\partial t} T(t) + b_1 T(t) = b_0 + b_2 S(t) + b_3 r(t) \quad (\text{II-62})$$

in which

$$\begin{aligned} S(t) &= \sin \delta \sin \varphi - \cos \delta \cos \varphi \cos \frac{\pi t}{12} & (R \leq t \leq S) \\ S(t) &= 0 & (\text{otherwise}) \end{aligned} \quad (\text{II-63})$$

$$\begin{aligned} r(t) &= (\partial/\partial t) S(t) = \lambda/12 \cos \delta \cos \varphi \sin \frac{\pi t}{12} & (R \leq t \leq 12) \\ r(t) &= 0 & (\text{otherwise}) \end{aligned} \quad (\text{II-64})$$

and δ is the solar declination, φ is the latitude, R is the local time of sunrise in hours, S is the local time of sunset in hours, T is the temperature, and t is the time in hours after local midnight. The coefficients, b_0 , b_1 , b_2 , and b_3 , were estimated using station records of hourly temperature change. The coefficients were categorized by month and by cloud cover. The basic temperature-change data were derived using ten-year average diurnal temperatures from which any net diurnal tendency (attributable to advection) was first subtracted. The data used in our computations of the coefficients were obtained from the U.S. Air Force and are described in a technical note by Kimball, Richardson, and Frey [15].

Once the empirical coefficients have been derived, the tendency implied by Bryan's equation may be computed given the type of cloudiness, the present temperature, the local time, geographical position and the time of year. The cloudiness specification was chosen to take advantage of the fact that low cloudiness would be predicted within the

model. Middle or high cloudiness might reasonably be predicted by a free air model and made available to this model. The three categories of cloudiness were therefore taken to be

- (a) Category 1—clear or scattered clouds
- (b) Category 2—broken or overcast clouds above 5000 ft
- (c) Category 3—broken or overcast clouds below 5000 ft.

Thermal advection at the level of the instrument shelter cannot be neglected. We compute it by assuming a logarithmic wind profile to exist through the 1.22-m air layer above the surface roughness height.

The influence of latent heat exchange is neglected as a smaller order effect in this model.

20. Surface Humidity Specification

The model requires the specification of the temporal variation of specific humidity at the lower boundary of the contact layer. For points which lie over water, we may safely assume that the relative humidity is always close to one hundred percent near the air-water interface. Over land, on the other hand, the low-level relative humidity depends upon the amount of available soil moisture and the complex process by which this moisture is liberated from the soil.

We originally considered approaching the prediction of surface relative humidity in a manner analogous to that used for the surface temperature. The Air Force data collection provides the requisite dew-point temperatures for such an approach. It was pointed out to us that another technique was available which would not require any significant development effort and we therefore decided to adopt it for the present.

In their effort to develop an analog computer for micrometeorological use, Halstead, et al. [13] were faced with the need to compute the percentage of available energy used to evaporate water. They employed a parameter, M , which is denoted as the "percent wetted area" in physiological climatology. For their problem, Halstead, et al., related M to the water vapor densities as follows,

$$\rho'_0 - \rho'_H = M (\rho'_{0SAT} - \rho'_H) \quad (II-65)$$

where ρ' denotes water vapor density; the subscript, 0, denotes a measurement near

the surface; the subscript, H, denotes a measurement some distance removed from the surface; and ρ_{0SAT} , is the saturation vapor density near the surface. Using meteorological data gathered during the Great Plains field program (this program is described by Lettau and Davidson [18]) it was found [13] that M was well correlated to measured soil moisture and that its value tended to remain constant during periods of twenty-four hours or more.

We have adapted this result to our problem as follows: let q be the specific humidity at the top of the contact layer, and q_i be the surface specific humidity measured at the level of the instrument shelter; finally, let q_{is} be the saturation specific humidity measured at the same level as q_i . Using measurements of these quantities made prior to the initial time of the forecast we may compute a value of M from

$$M = (q - q_i) / (q - q_{is}). \quad (II-66)$$

Now, holding M constant through the forecast interval permits one to solve for the surface relative humidity from the equation,

$$RHS(t) = M + (1 - M) q(t) / q_{is}(t). \quad (II-67)$$

Since q_{is} is principally a function of temperature, its value may be computed from the predicted value of the surface temperature. The value of q is predicted within the model and is available at every time step for use in evaluating Eq. (II-67) for RHS(t).

21. Coordinate System and Terrain Variation

The equations used in this prediction model are written in Cartesian coordinates. The horizontal coordinates (x, y) are established on a polar stereographic mapping of the Northern Hemisphere with their origin taken at the North Pole. The particular polar stereographic map used is "true" at 60° North Latitude and has a scale of 1:5,000,000. The map scale factor, σ , is defined as follows,

$$\sigma = [1 + \sin \frac{\pi}{3}] / [1 + \sin \varphi] \quad (II-68)$$

and its numerical value, over the region shown in Fig. 1, is given in Table I.

The vertical coordinate (Z) has its origin at the height of the surface terrain. The elevation of the surface terrain was derived from the values given by Berkofsky and Bertoni [4] and from other sources of topographic data. The elevations assigned to the grid points are given in Table II.

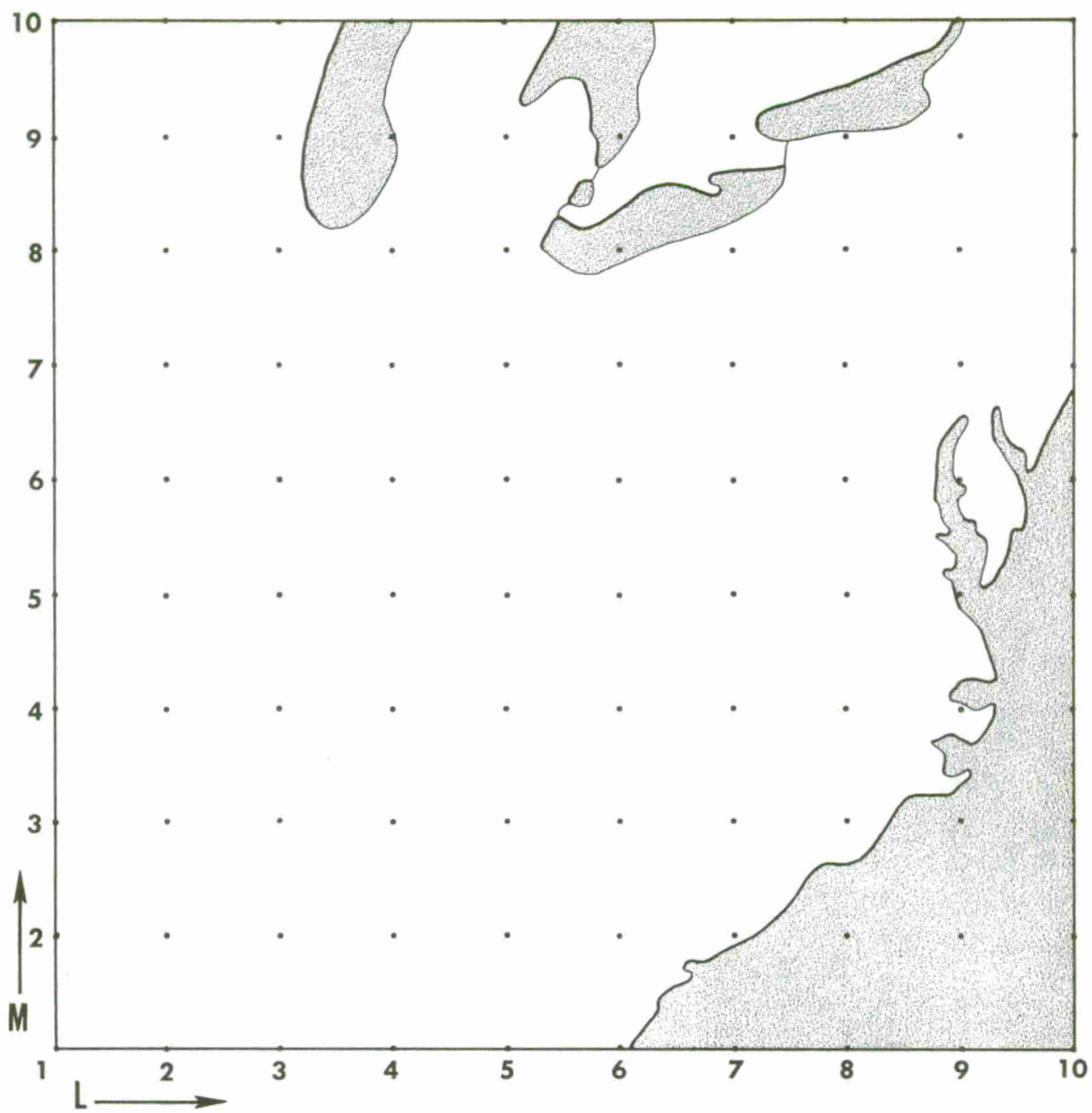


Fig. 1. Grid network used in this study.

TABLE I
MAP SCALE FACTOR AT GRID POINTS IN FIG. 1

<div>M \ L</div>	1	2	3	4	5	6	7	8	9	10
10	1.104	1.100	1.099	1.097	1.095	1.095	1.094	1.095	1.095	1.096
9	1.115	1.114	1.111	1.109	1.108	1.108	1.108	1.108	1.108	1.109
8	1.129	1.126	1.124	1.122	1.121	1.120	1.120	1.120	1.121	1.123
7	1.142	1.140	1.138	1.137	1.135	1.134	1.134	1.135	1.135	1.137
6	1.156	1.154	1.152	1.151	1.149	1.148	1.147	1.148	1.149	1.151
5	1.172	1.168	1.167	1.165	1.164	1.163	1.163	1.163	1.164	1.165
4	1.187	1.184	1.183	1.180	1.179	1.178	1.178	1.178	1.179	1.180
3	1.201	1.199	1.197	1.196	1.194	1.193	1.194	1.194	1.194	1.196
2	1.217	1.215	1.213	1.212	1.210	1.209	1.209	1.209	1.209	1.210
1	1.234	1.232	1.230	1.229	1.228	1.227	1.226	1.227	1.228	1.228

TABLE II
ELEVATION OF TERRAIN (IN METERS) ABOVE MEAN SEA LEVEL AT
VARIOUS GRID POINTS GIVEN IN FIG. 1

<div>M \ L</div>	1	2	3	4	5	6	7	8	9	10
10	367	206	227	191	227	191	191	185	70	82
9	267	327	212	191	245	191	182	167	121	182
8	261	203	197	233	258	191	348	667	369	124
7	221	179	185	245	306	282	370	385	82	15
6	252	109	118	158	273	173	606	148	9	0
5	124	91	148	239	336	439	364	124	0	0
4	70	115	183	211	330	530	221	70	6	0
3	48	70	185	203	324	136	58	15	0	0
2	115	92	52	140	93	39	18	0	0	0
1	61	52	39	61	70	21	0	0	0	0

The surface roughness parameter has been derived from data given by Kung [16]. He made use of information on land usage available from the U.S. Department of Agriculture and related it to estimates of the surface roughness parameter, available for various crops and trees, from detailed local studies. The grid-point values of surface roughness used in the model integrations of winter cases are given in Table III.

TABLE III
SURFACE ROUGHNESS PARAMETER (IN CENTIMETERS) AT THE
GRID POINTS SHOWN IN FIG. 1

M \ L										
	1	2	3	4	5	6	7	8	9	10
10	1	1	1	1	2	1	2	10	12	32
9	1	1	1	1	2	1	1	2	22	32
8	5	2	2	2	2	1	2	19	30	20
7	10	5	4	3	2	5	15	32	21	10
6	15	15	15	15	16	20	30	32	10	1
5	25	28	30	30	30	35	45	30	10	1
4	35	40	42	50	52	61	47	20	10	1
3	45	50	56	60	70	65	25	10	1	1
2	55	62	70	80	93	50	8	1	1	1
1	70	90	100	101	100	20	1	1	1	1

SECTION III

INPUT DATA ANALYSIS

The surface and upper-air observations made during two time periods were collected through local weather teletype facilities with the cooperation of the personnel of the Travelers Weather Service. From these routine data, we constructed the grid-point data required by the prediction model. We employed some machine computation methods in the data preparation but the analysis procedure was not fully automated. The surface charts were analyzed for the temperature field. Grid point values of surface temperature were interpolated from the surface isopleths. Over the ocean, we used monthly mean values of the sea surface temperature made available to us by Mr. A. Thomasell of the Research Center staff.

Radiosonde reports for each observing station were processed to obtain temperature and dew-point temperature values at each level in the vertical required in the model. These values were linearly interpolated from mandatory- and significant-level observations. We then plotted, at the various reporting stations, the difference in temperature between particular levels. These data were then analyzed and, by interpolation between isopleths, grid-point values were obtained. When these vertical temperature differences were used in conjunction with the grid-point values of surface temperature, we reconstructed vertical temperature distributions at each grid point.

From the interpolated radiosonde data, we plotted the dew-point depression at each reporting station. Analyses of these fields were then constructed and interpolation again yielded grid-point values. When these data were combined with the grid-point temperatures, the grid-point values of dew-point temperature resulted. Conversion of these data to specific humidity values was carried out using a standard atmosphere pressure-height relation.

This analysis technique seems suitably controlled, but it is necessary to use good judgement when performing the hand analysis. The development of a good automated procedure is highly desirable.

The geostrophic wind components at $Z = H$ and the upper level cloudiness can, in principle, be obtained from free-air prediction models. However, we were forced to use the observed synoptic reports to construct the needed input.

Geostrophic winds were computed from the observed field of geopotential at 850 and 700 mb at twelve hour intervals. These were interpolated vertically to obtain geostrophic winds at $Z = H$. Six-hour pibal wind observations were used to determine if the temporal variation of the geostrophic winds between the twelve-hour observations was reasonably accurate. Changes were introduced at the sixth hour if it appeared necessary.

Nephanalysis of the middle- and high-cloud fields was attempted using the six-hourly surface synoptic data. The mean condition of cloudiness was fixed over a six-hour interval at each grid point by assigning to the parameters ICLU1 and ICLU2 the value 1 for clear or scattered high and middle cloudiness or 2 for broken to overcast high or middle cloudiness.

It should be noted that we did not attempt to modify the radiosonde temperature or humidity observations to reflect the observed cloudiness. Such a procedure might prove desirable in operational use of the model. In this connection the initial specific moisture (r) field was always equal to the initial specific humidity (q) field.

SECTION IV

ANALYSIS OF TESTS

The results of three forecasts (identified as Cases A, B, and C) made with the prediction model are given below. Each test case is a 12-hr forecast.

Case A: 12Z February 6, 1964 to 00Z February 7, 1964

This case was run previously with an earlier model [12] and served as a control in the development of the revised model. The synoptic charts at the initial time [see Fig. 2(a) to 2(n)] depicted a diffuse occluded low at the surface with its center in southern Ohio. At upper levels, this low was more intense but the cold air was located to its south. On the surface chart at the initial time "four-dot rain" was reported at Cape Hatteras, N. C. and Norfolk, Va., indicative of the development of a secondary cyclone. This secondary circulation was very evident in the 50-m wind field diagnosed using the model (see Fig. 3). During the forecast period, the secondary circulation intensified and moved rapidly northward. At upper levels this development was associated (during the first six hours) with a gradual turn of the upper winds from southerly to westerly over the south-central portion of the region. During the second half of the forecast period the upper circulation rapidly adjusted to the developing secondary cyclone. The upper low accelerated, and at the end of the forecast period was located over eastern Pennsylvania.

The results obtained in this case [see Fig. 2(a) through 2(n)] can be seen to be of highest quality in regions removed from the lateral boundaries. This is to be expected in view of our neglect of horizontal advection on inflow boundaries. The most serious errors introduced in this case occur in the northeastern region. At the initial time, the air in this region was very dry. As the situation evolved, the humidity increased due to the over-water trajectory of the air in advance of the secondary cyclone. The model does not detect this transport because of the boundary condition. The movement of the cold air trough through the center of the region is well predicted, as is the cloudiness and precipitation observed through the Appalachians. The close correspondence of the observed and predicted 50-m wind fields bears witness to the adequacy of the predicted thermal field configuration. Since the thermal wind within the boundary layer is predicted, such close agreement of the 50-m wind fields could not occur if the predicted thermal field was poorly correlated with the observed field.

The pattern of humidity (cloudiness) depicted in the vertical cross-sections is traceable to the "terrain induced" component of the vertical wind. In Fig. 4, we show this field as predicted at the verification time. It is significant that the scale of the major feature of this field is smaller than the NMC mesh spacing. The computation of the terrain influence on the weather associated with the vertical velocity field requires the consideration of such smaller-scale phenomena. Indeed, the secondary cyclone at the initial time (see Fig. 3) also would have been lost in the NMC grid.

Figures (5) and (6) show, respectively, the net sensible heat and latent heat added to the transition layer during the forecast periods. The values plotted were computed by integrating the "instantaneous values" of the fluxes at hourly intervals. It is interesting to note that the maximum value of sensible heat transfer occurs over the land. Clear skies prevailed over this region and the pattern of heating reflects the cloudiness distribution to a significant extent. Over the ocean, the latent heat transfer is much greater than the sensible heat transfer. The accuracy of this result is in doubt due to the inadequacy of the initial data in that region.

Case B: 00Z January 23—12Z January 23, 1965

Figure 7(a) and (b) displays the synoptic patterns at the initial and final times of the forecast period. Low cloudiness and precipitation are noted across the northern and western portions of the region at the initial time. The activity in the north is associated with a stationary front. In the southwestern region, showery conditions are reported in the warm air—the NMC analysis indicated the presence of a squall line in this area.

During the forecast interval, the cold air pushed southward along the eastern boundary, with a small depression indicated on the front near Washington, D.C. Precipitation continued to occur over the northern portion. Low cloudiness developed over the central portion of the map and an elongated area of precipitation was reported along the western slope of the Appalachian Mountains.

Figure 7(c), (d), and (e) shows the analysis of the thermal and humidity fields observed at 12Z January 23, 1965. The corresponding forecast charts are given in Fig. 7(f), (g), and (h). The isotherm ribbon associated with the stationary front was observed to move southward along the east coast during the forecast interval. This movement was not predicted by the model and the intensity of the thermal gradient in that region is under-predicted.

The cold trough through the central region is a reflection of the terrain elevation. Rather little temperature change occurred therein. The incursion of higher humidity into the southwestern portion is predicted by the model, principally at the upper-most level and at the level of the instrument shelter. The observed and predicted surface charts (instrument shelter temperature and 50-m wind) shown in Fig. 7(i) and (j) are in good agreement except in the northeastern portion. The band of precipitation on the western slope of the Appalachian Mountains seems to be due to a high-level condensation process. The low cloud reported is apparently due to the advective formation of stratus and, possibly, in part due to the evaporation of precipitation falling into the boundary layer from above.

West to east, vertical cross sections through the predicted atmosphere are given in Fig. 7(k) through (n). In Fig. 8 we have constructed a south to north vertical cross section along the coordinate line, $L = 5$.

Figures 9 through 13 are soundings showing the initial and predicted grid-point temperature structure and the thermal structure at the verification time observed at a nearby radiosonde station. In Fig. 9 we show a point near the eastern boundary of the grid. The front was observed to pass south of this point during the forecast period. The predicted sounding is too warm at low levels, reflecting the failure of the model to properly displace the frontal position. Above 300 m the predicted sounding agrees closely with the observed data. We may note also the very strong inversion in the lowest 50 m of the predicted sounding. This low level structure may be unrealistic due to the absence of sufficient refinement in the contact layer theory for strong inversion conditions.

Figure 10 shows a grid point near the elongated axis of precipitation on the western slope of the Appalachians. The negligible change observed in the vertical temperature structure is properly treated by the model. Figure 11 shows a point located just to the north of the stationary front throughout the forecast period. At low levels (below 600 m) some cooling was observed to occur, whereas the model predicted some warming. Note again the strong inversion in the predicted sounding between the surface and 50 m. Figure 12 is for a point located similarly to that shown in Fig. 11, with rather similar results. In Fig. 13 we indicate the results at a point located to the north of the front but nearer to the developing storm (just off the western edge of the map). The warming above

the frontal inversion is predicted by the model, but the observed low-level cooling is not indicated in the forecast. We may note the northward displacement of the thermal ribbon in the horizontal depiction charts as the explanation for the low-level error at this grid-point.

Figure 14 shows the temperature and dew-point soundings observed at radiosonde station 226 at the initial and final times of the forecast, as well as the predicted values at the nearby grid point. This station was reporting moderate rain at the verification time. The analysis is complicated by the nearness of the grid point to an inflow boundary, but with the exception of the observed inversion between 850 m and 1150 m and the departure below 300 m, the predicted temperature lapse rate is very close to that observed. The predicted dew-point spread is greater than the initial and observed values above 400 m. The vertical velocity predicted at this grid point was small until the tenth hour. At that time an upward flow of 2 cm sec^{-1} was predicted in the upper portion of the boundary layer. Consequently, we must ascribe the predicted drying to advection. Below 400 m, the observed increase of humidity is well predicted. In the forecast super-saturation was predicted between 50 m and 150 m. The liquid water concentration predicted was between 0.2 and 0.4 gms kg^{-1} . There is a good possibility that the observed increase in humidity at upper levels was in response to the evaporation of the precipitation which fell through the boundary layer from above. One must also note that the convective activity which occurred in this general region is not predicted by the physical model. Its potential influence on the observed soundings cannot be ignored as a source of spatial scale confusion.

Case C: 12Z January 24, 1965—00Z January 25, 1965

In Fig. 15(a) and (b), the synoptic patterns at the beginning and end of the Case C forecast are indicated. A low-pressure center was located over Michigan at the initial time. Along the east coast a ridge of cold air was entrenched to the east of the Appalachian Mountains and north of the stationary front located along the border between Virginia and North Carolina. A cold front extended from the low southward to the southwestern edge of the grid region.

During the twelve hours of the forecast, the low moved east—northeastward to the north of Lake Erie. The front moved eastward with the low. It extended southward through

western Pennsylvania and Virginia as a warm type occlusion. From Virginia southward, it was a cold front along which squalls were reported. A secondary low had developed on the stationary front over the coastal waters and at 00Z was located at 40°N and 71°W.

The entire grid region was covered by broken or overcast low cloudiness at the initial time. Precipitation was widespread. An extensive area of snow was reported to the west of the low. An area of rain showers was reported along the cold front as far south as Nashville, Tenn. Under the cold-air ridge along the east coast, freezing precipitation was reported over a large area. Showery conditions also existed in the warm air along the coast and over the coastal waters.

At the end of the forecast period, cloudiness diminished over the southwestern portion of the region but continued in evidence along the northern half and along the east coastal region. The precipitation pattern changed in response to the displacement of the low and the cold front. A small region through central New York and Pennsylvania separated the frontal precipitation from that in the cold ridge associated with the off-shore low.

Figure 15(c), (d), and (e) depicts the analysis of temperature and humidity observed at 00Z, Jan. 25, 1965. The analyses of the predicted fields are given in Fig. 15(f), (g), and (h). At the three levels, the forecast of temperature in the northeast is much too high. The explanation for this error lies in the development of the secondary coastal low. In Fig. 16, the sounding at radiosonde station 518, near grid point $L = 10$, $M = 7$, is shown. It indicates that below 1500 m the forecast sounding is displaced toward higher temperatures. The observed trend is the reverse. If one compares the 50-m wind fields shown in Fig. 15(i) and (j), the influence of the off-shore development is evident. The low-level wind field is distorted away from verification because the thermal wind field is inaccurately predicted.

The principal line of cold air is well positioned in the forecast charts. We must note that the verification analysis over the ocean is highly speculative. As a consequence, the thermal gradients in the southeast portion are not reliable. The errors in the forecast temperature fields are given in Table IV for each grid point, excluding those over the ocean. Also given are the errors resulting from a persistence forecast. The later values are the negative of the observed temperature changes.

TABLE IV
COMPARISON OF TEMPERATURE PREDICTION ERRORS (°K)*
THE MODEL VERSUS PERSISTENCE†

(a) At 500 m level

		Grid coordinate L									
		1	2	3	4	5	6	7	8	9	10
Grid coordinate M	10	-3 -4	-1 0	0 1	3 5	7 9	9 8	7 0	4 -9	10 -7	8 -9
	9	-2 -4	-2 0	0 6	-1 7	1 11	0 14	-1 6	-1 1	7 -3	10 -6
	8	1 -2	0 0	1 3	1 4	1 7	0 14	-1 8	6 5	11 4	11 -3
	7	2 -1	2 0	2 3	3 7	2 7	2 13	-1 7	10 5	10 -1	6 -2
	6	4 1	5 4	4 6	4 8	4 9	5 14	2 8	9 2	5 -4	—
	5	6 3	3 3	3 6	3 7	3 8	0 6	6 6	6 3	1 2	—
	4	4 1	2 1	2 4	3 9	3 8	1 5	2 5	-2 3	-3 1	—
	3	2 0	2 2	6 9	6 10	7 11	3 5	-1 2	1 5	—	—
	2	1 -1	2 2	4 6	6 9	6 8	1 3	0 3	—	—	—
	1	2 -1	1 0	3 4	5 5	5 5	4 4	—	—	—	—

(b) At 1150 m level

		1	2	3	4	5	6	7	8	9	10
Grid coordinate M	10	-3 -3	-1 -1	-1 -2	4 3	8 10	9 11	5 4	0 -6	8 -5	7 -8
	9	-5 -5	-2 0	0 4	2 6	5 12	3 15	-3 8	-3 4	5 0	9 -3
	8	-4 -4	-1 2	1 3	1 4	2 7	0 14	-2 9	5 10	9 8	7 -6
	7	-3 -3	1 3	3 5	2 8	-1 7	0 13	-2 7	8 9	8 5	-1 -8
	6	-3 -3	-3 5	2 8	1 9	1 9	2 13	1 10	5 8	0 1	—
	5	2 3	1 4	0 6	1 8	1 8	-1 7	5 9	4 4	-3 1	—
	4	-2 -2	-1 0	-2 3	2 10	3 10	1 7	1 8	-3 4	-5 1	—
	3	3 -3	-1 -2	1 6	4 10	6 13	2 7	-2 4	0 6	—	—
	2	-4 -6	-2 -1	-2 2	2 7	5 10	0 6	-2 5	—	—	—
	1	-3 -6	-3 -4	-1 1	1 3	2 5	1 6	—	—	—	—

*Forecast temperature minus observed temperature.

†Model-forecast errors are entered in the left of each box, persistence errors are entered in the right.

(c) At 2000 m level

		Grid coordinate L									
		1	2	3	4	5	6	7	8	9	10
Grid coordinate M	10	-2 -2	0 0	4 4	6 5	6 9	4 6	0 -2	-4 -10	1 -6	1 -8
	9	-4 -4	-2 0	1 7	1 4	4 6	2 9	-1 4	-2 3	1 0	2 -3
	8	-4 -4	-1 1	0 3	0 3	0 3	2 11	-1 8	5 10	7 12	4 0
	7	-3 -3	1 2	2 4	0 6	-1 5	2 12	0 7	8 11	4 7	-3 -1
	6	-5 -5	3 4	4 7	3 9	2 9	4 13	2 10	5 9	-2 2	—
	5	-2 -2	-1 1	1 5	1 7	1 7	-1 7	4 9	4 5	-1 4	—
	4	-7 -7	-4 -3	-2 2	0 8	-2 7	-4 5	-2 8	-5 4	-5 1	—
	3	-7 -7	-4 -5	-1 3	1 6	-2 6	-4 2	-3 3	0 5	—	—
	2	-5 -5	-3 -3	-1 -1	0 1	-2 2	-4 2	-1 4	—	—	—
	1	-4 -4	-5 -4	-4 -4	-2 -1	-2 0	4 4	—	—	—	—

The average absolute error in temperature at each level is given in Table V below. We have computed a value F_W over the entire grid excluding only points over the ocean, and a value F_I over the interior points ($L = 3, \dots, 8$; $M = 3, \dots, 8$) excluding points within two intervals of a boundary. Similar values (P_W, P_I) were computed for the persistence forecast.

TABLE V
AVERAGE ABSOLUTE ERROR IN TEMPERATURE

Z (m)	F_W (°K)	F_I (°K)	P_W (°K)	P_I (°K)
500	3.56	3.22	4.98	6.72
1500	2.81	2.17	5.90	7.86
2000	2.64	2.19	4.97	6.64

The verification of the humidity prediction is best done by using the observed low cloud and precipitation. The analyzed radiosonde humidity data rarely indicates in a direct fashion the observed cloudiness pattern. It should again be noted that the initial humidity data employed in the forecast were not systematically modified to reflect the initial observed cloudiness.

In Fig. 17, the regions reporting broken or overcast low cloudiness are indicated. We also show the regions reporting precipitation together with an indication of the type of precipitation. Figure 18 was constructed using the humidity predictions at the three levels, 500 m, 1150 m, and 2000 m. If we assume that regions with supersaturation at one of the three levels are experiencing precipitation, then we may note the high correlation in the region of frontal precipitation. Reference to Fig. 15(k) through (n), vertical cross sections through the predicted atmosphere, will indicate that Fig. 18 does not depict the full detail available in the forecast. By comparison with Fig. 19, which is a presentation of the analysis of the observed radiosonde humidity field, the composite prediction chart seems to be superior as a depiction of observed weather conditions.

To provide further detail on the skill of the prediction model we have reproduced the predicted temperature soundings at five interior grid points located near radiosonde stations. The charts (see Figs. 20 through 24) indicate the initial and predicted temperature at the grid point plus the observed temperature at the nearby radiosonde station.

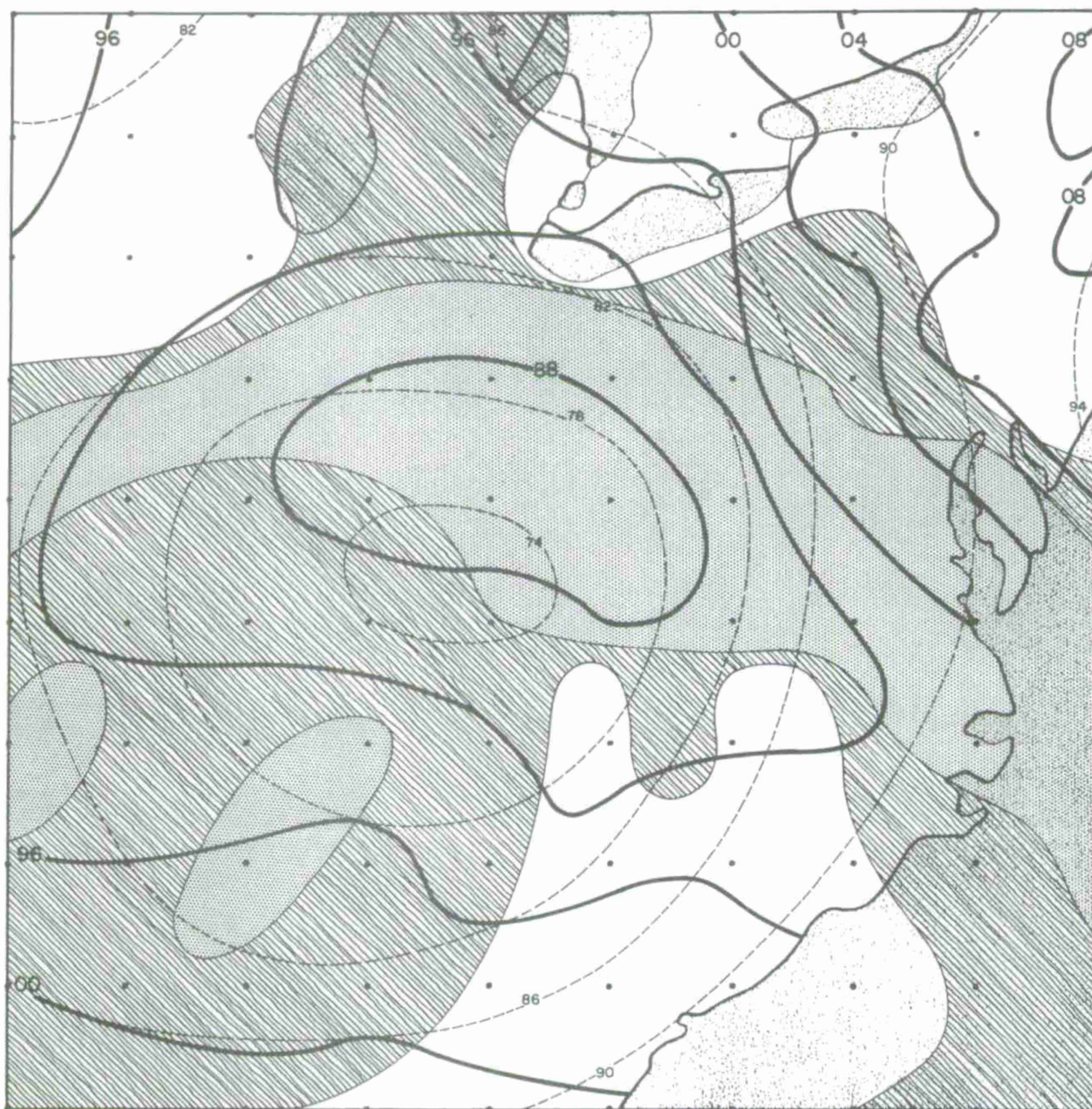






Fig. 2(a). Case A, observed data: surface isobars (mb) and 700-mb contours (tens of meters) at initial time. Shading indicates regions covered by broken or overcast low cloudiness , or experiencing precipitation .



Fig. 2(b). Case A, observed data: surface isobars (mb) and 700-mb contours (tens of meters) at verification time. Shading indicates regions covered by broken or overcast low cloudiness , or experiencing precipitation .

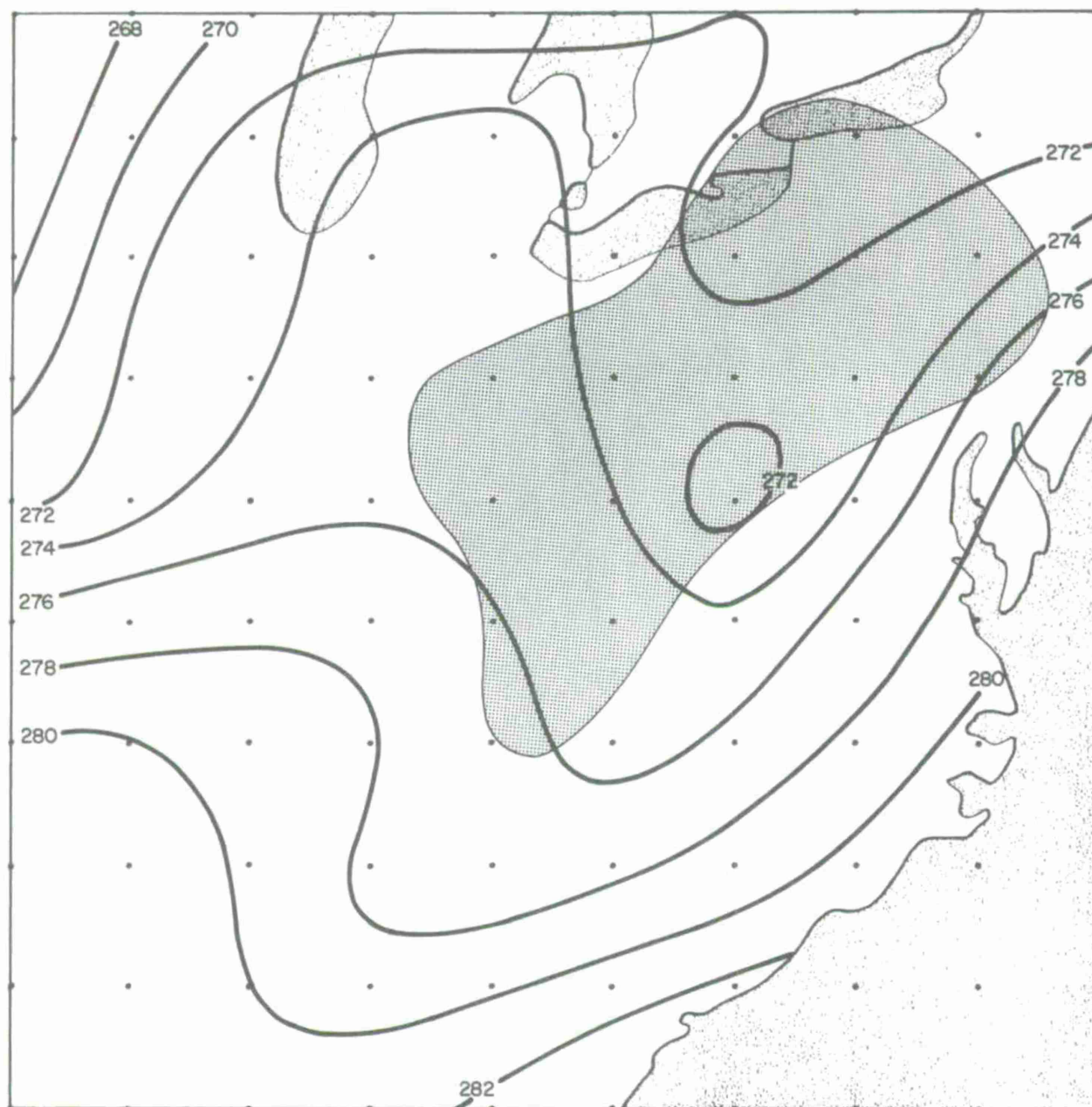



Fig. 2(c). Case A: analysis of observed temperature ($^{\circ}\text{K}$) and humidity at verification time for level 500 m above terrain height. $80\% \leq \text{RH} < 100\%$ 

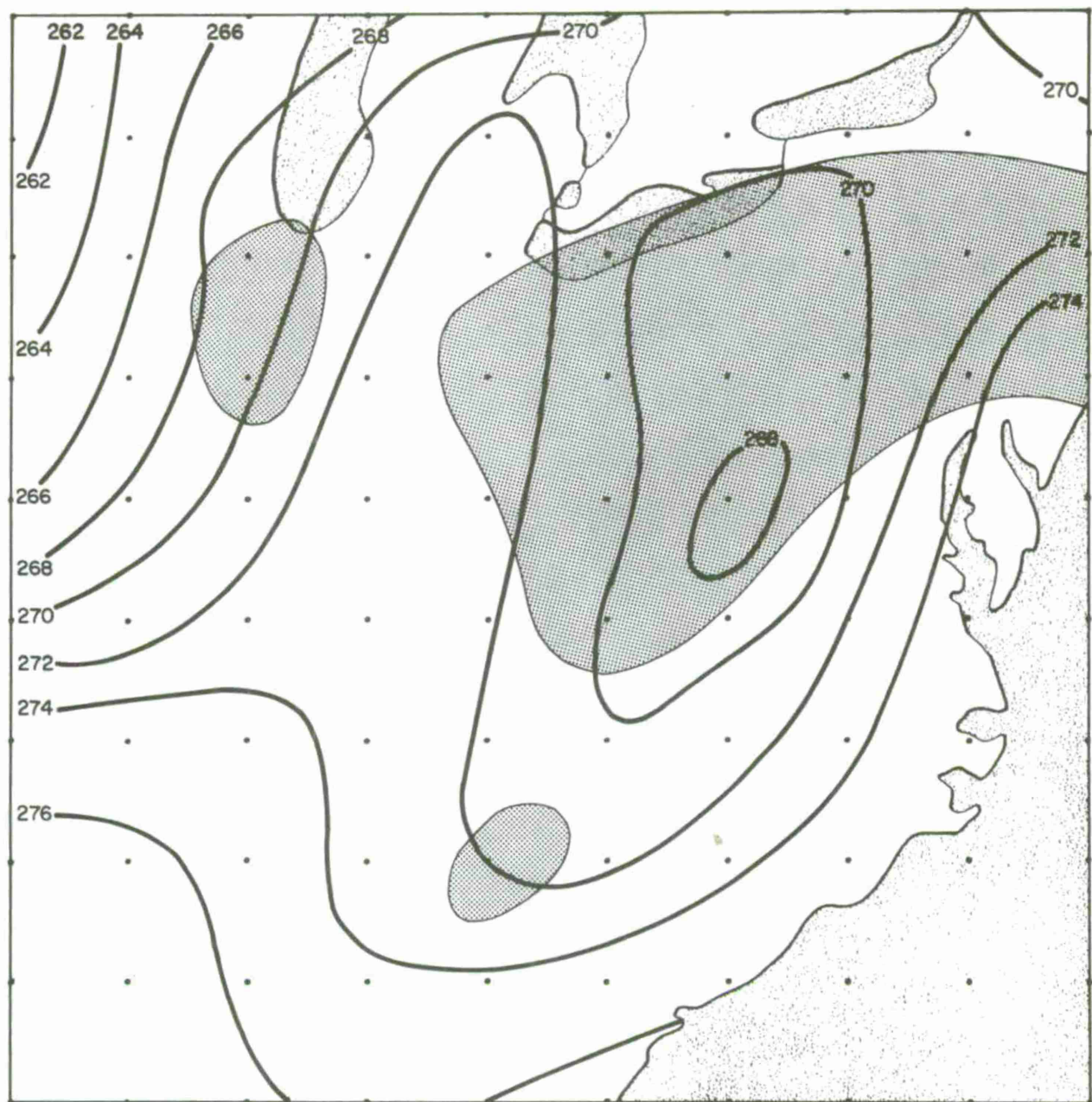



Fig. 2(d). Case A: analysis of observed temperature ($^{\circ}\text{K}$) and humidity at verification time for level 1150 m above terrain height. $80\% \leq \text{RH} < 100\%$ 

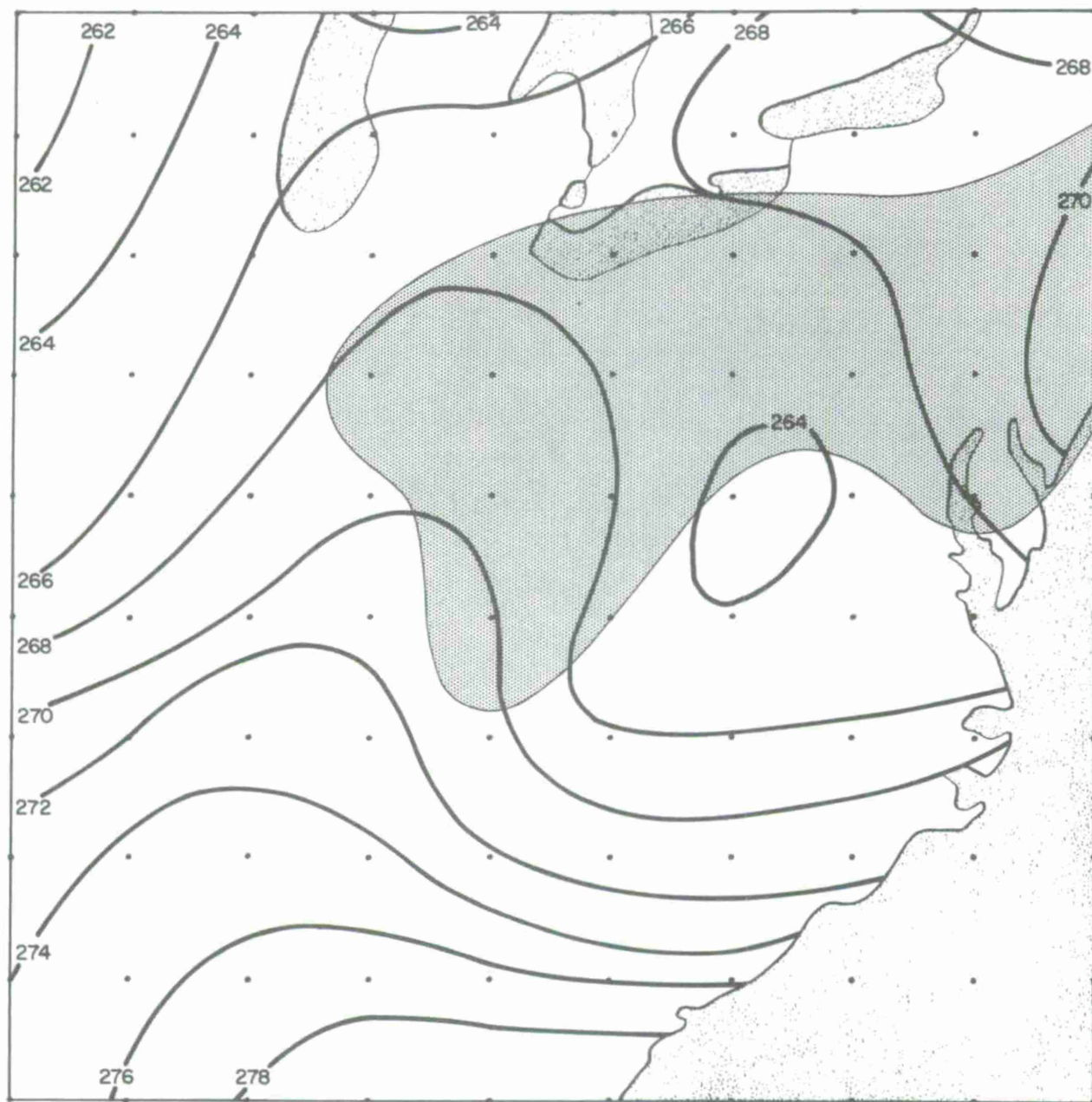




Fig. 2(e). Case A: analysis of observed temperature ($^{\circ}\text{K}$) and humidity at verification time for level 2000 m above terrain height. $80\% \leq \text{RH} < 100\%$ 



Fig. 2(f). Case A: analysis of predicted temperature ($^{\circ}\text{K}$) and humidity at verification time for level 500 m above terrain height. $80\% \leq \text{RH} < 100\%$  $\text{RH} \geq 100\%$ 

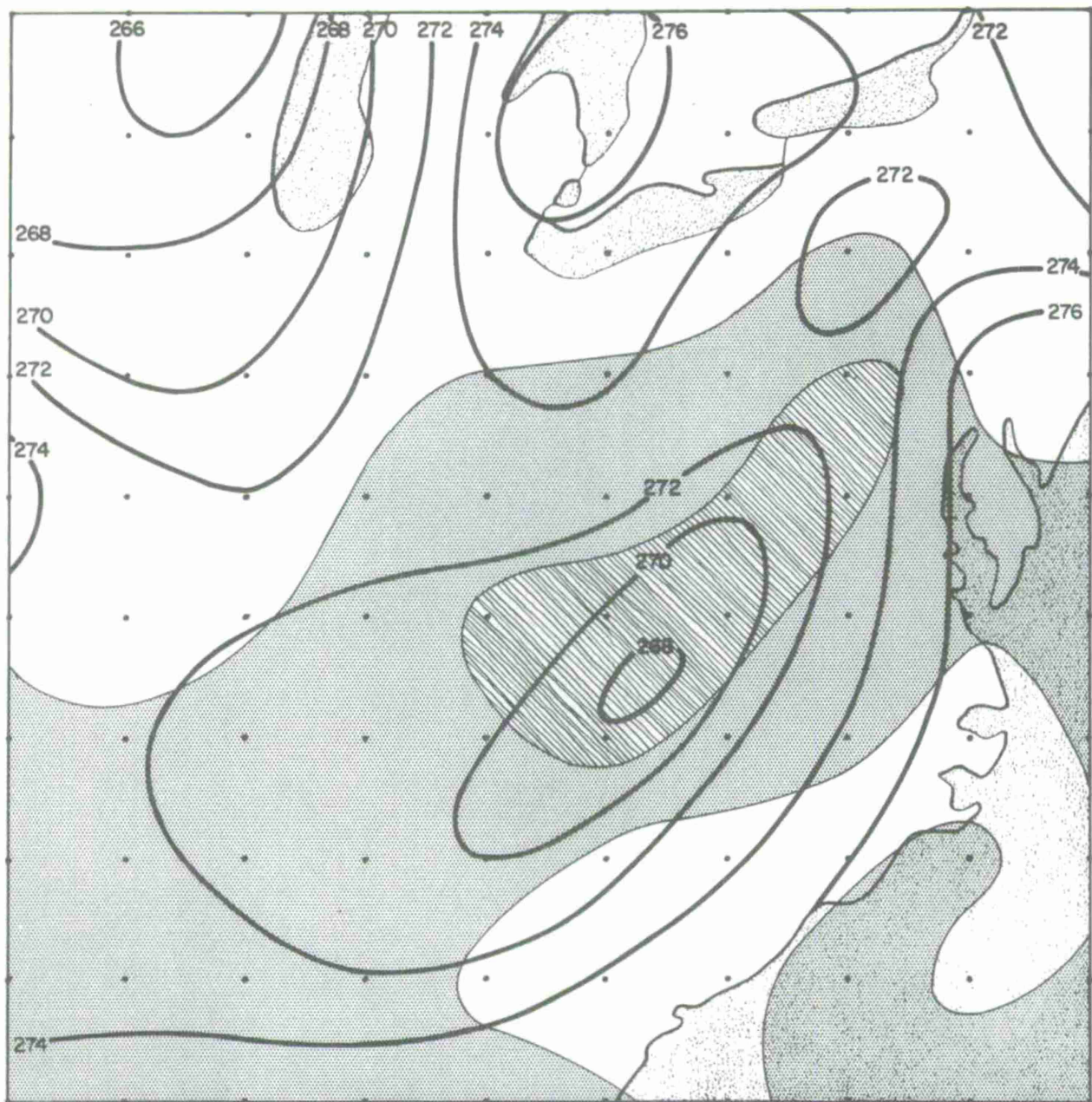




Fig. 2(g). Case A: analysis of predicted temperature ($^{\circ}\text{K}$) and humidity at verification time for level 1150 m above terrain height. $80\% \leq \text{RH} < 100\%$  $\text{RH} \geq 100\%$ 

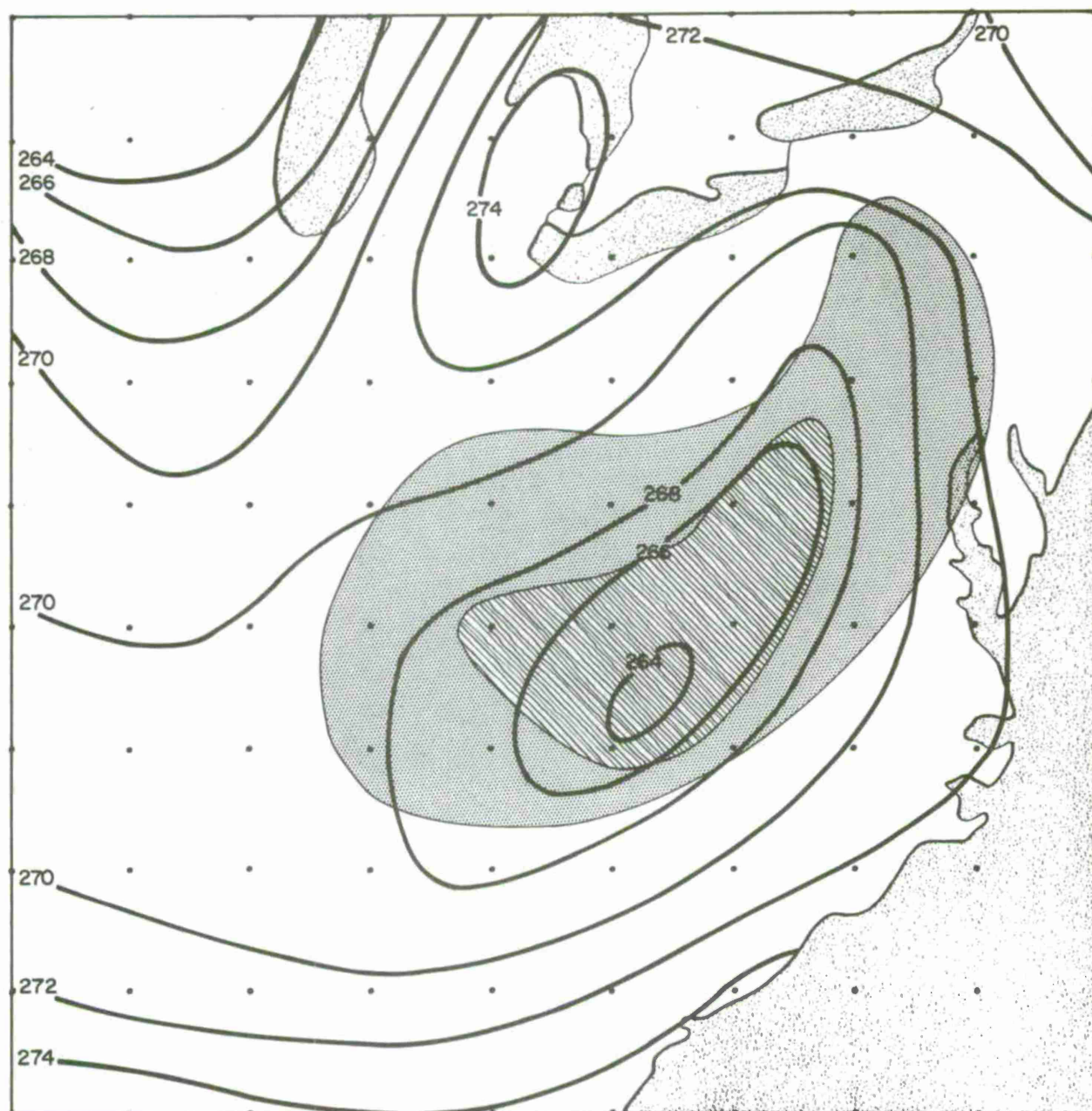




Fig. 2(h). Case A: analysis of predicted temperature ($^{\circ}\text{K}$) and humidity at verification time for level 2000 m above terrain height. $80\% \leq \text{RH} < 100\%$  $\text{RH} \geq 100\%$ 

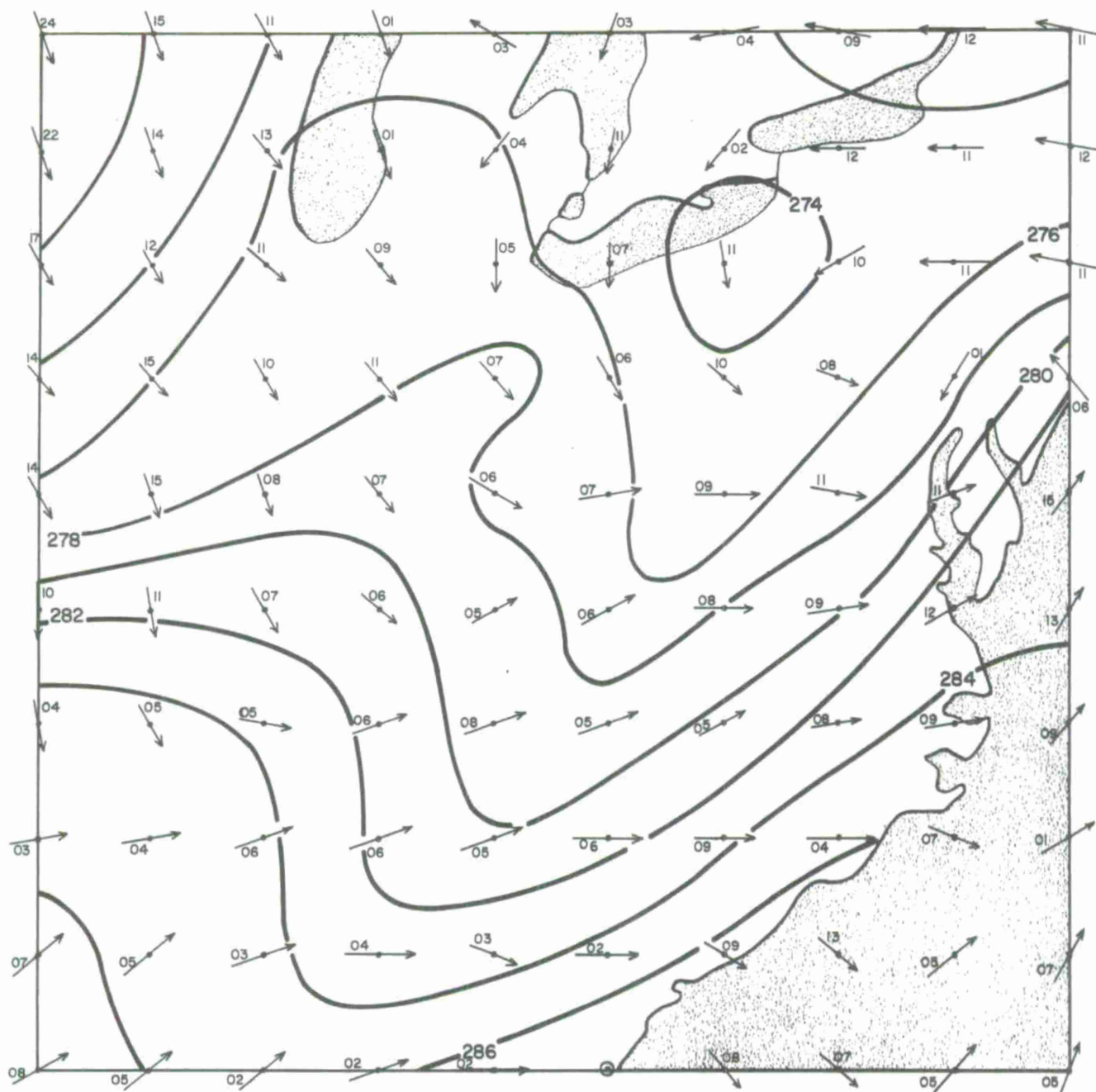


Fig. 2(i). Case A: analysis of observed surface isotherms ($^{\circ}\text{K}$) and derived 50-m wind field at verification time (arrows indicate wind direction; numbers indicate wind speed in m sec^{-1}).

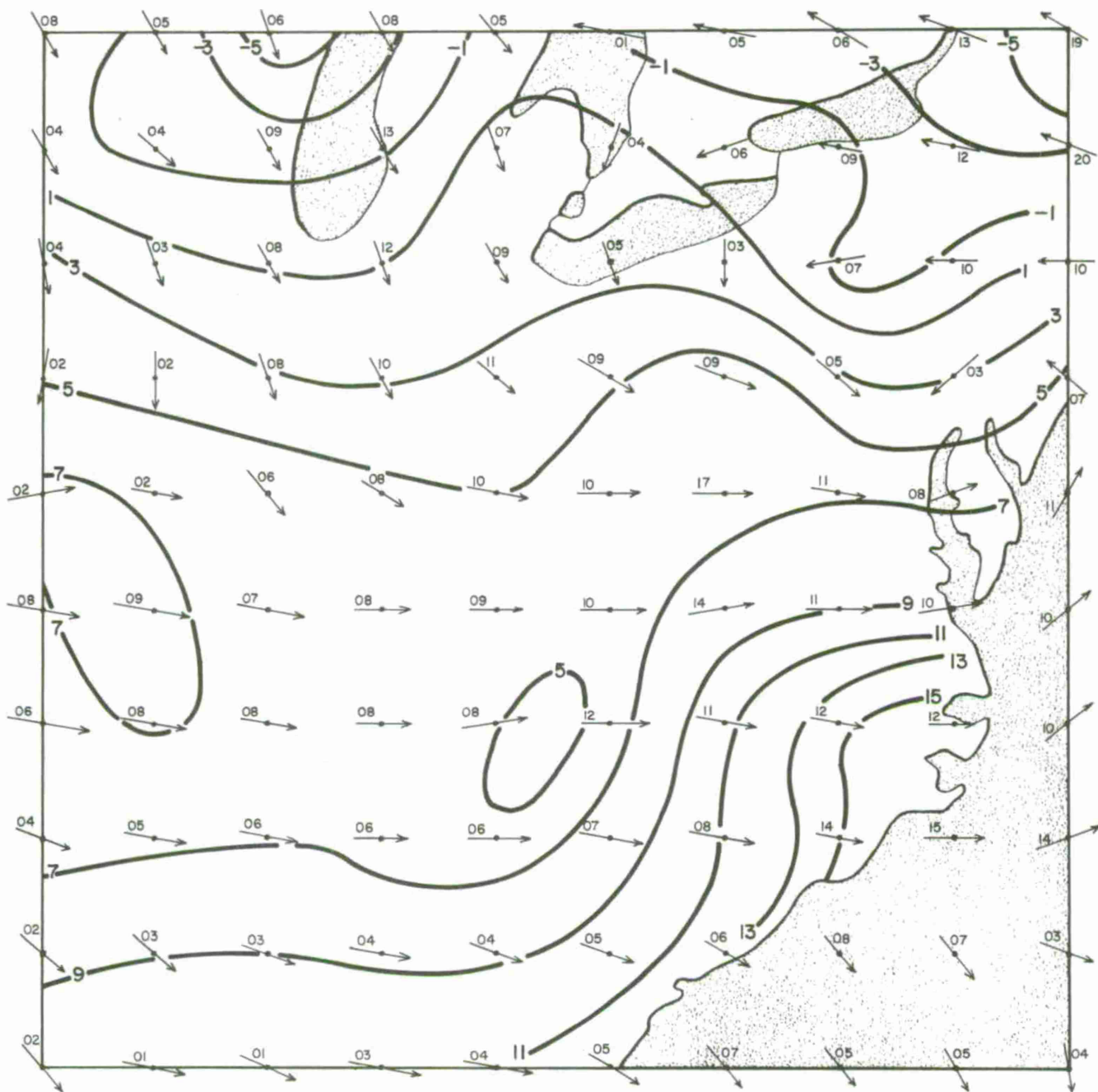


Fig. 2(j). Case A: prognosis of surface isotherms ($^{\circ}\text{K}$) and 50-m wind field valid at verification time (arrows indicate wind direction; numbers indicate wind speed in m sec^{-1}).

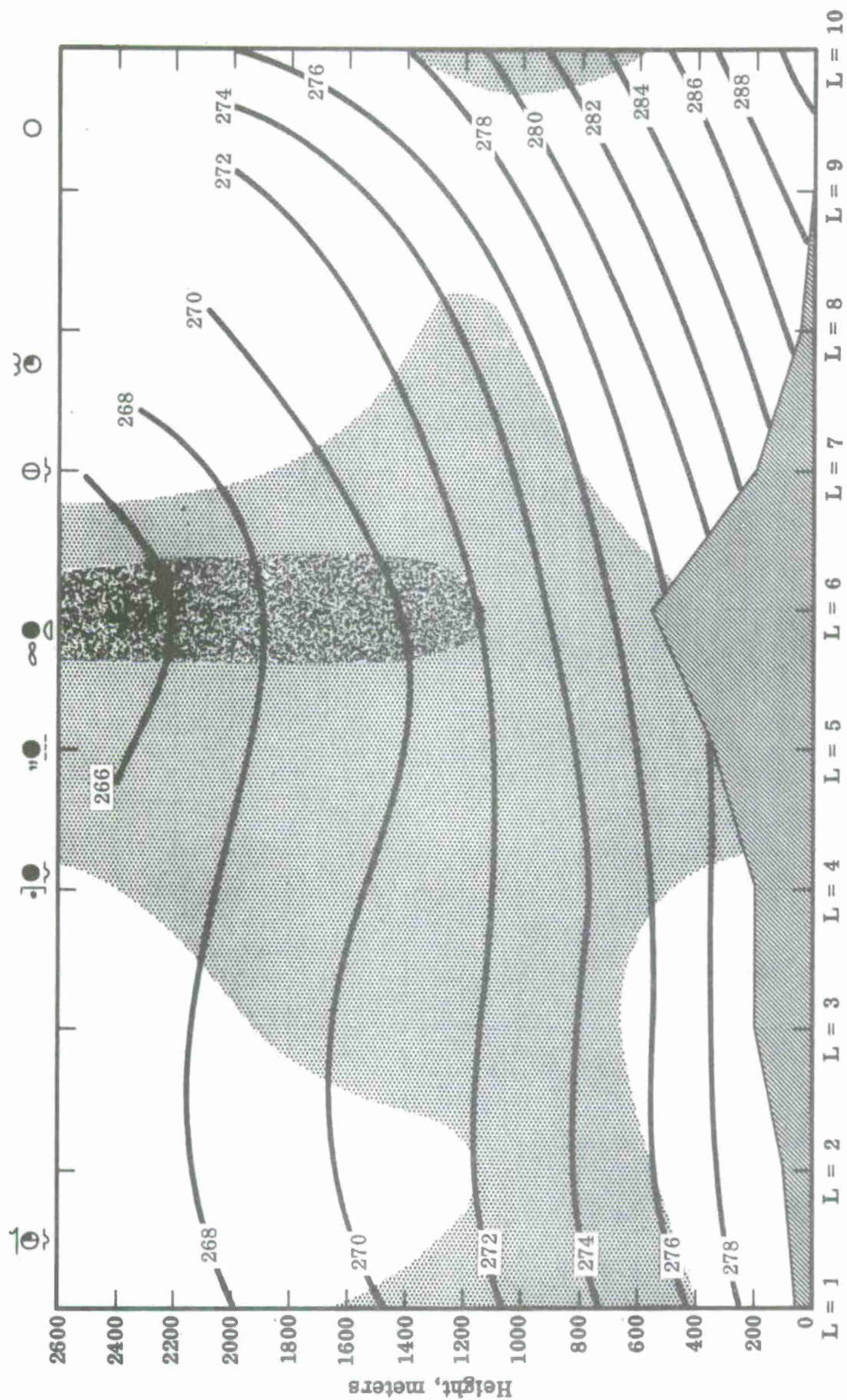


Fig. 2(k). Case A: vertical cross section along grid row $M = 4$ showing predicted temperature ($^{\circ}\text{K}$) and humidity, and observed sky condition and weather (at top of figure), valid at verification time. $RH < 100\%$  $RH \geq 100\%$ 

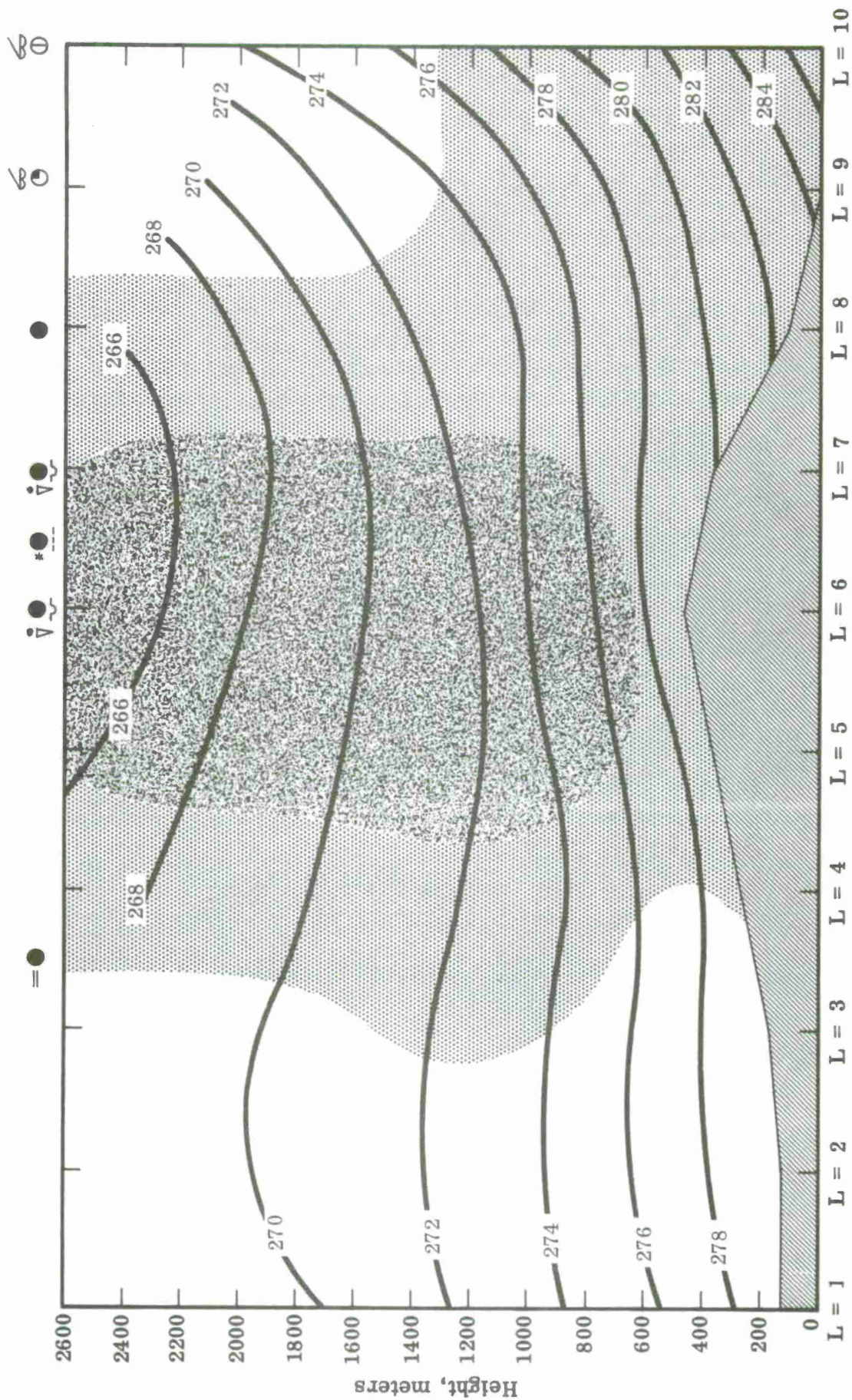


Fig. 2(l). Case A: vertical cross section along grid row M = 5 showing predicted temperature (°K) and humidity, and observed sky condition and weather (at top of figure), valid at verification time. 80% RH < 100% RH ≥ 100%

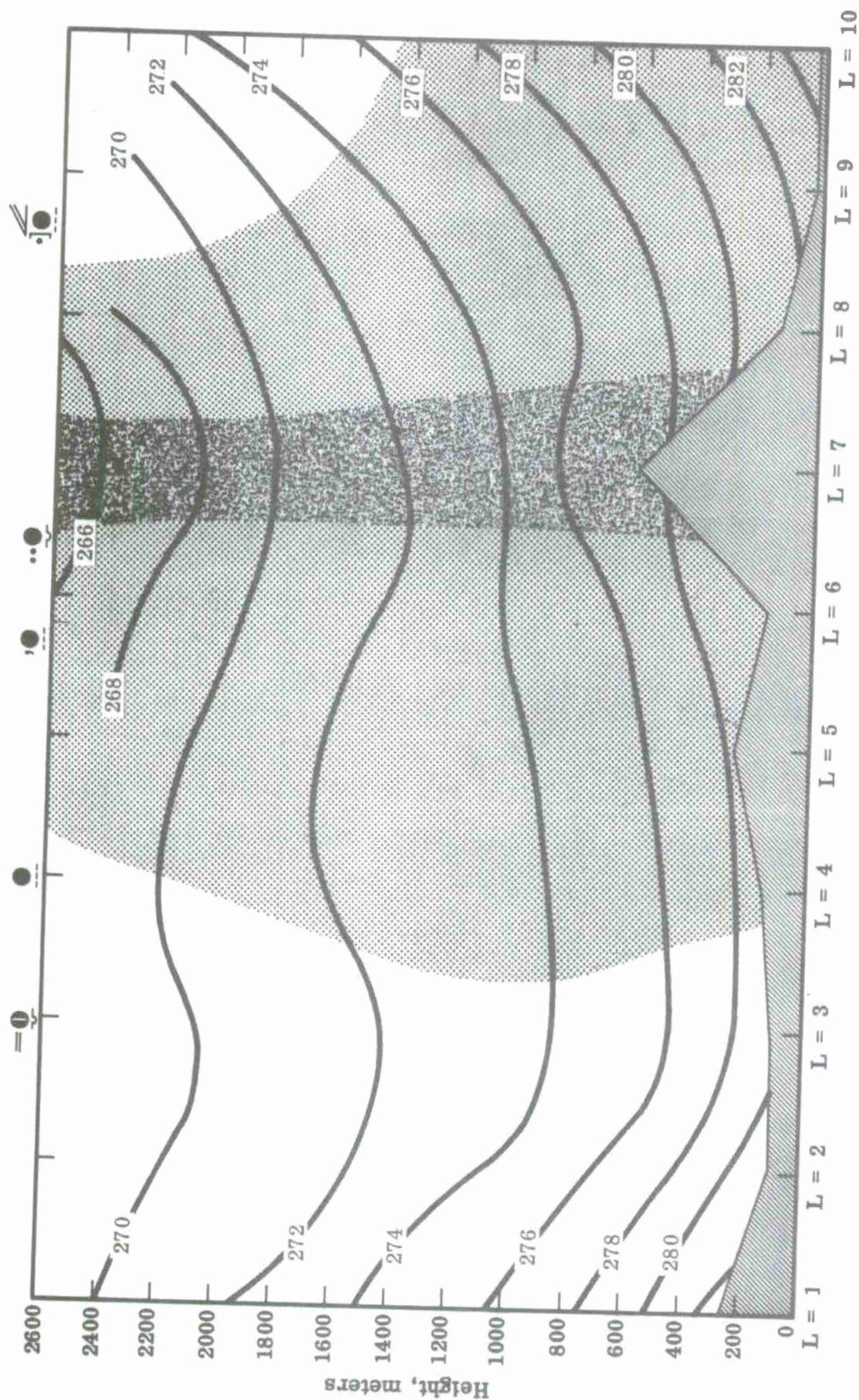




Fig. 2(m). Case A: vertical cross section along grid row M = 6 showing predicted temperature ($^{\circ}\text{K}$) and humidity, and observed sky condition and weather (at top of figure), valid at verification time. $80\% \leq \text{RH} < 100\%$  $\text{RH} \geq 100\%$ 

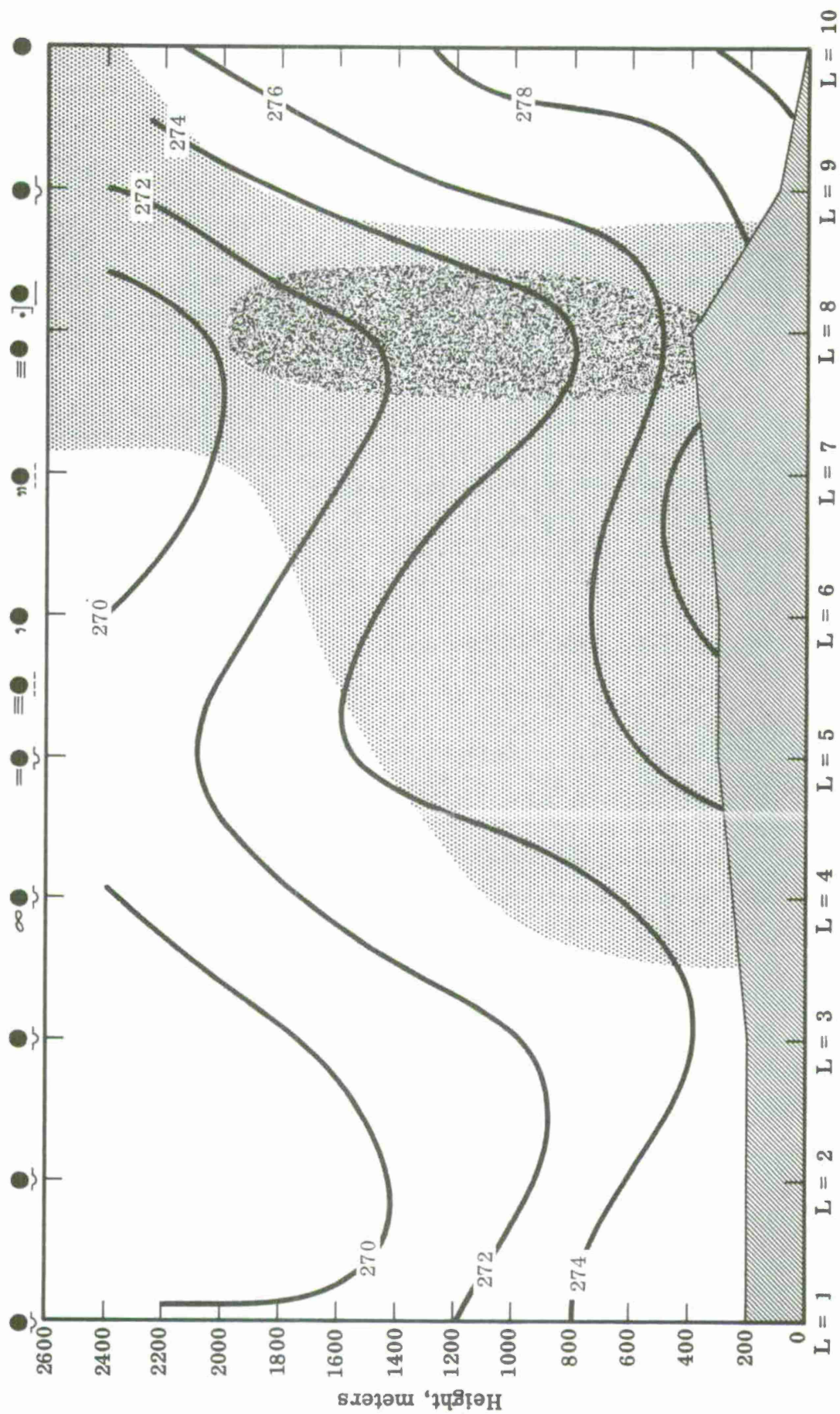


Fig. 2(n). Case A: vertical cross section along grid row M = 7 showing predicted temperature (°K) and humidity, and observed sky condition and weather (at top of figure), valid at verification time. $80\% \leq RH < 100\%$ $RH \approx 100\%$

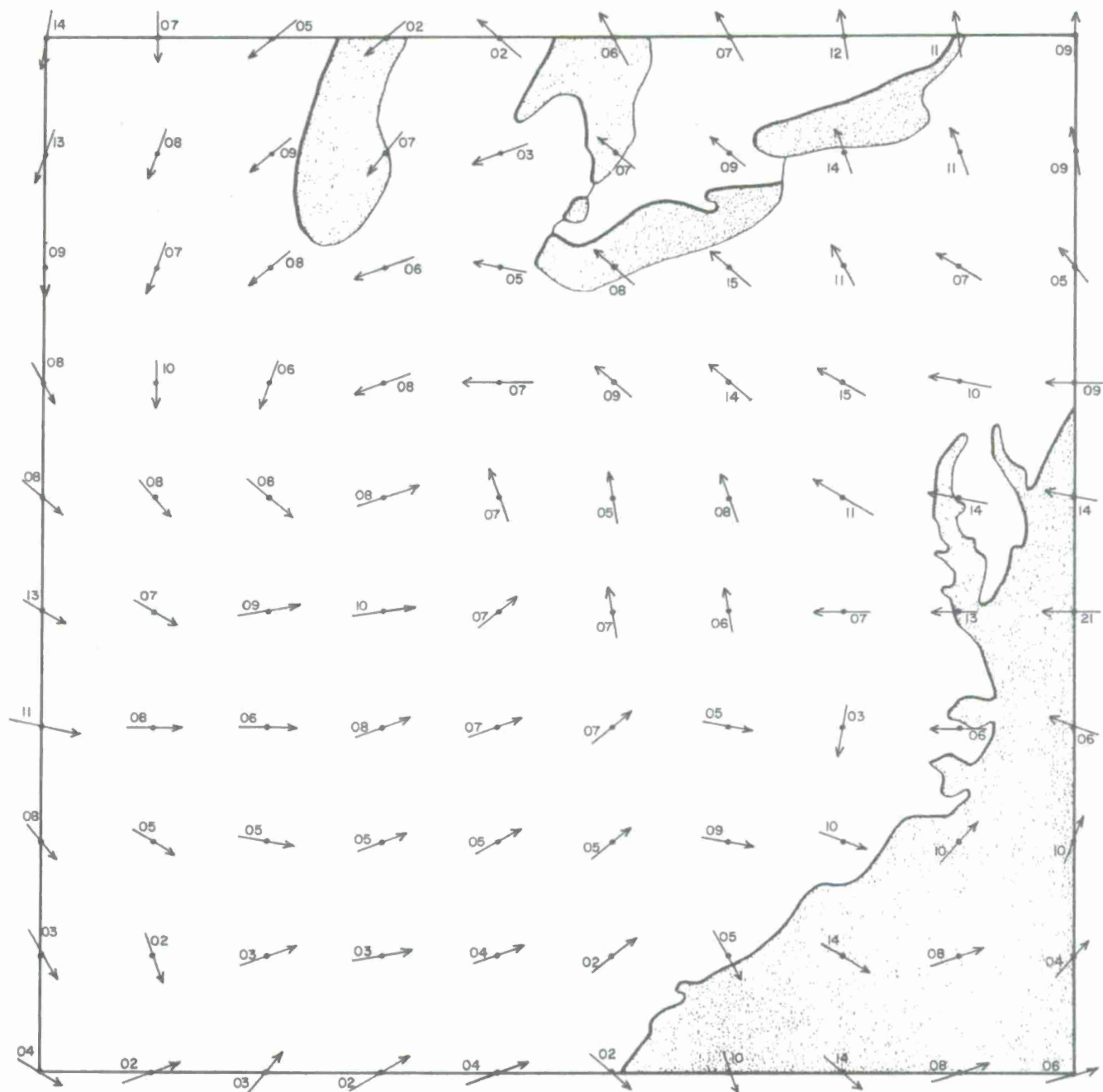


Fig. 3. Case A: analysis of observed surface isotherms ($^{\circ}\text{K}$) and derived 50-m wind field at initial time (arrows indicate wind direction; numbers indicate wind speed in m sec^{-1}).

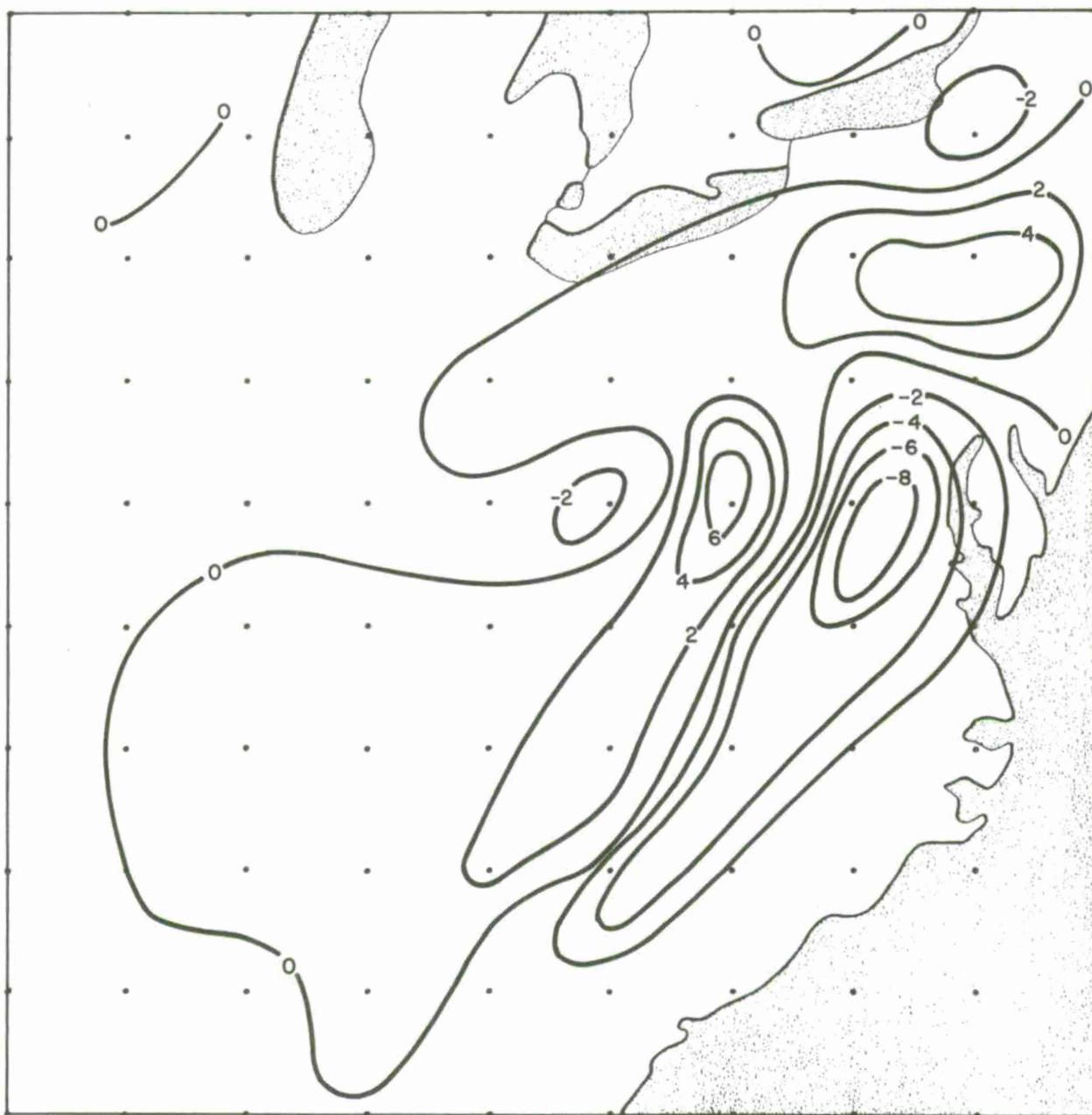


Fig. 4. Case A: predicted terrain-induced vertical velocity (cm sec^{-1}) at verification time.

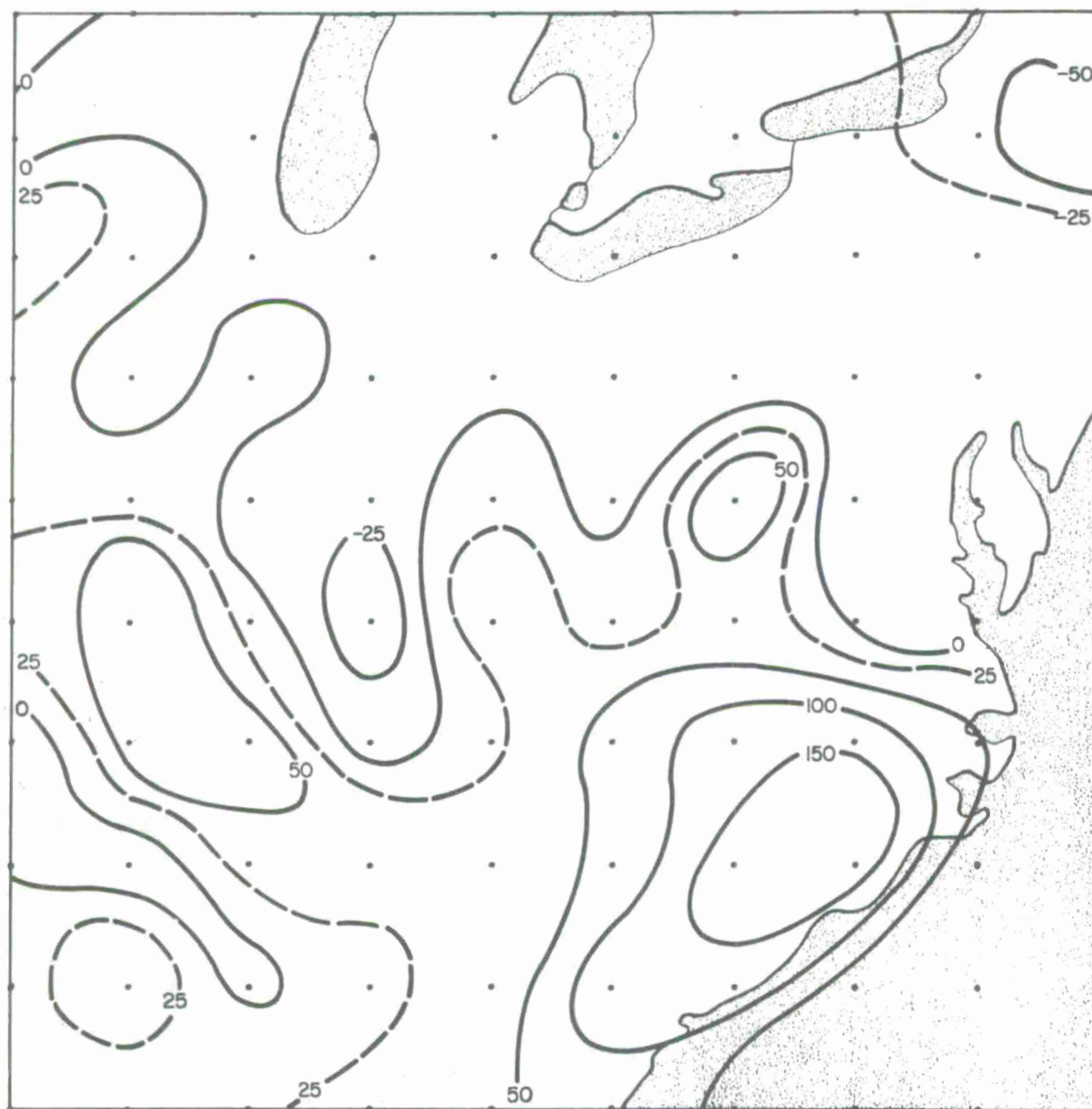


Fig. 5. Case A: net sensible heat (Cal cm^{-2}) added to the transition layer during the forecast period.

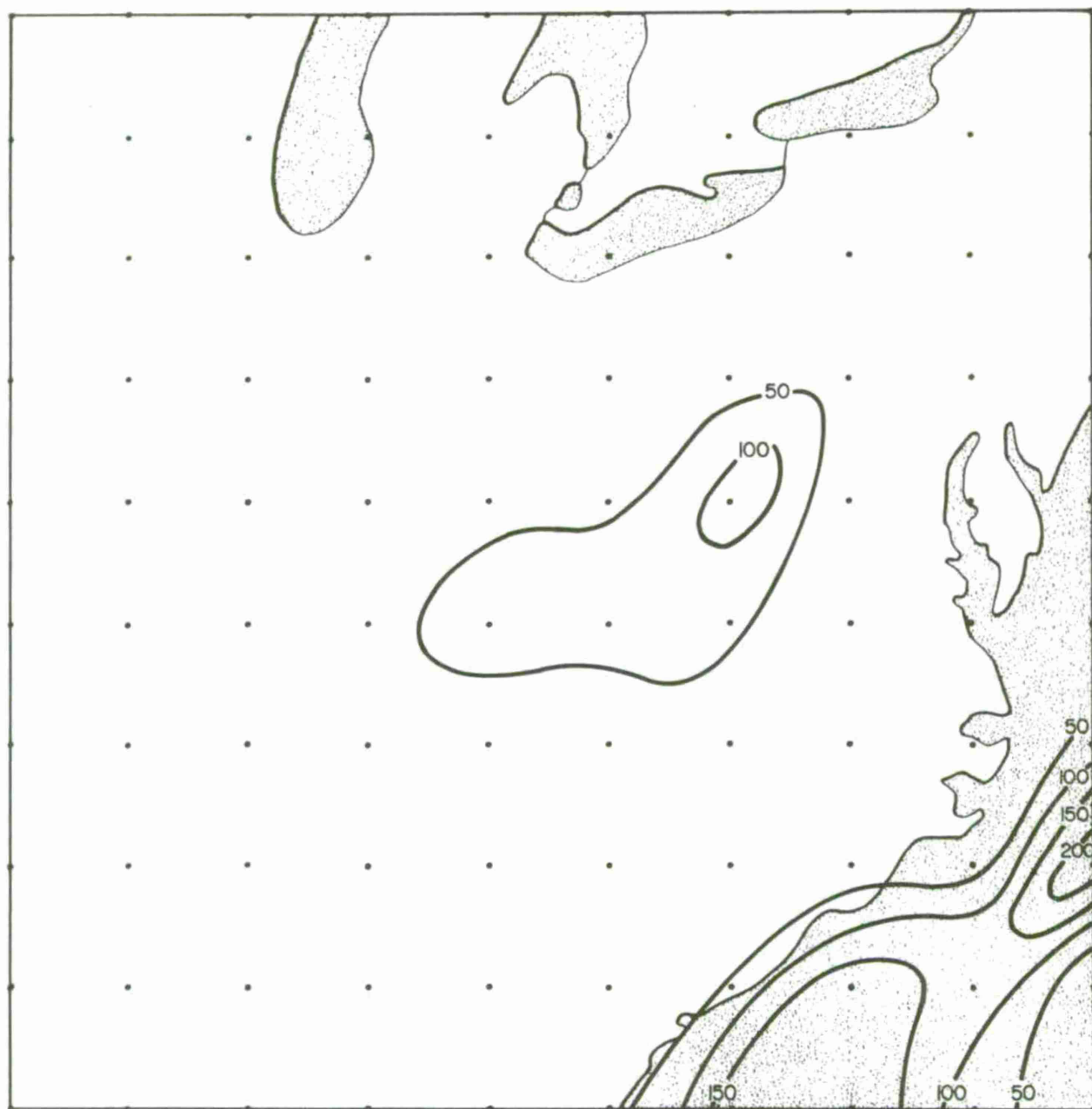


Fig. 6. Case A: net latent heat (Cal cm^{-2}) added to the transition layer during the forecast period.

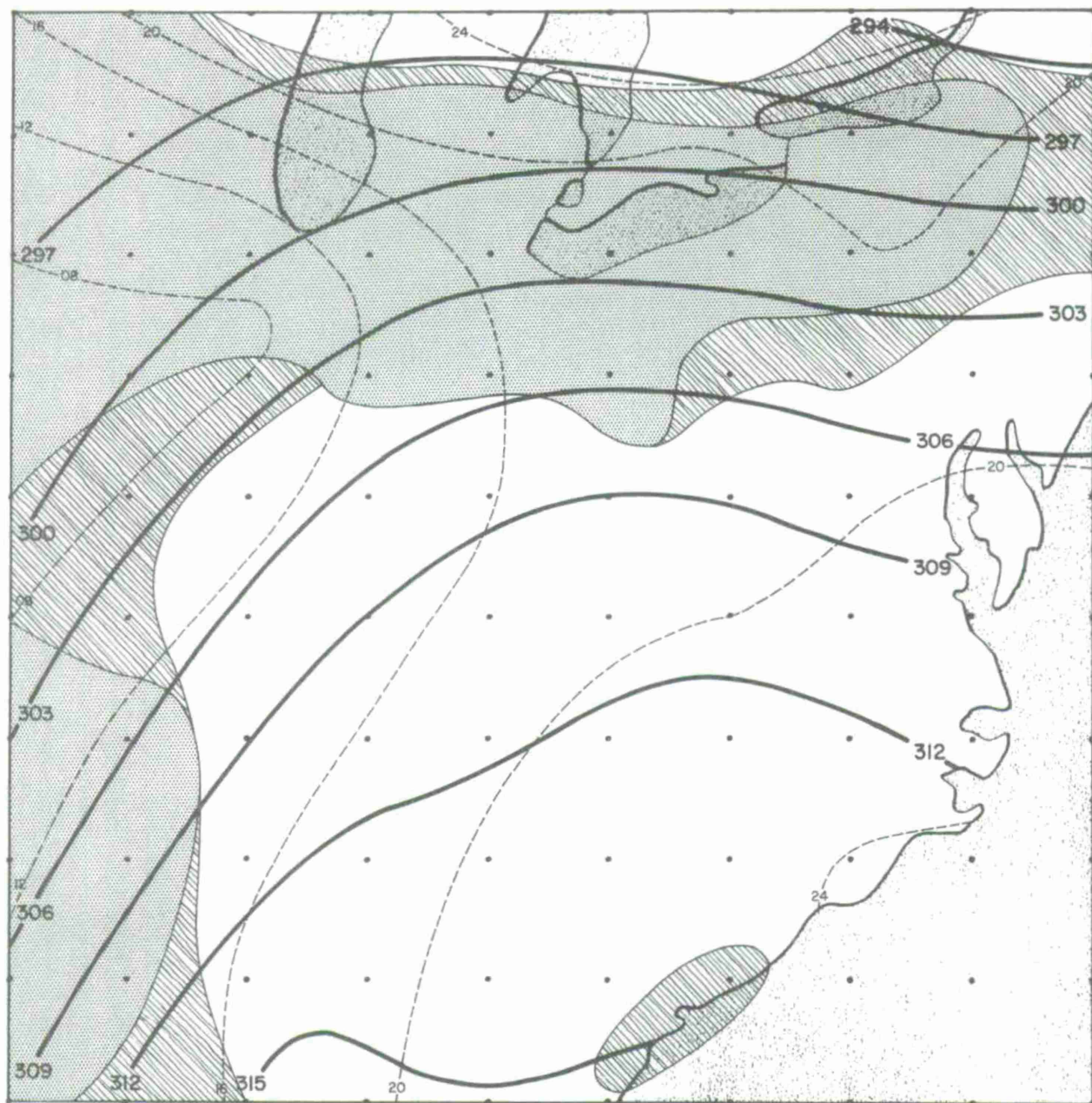






Fig. 7(a). Case B, observed data: surface isobars (mb) and 700-mb contours (tens of meters) at initial time. Shading indicates regions covered by broken or overcast low cloudiness , or experiencing precipitation .



Fig. 7(b). Case B, observed data: surface isobars (mb) and 700-mb contours (tens of meters) at verification time. Shading indicates regions covered by broken or overcast low cloudiness , or experiencing precipitation .

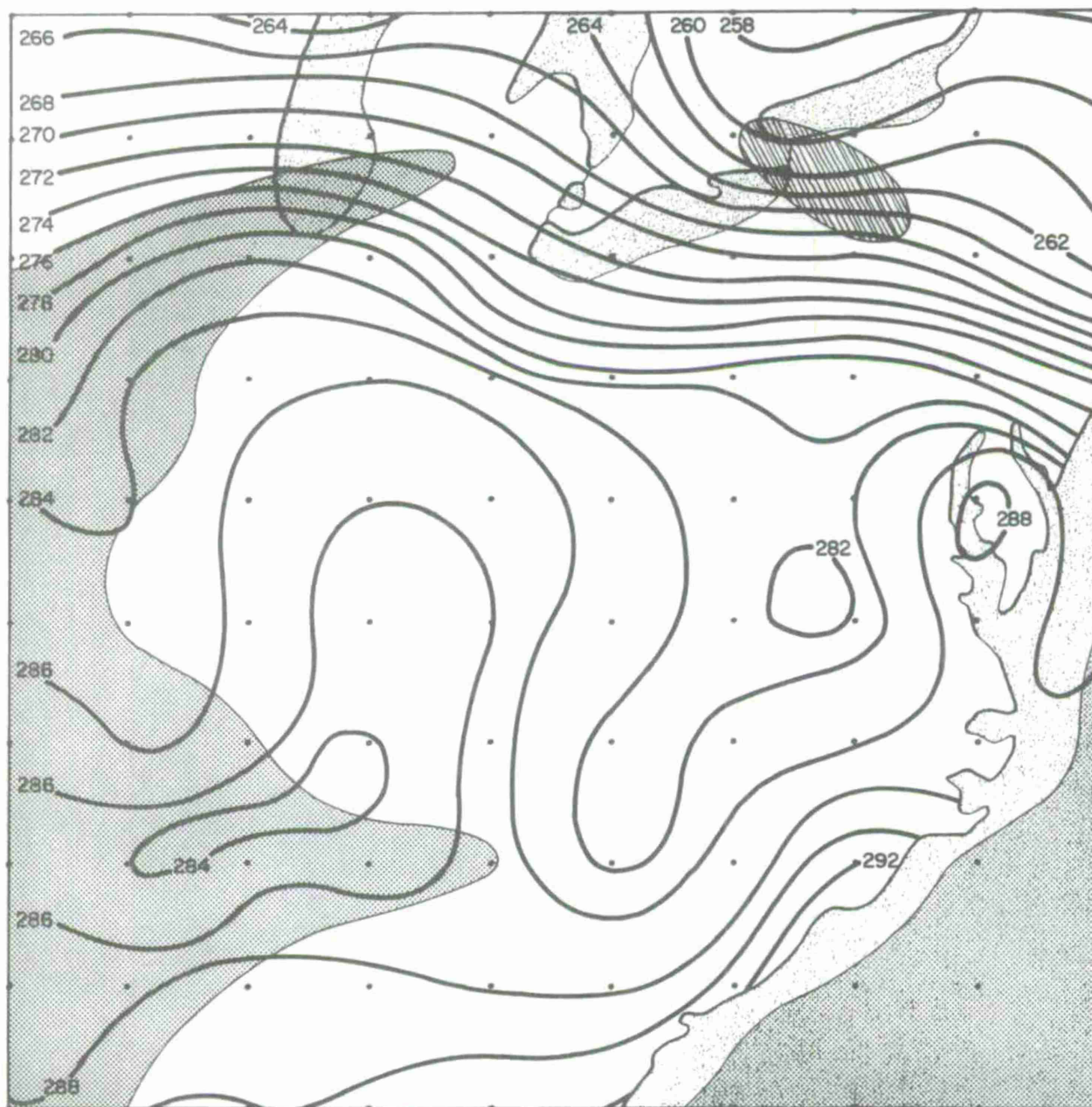



Fig. 7(c). Case B: analysis of observed temperature ($^{\circ}\text{K}$) and humidity at verification time for level 500 m above terrain height. $80\% \leq \text{RH} < 100\%$ 

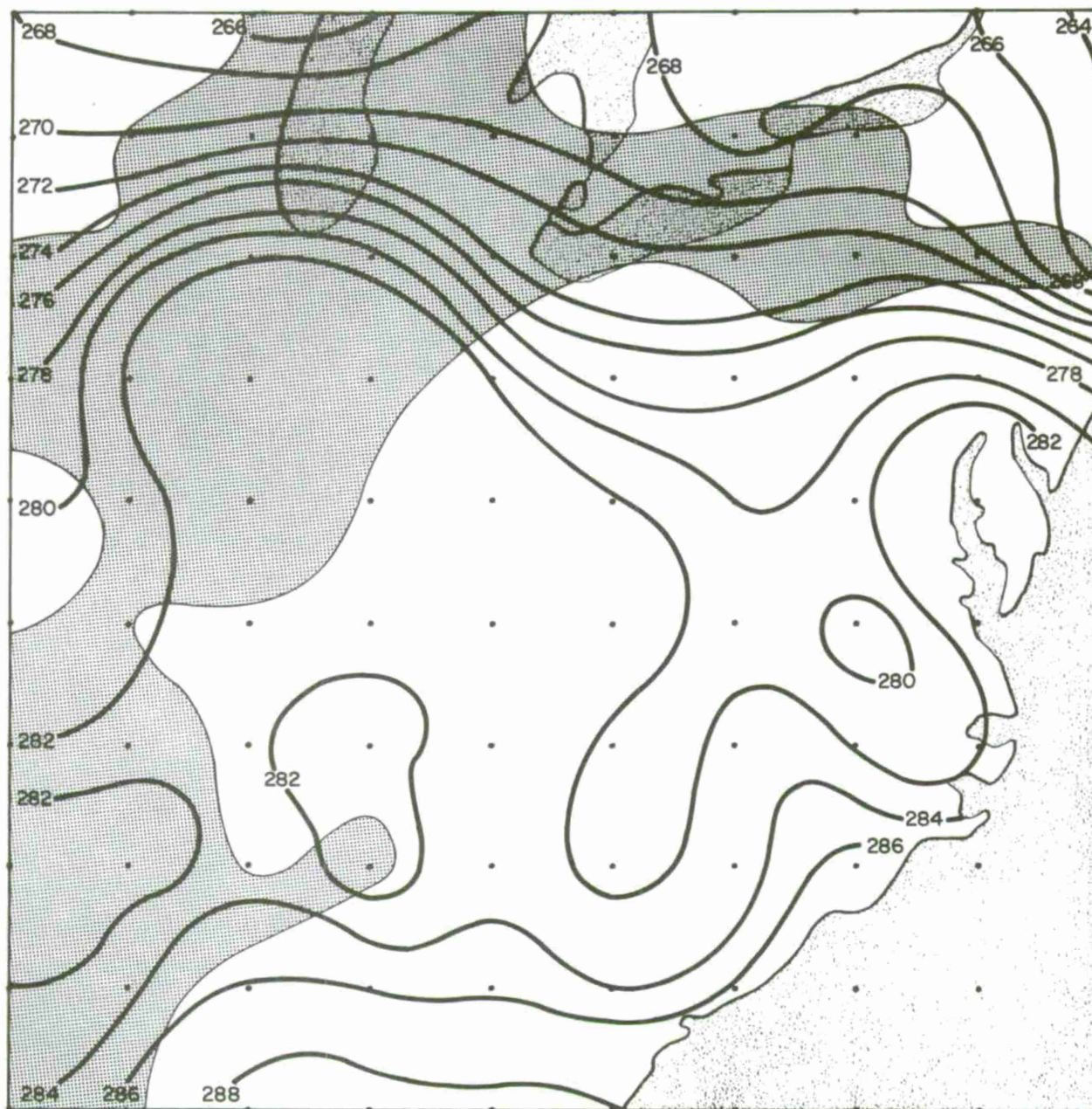



Fig. 7(d). Case B: analysis of observed temperature ($^{\circ}\text{K}$) and humidity at verification time for level 1150 m above terrain height. $80\% \leq \text{RH} < 100\%$ 

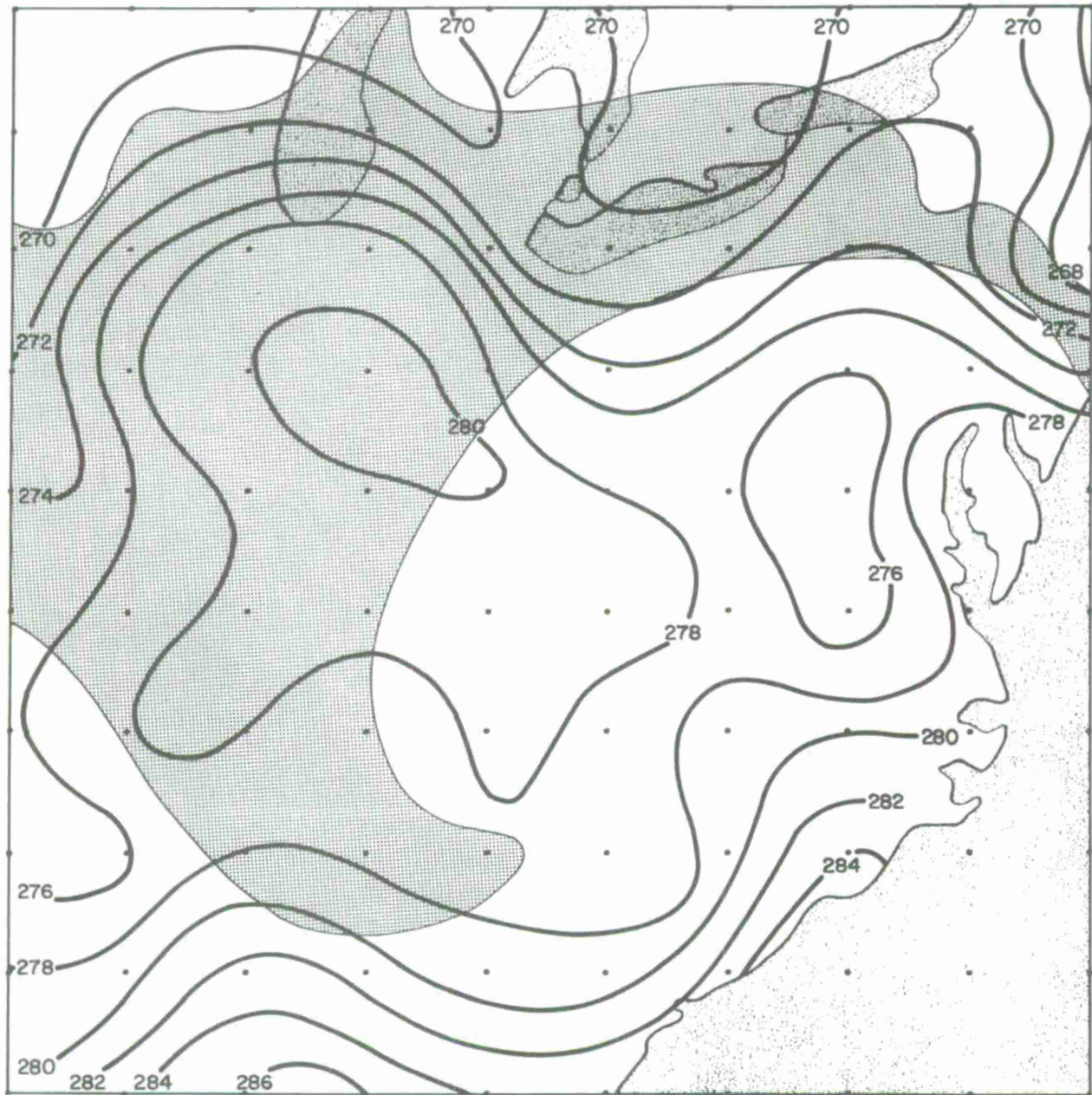



Fig. 7(e). Case B: analysis of observed temperature ($^{\circ}\text{K}$) and humidity at verification time for level 2000 m above terrain height. $80\% \leq \text{RH} < 100\%$ 

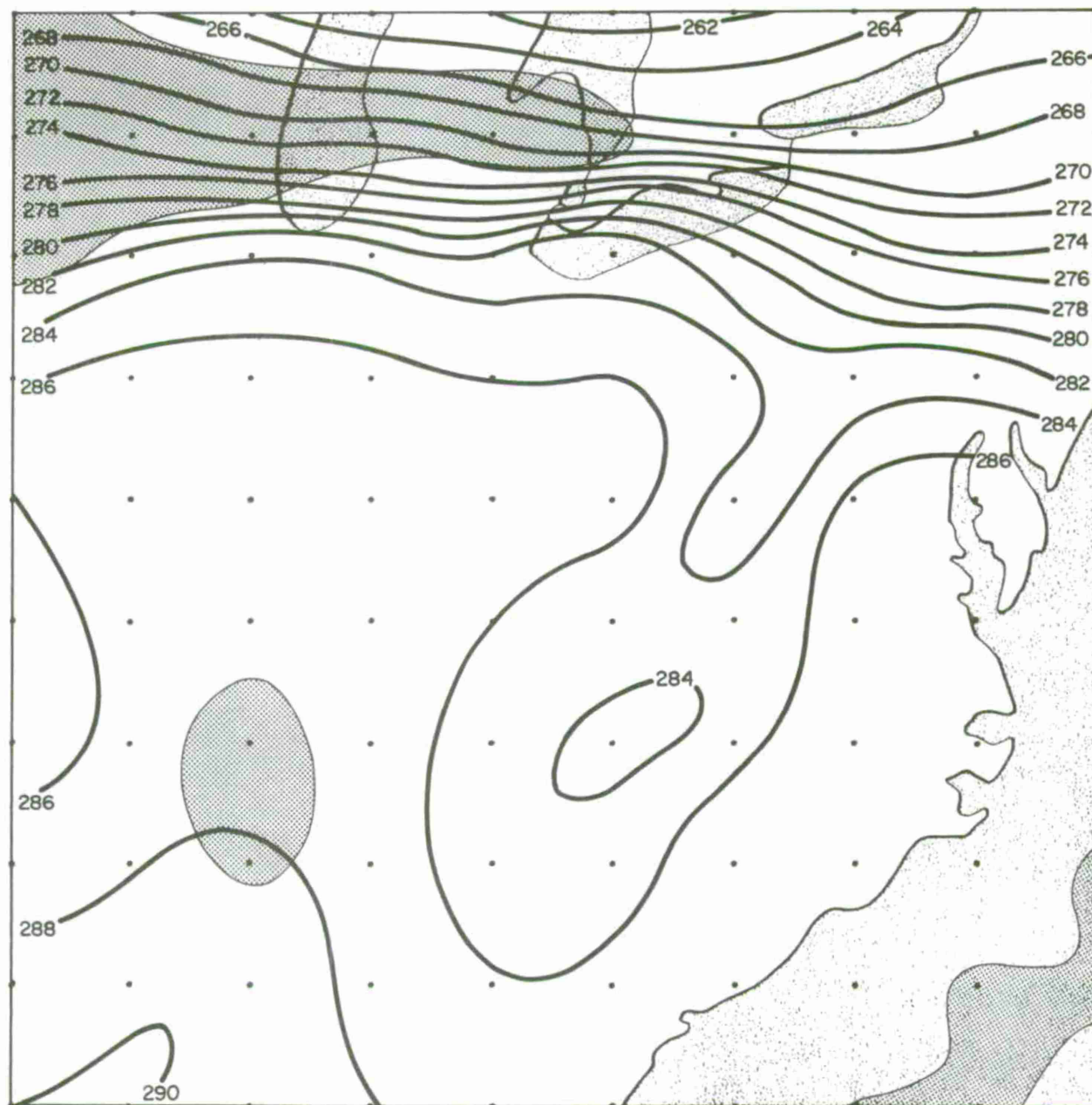




Fig. 7(f). Case B: analysis of predicted temperature (°K) and humidity at verification time for level 500 m above terrain height. $80\% \leq RH < 100\%$  $RH \geq 100\%$ 

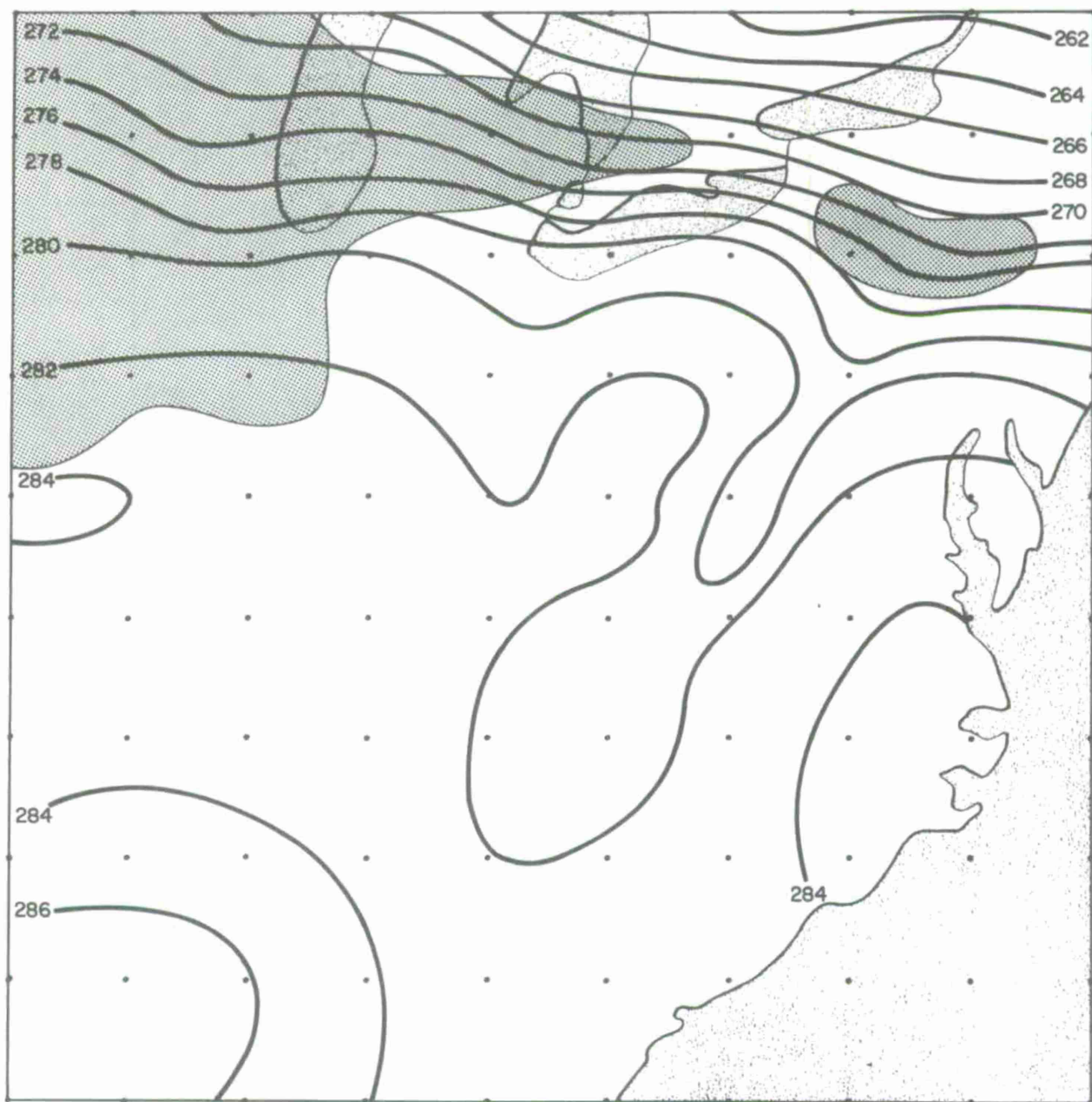




Fig. 7(g). Case B: analysis of predicted temperature ($^{\circ}\text{K}$) and humidity at verification time for level 1150 m above terrain height. $80\% \leq RH < 100\%$  $RH \geq 100\%$ 

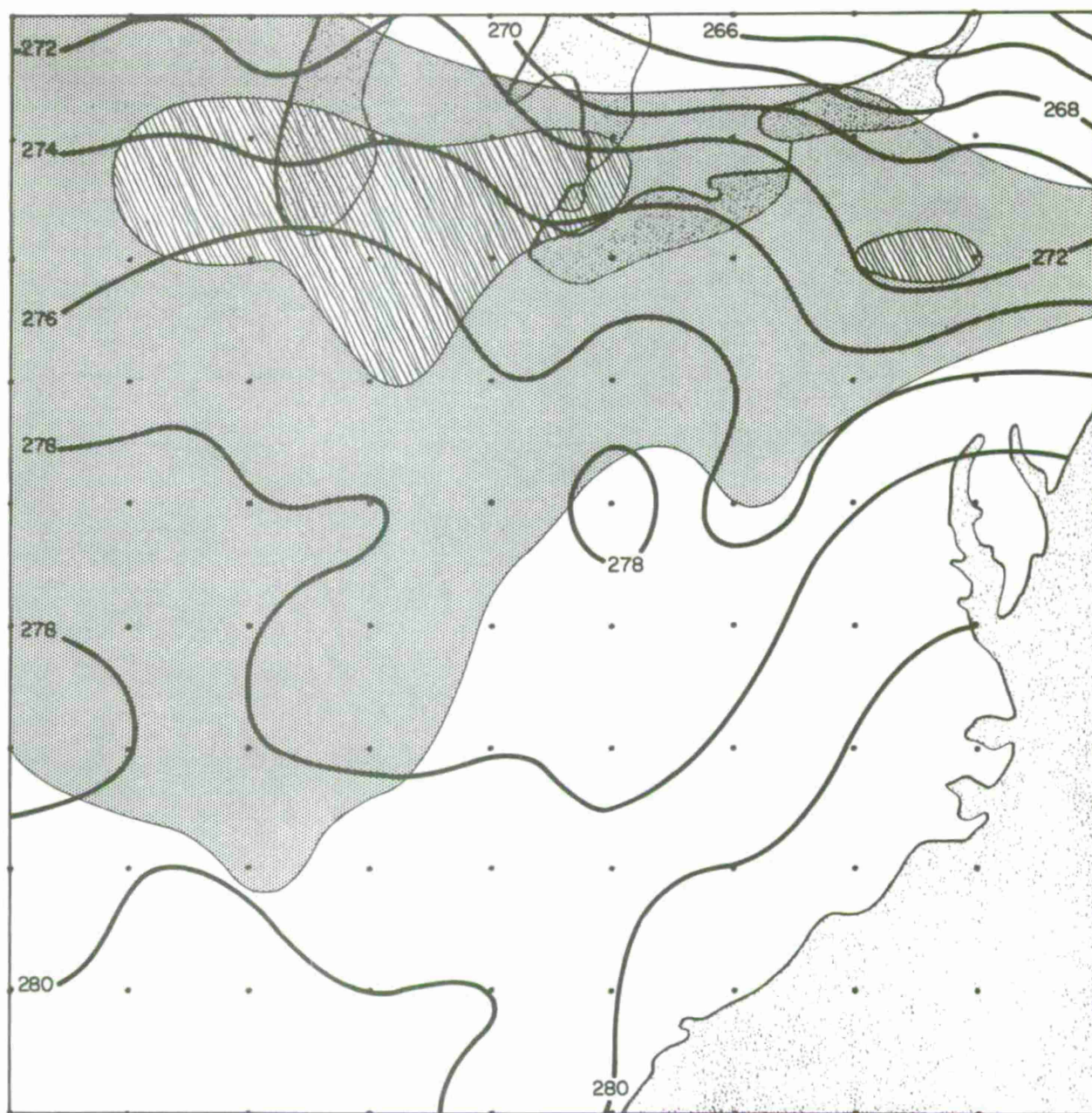




Fig. 7(h). Case B: analysis of predicted temperature ($^{\circ}\text{K}$) and humidity at verification time for level 2000 m above terrain height. $80\% \leq RH < 100\%$  $RH \geq 100\%$ 

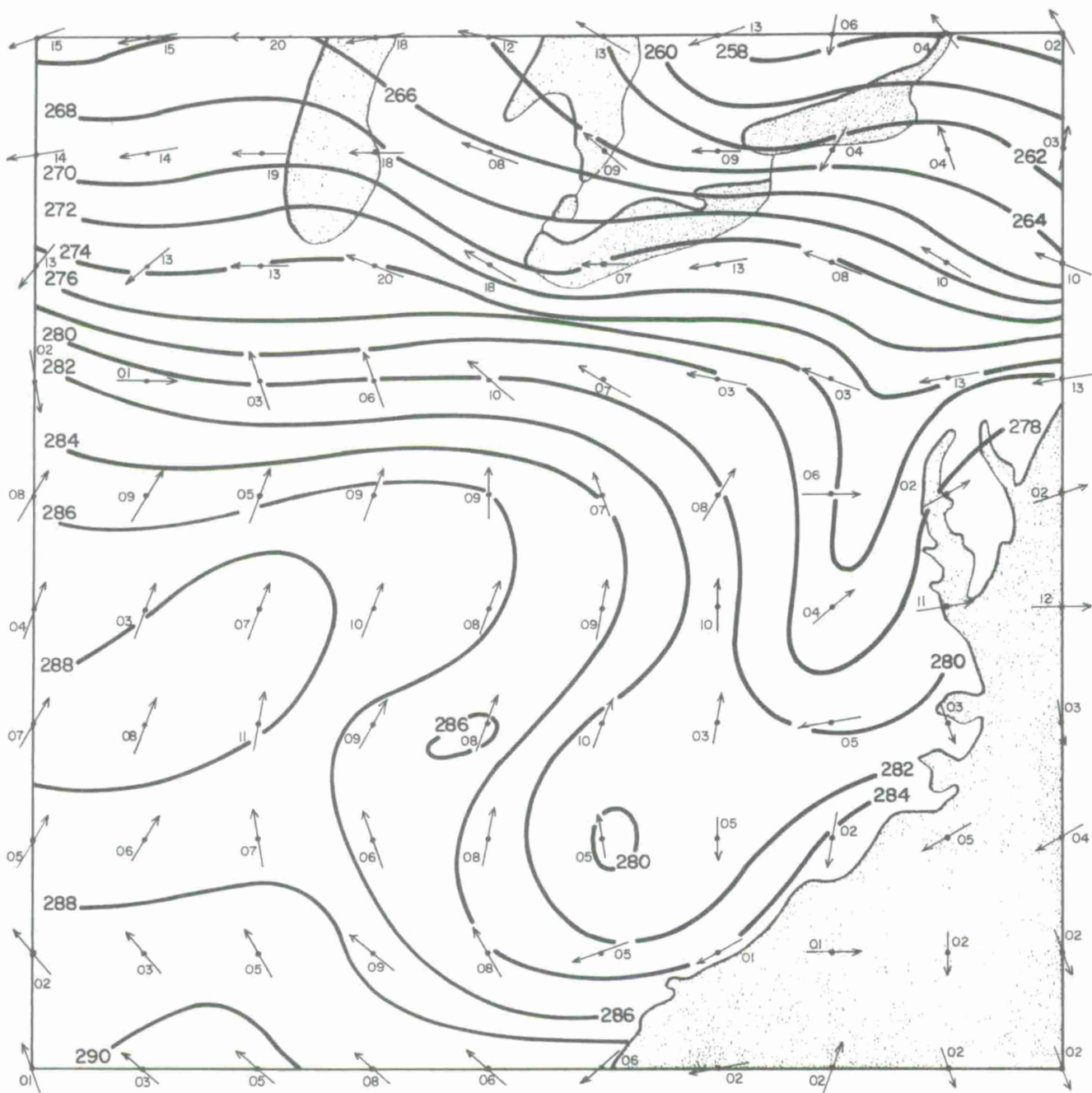


Fig. 7(i). Case B: analysis of observed surface isotherms ($^{\circ}\text{K}$) and derived 50-m wind field at verification time (arrows indicate wind direction; numbers indicate wind speed in m sec^{-1}).

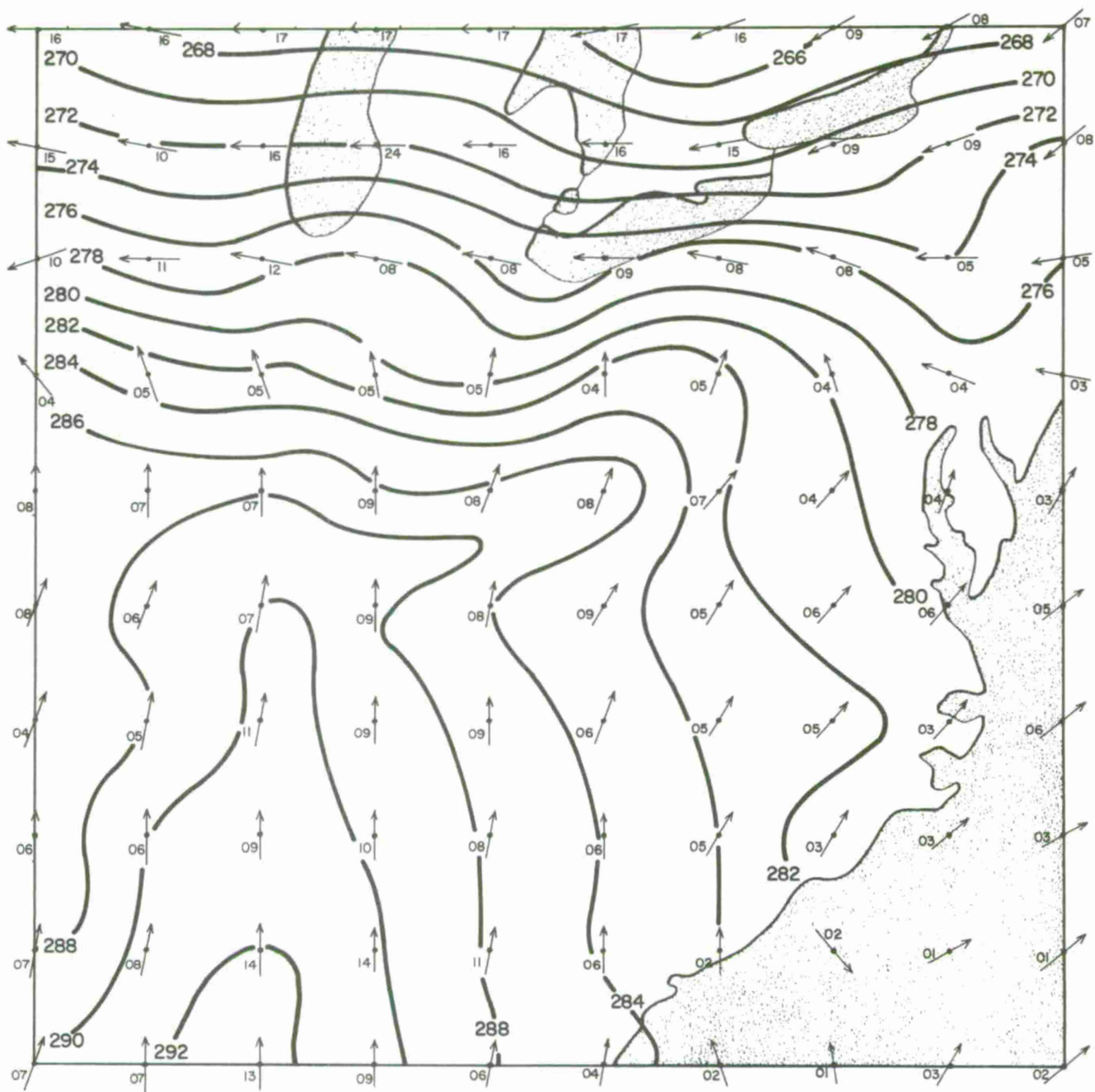


Fig. 7(j). Case B: prognosis of surface isotherms ($^{\circ}\text{K}$) and 50-m wind field valid at verification time (arrows indicate wind direction; numbers indicate wind speed in m sec^{-1}).

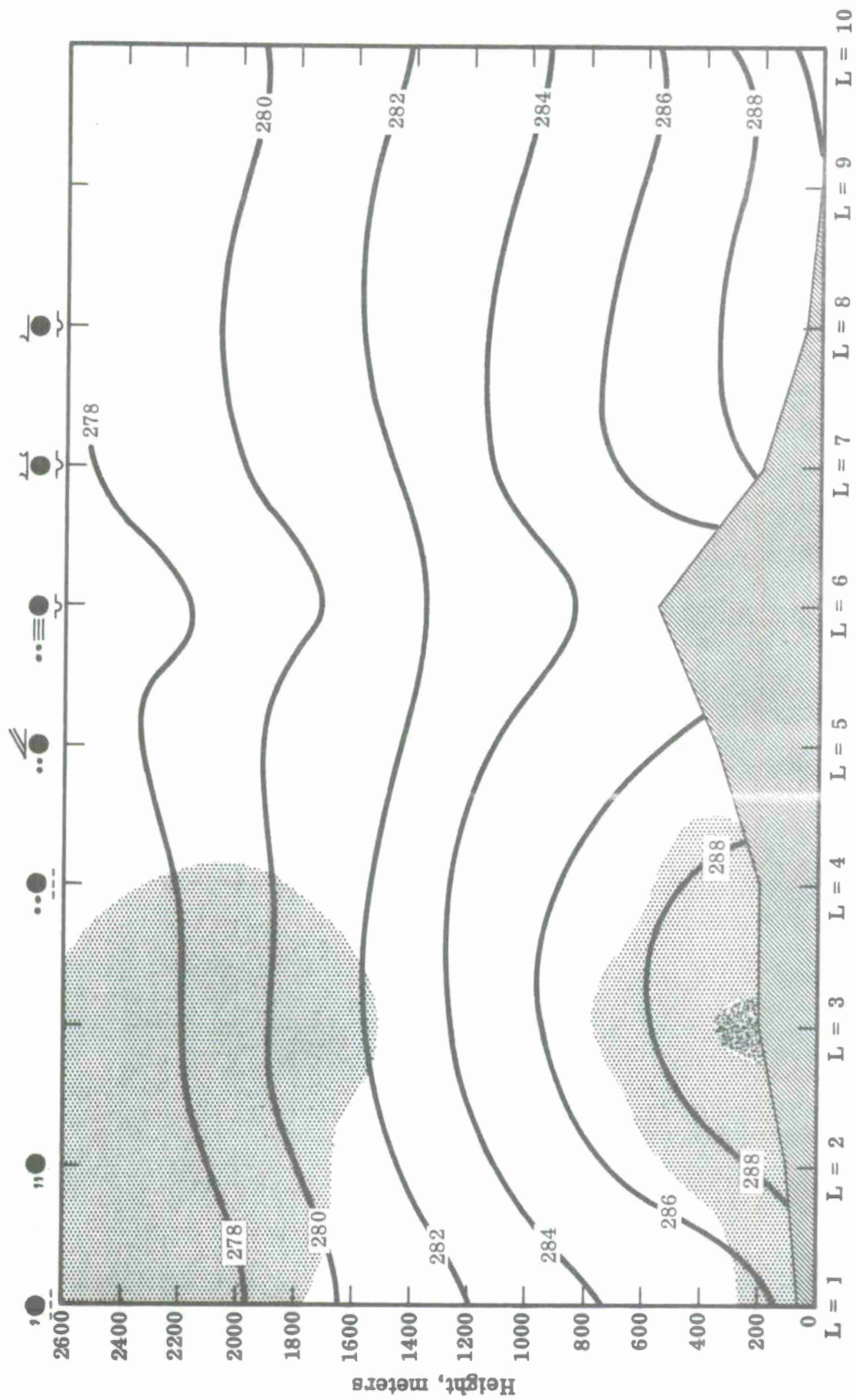


Fig. 7(k). Case B: vertical cross section along grid row M = 4 showing predicted temperature ($^{\circ}\text{K}$) and humidity, and observed sky condition and weather (at top of figure), valid at verification time. $\text{RH} < 100\%$ $\text{RH} = 100\%$

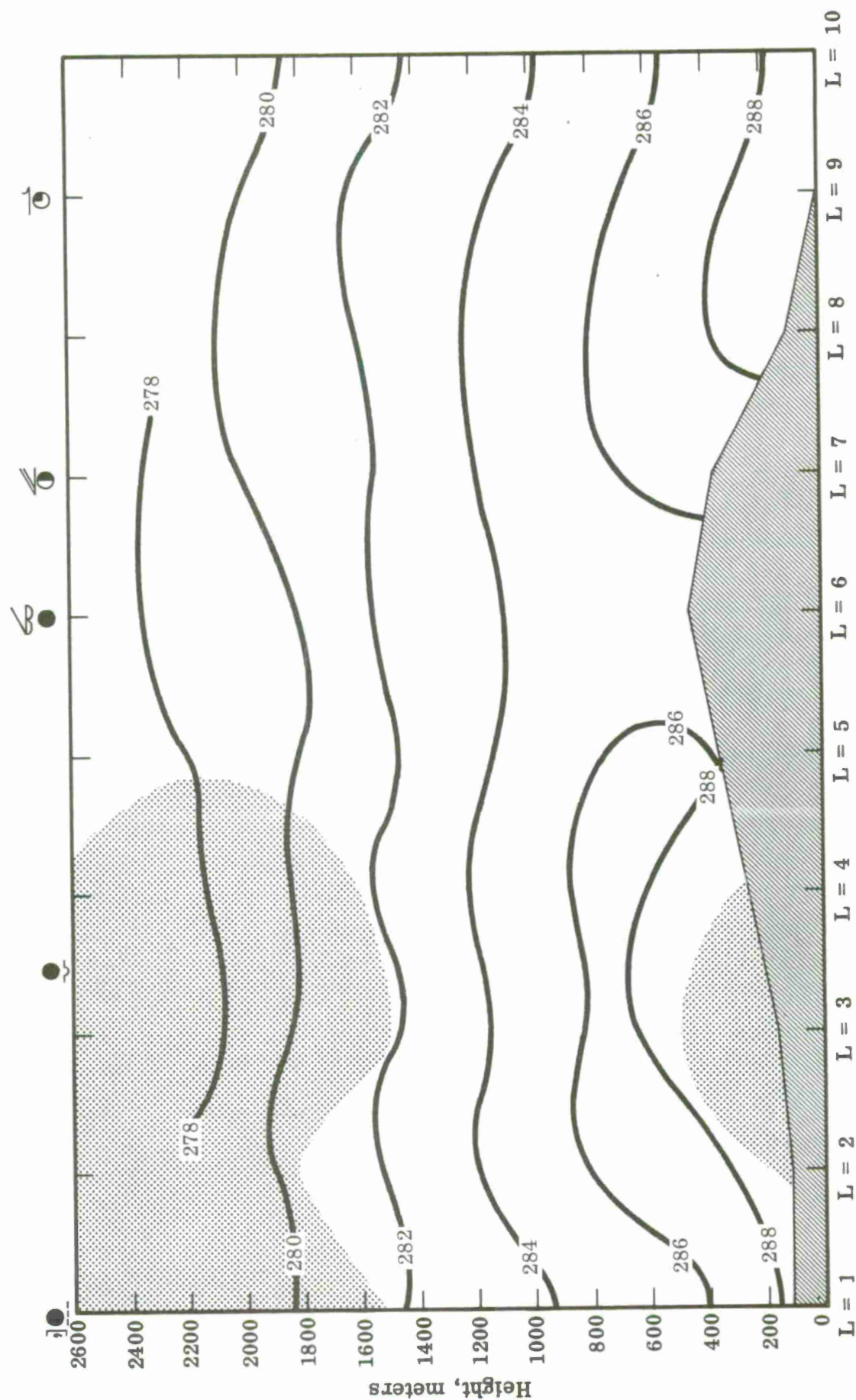


Fig. 7(1). Case B: vertical cross section along grid row M = 5 showing predicted temperature (°K) and humidity, and observed sky condition and weather (at top of figure), valid at verification time. RH < 100% RH ≥ 100%

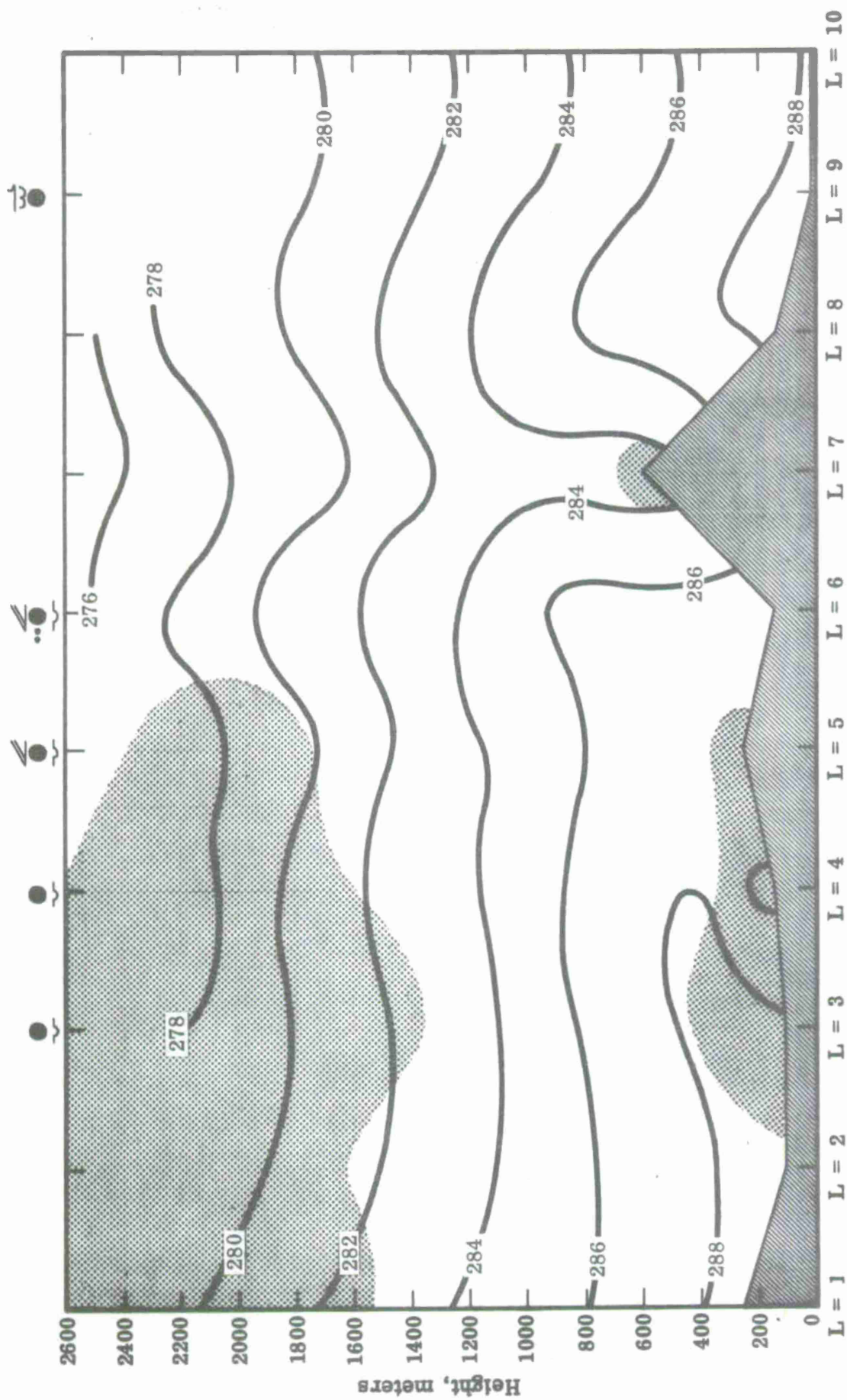


Fig. 7(m). Case B: vertical cross section along grid row M = 6 showing predicted temperature ($^{\circ}\text{K}$) and humidity, and observed sky condition and weather (at top of figure), valid at verification time. $\text{RH} < 100\%$  $\text{RH} \geq 100\%$ 

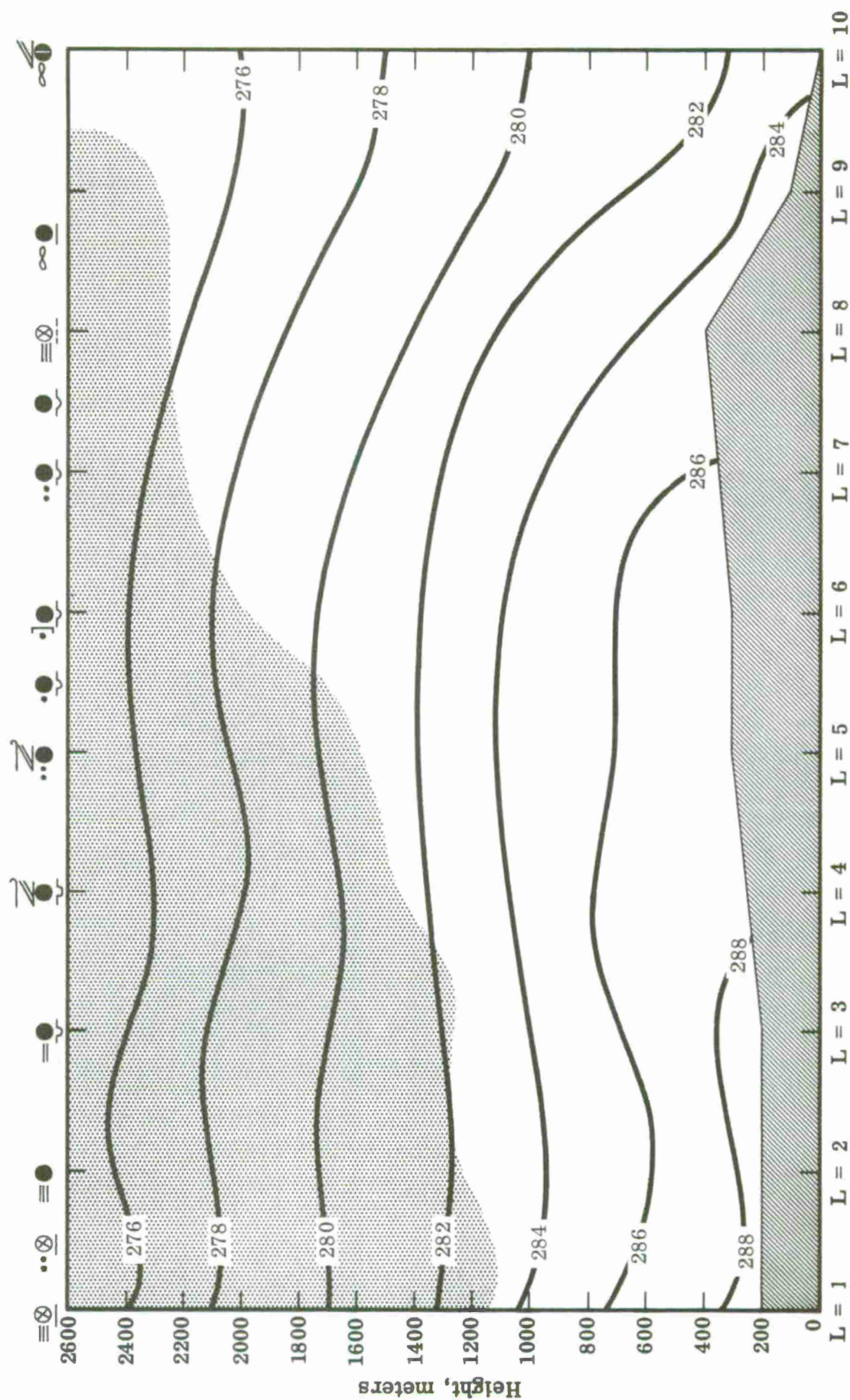


Fig. 7(n). Case B: vertical cross section along grid row $M = 7$ showing predicted temperature ($^{\circ}\text{K}$) and humidity, and observed sky condition and weather (at top of figure), valid at verification time. $80\% \leq \text{RH} < 100\%$ $\text{RH} \geq 100\%$

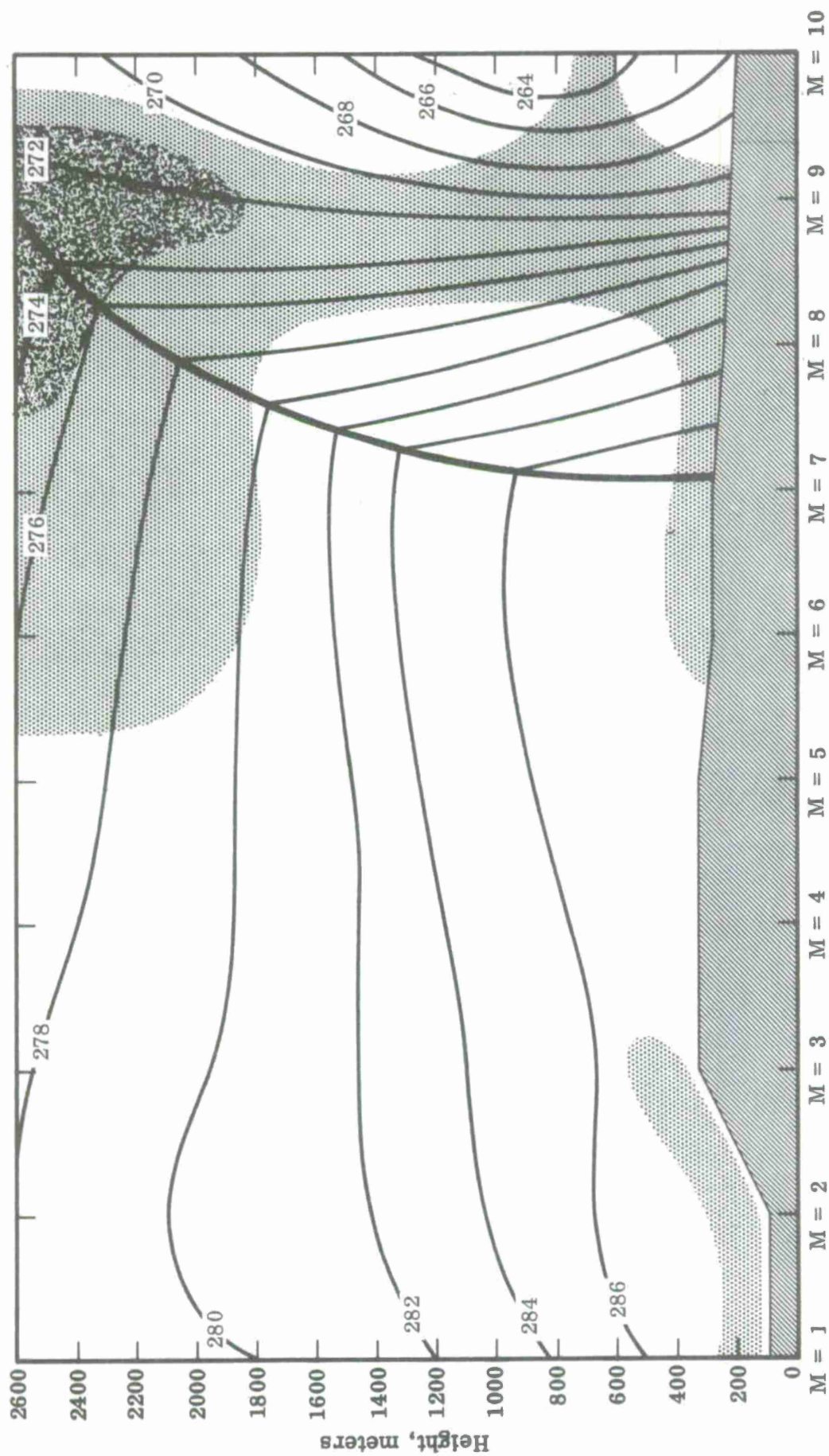


Fig. 8. Case B: south-to-north vertical cross section of temperature ($^{\circ}\text{K}$) and humidity along the coordinate line $L = 5$ (solid line indicates frontal position). $80\% \leq \text{RH} < 100\%$  $\text{RH} \geq 100\%$ .

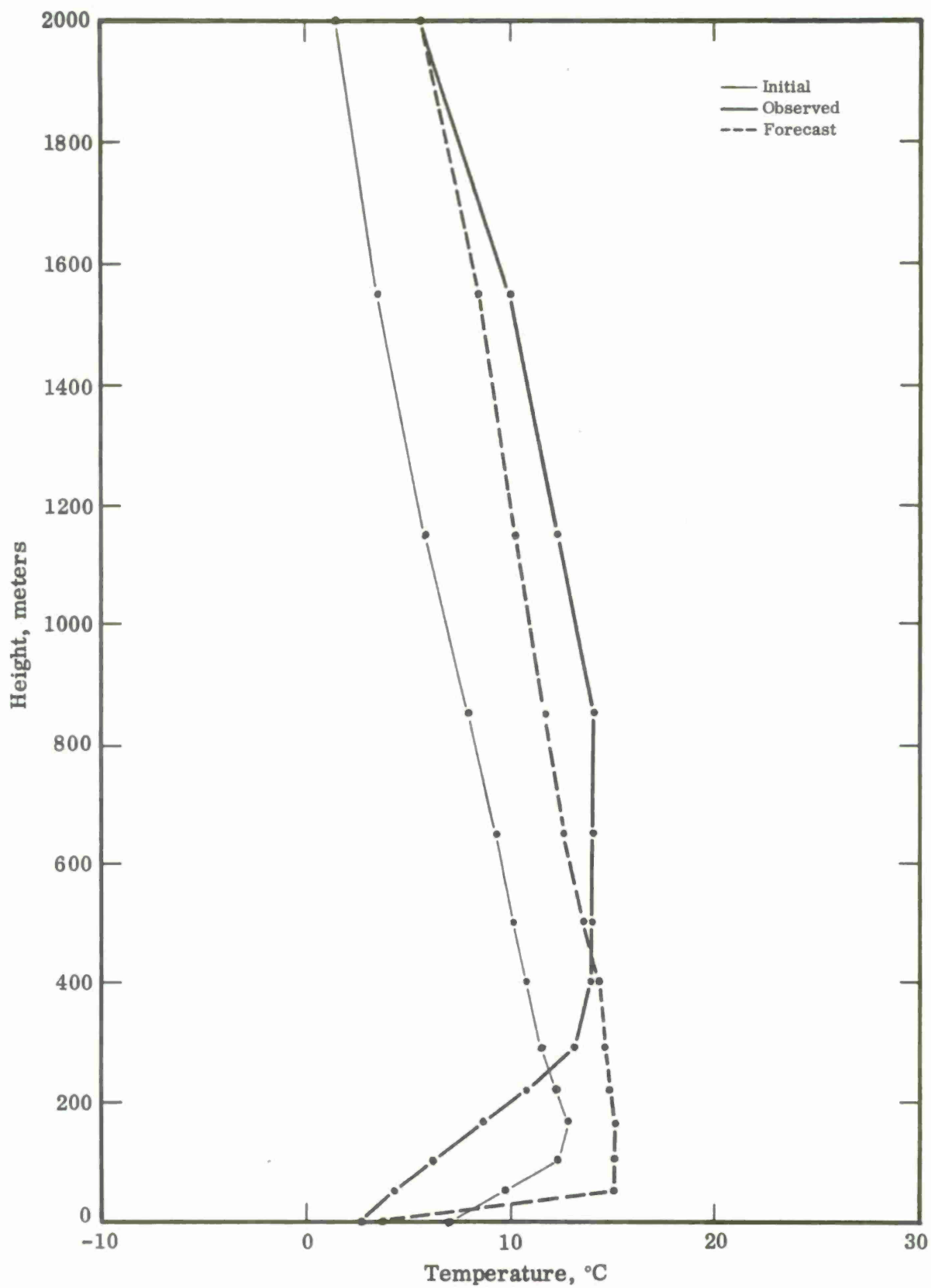


Fig. 9. Case B: initial and predicted temperature structure at grid point $L = 9$, $M = 6$, and observed (at verification time) structure at a nearby radio-sonde station.

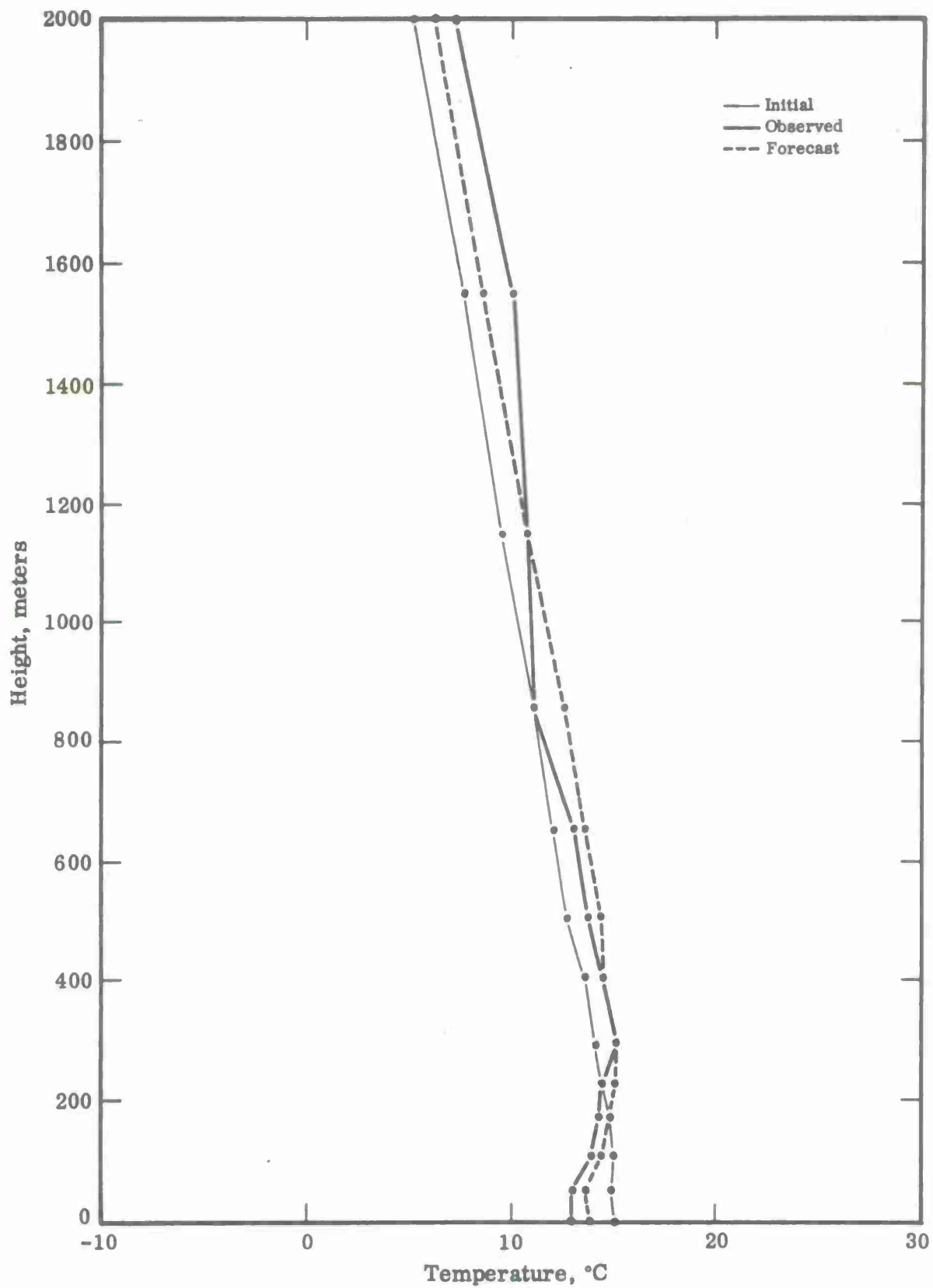


Fig. 10. Case B: initial and predicted temperature structure at grid point $L = 6$, $M = 6$, and observed (at verification time) structure at a nearby radio-sonde station.

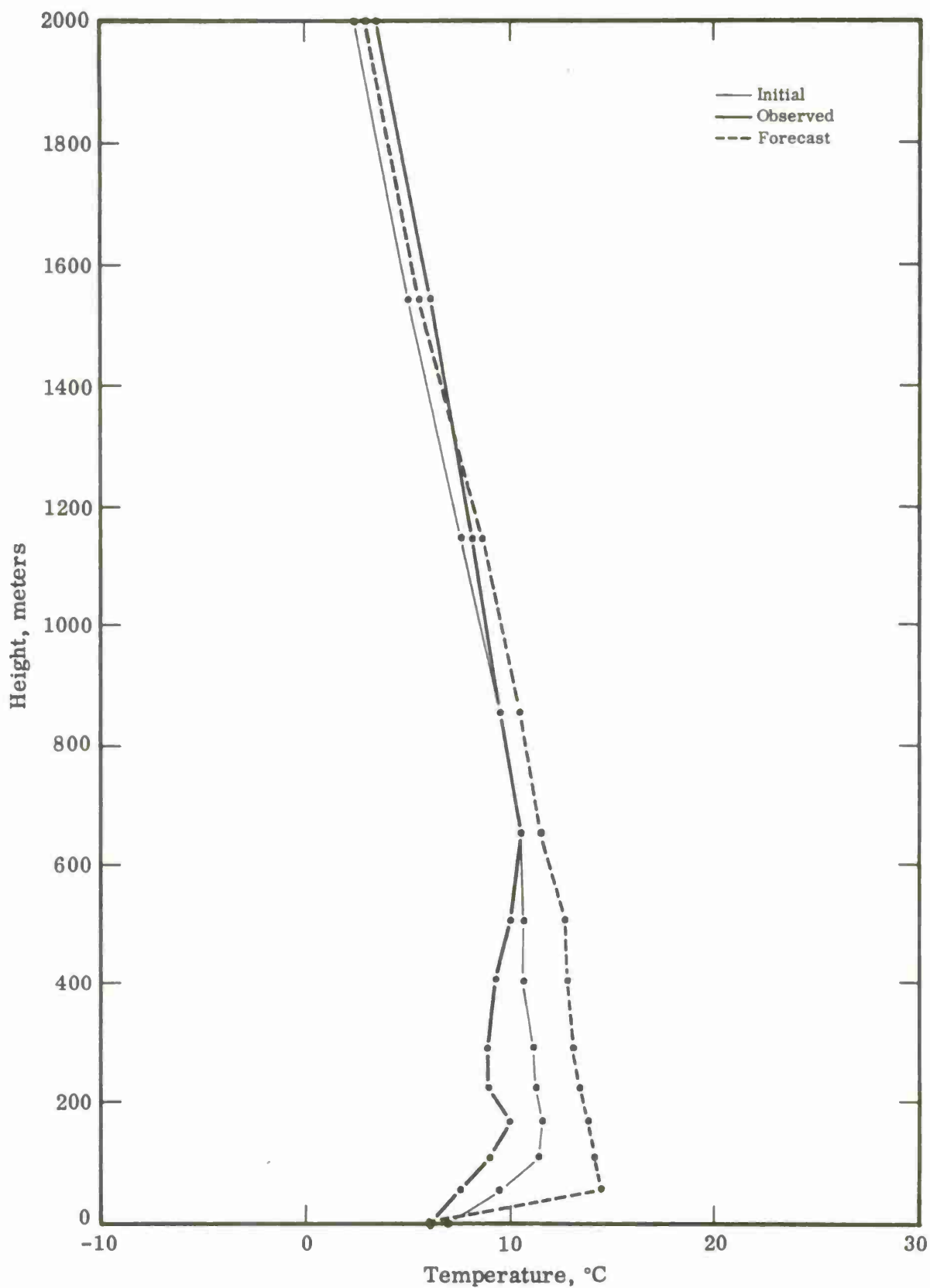


Fig. 11. Case B: initial and predicted temperature structure at grid point $L = 5$, $M = 7$, and observed (at verification time) structure at a nearby radio-sonde station.

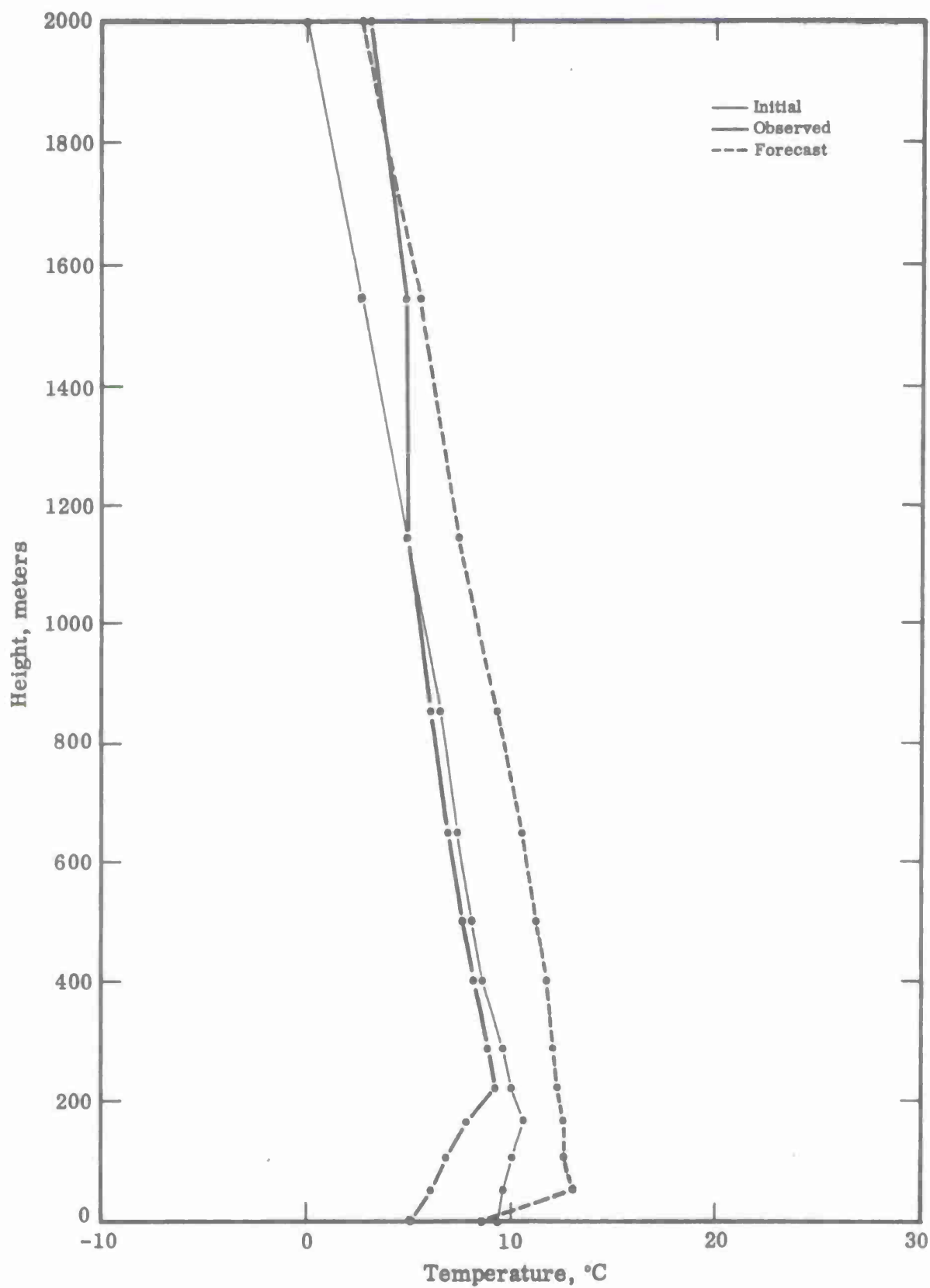


Fig. 12. Case B: initial and predicted temperature structure at grid point $L = 7$, $M = 7$, and observed (at verification time) structure at a nearby radio-sonde station.

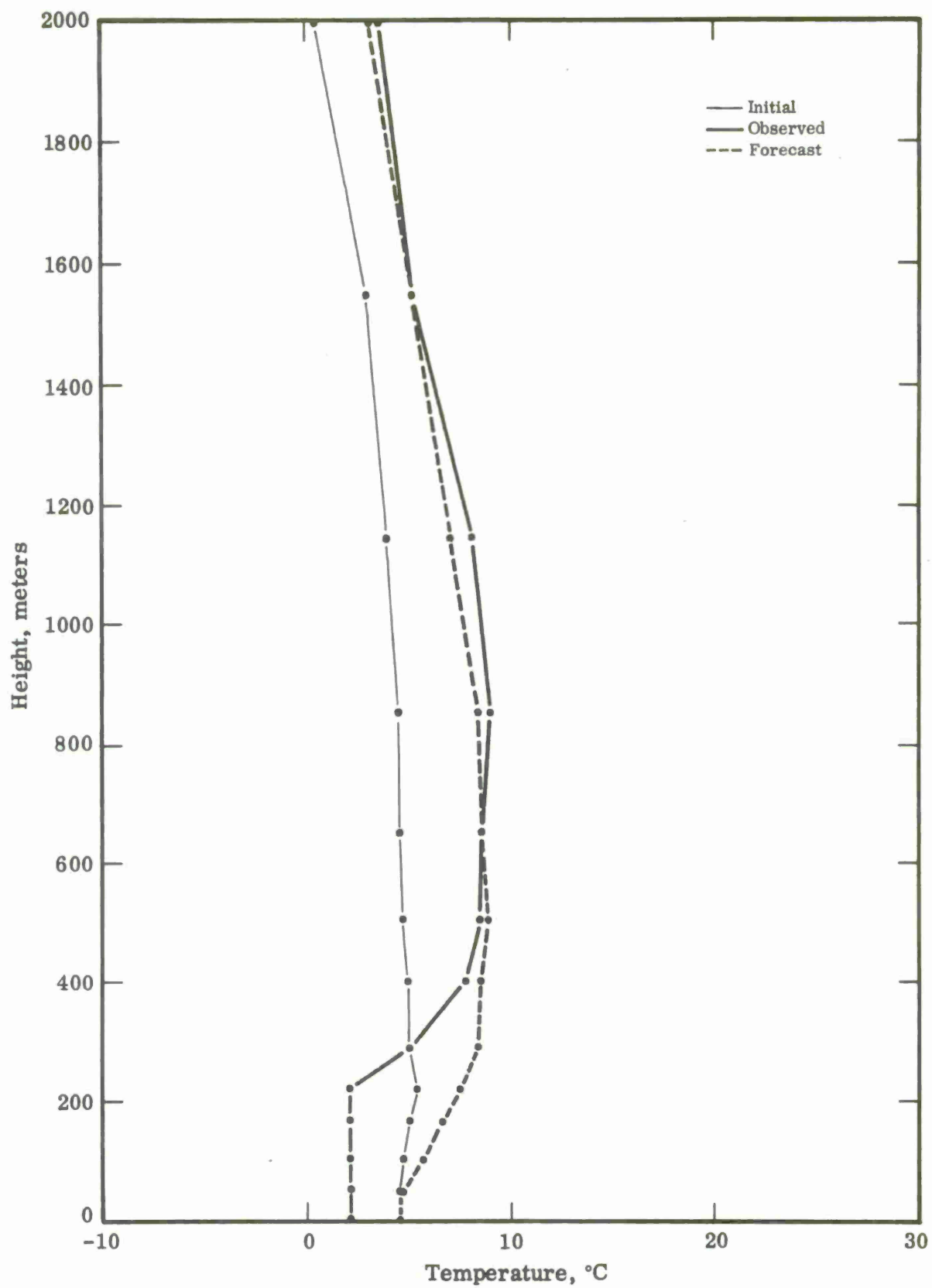


Fig. 13. Case B: initial and predicted temperature structure at grid point $L = 2$, $M = 8$, and observed (at verification time) structure at a nearby radio-sonde station.

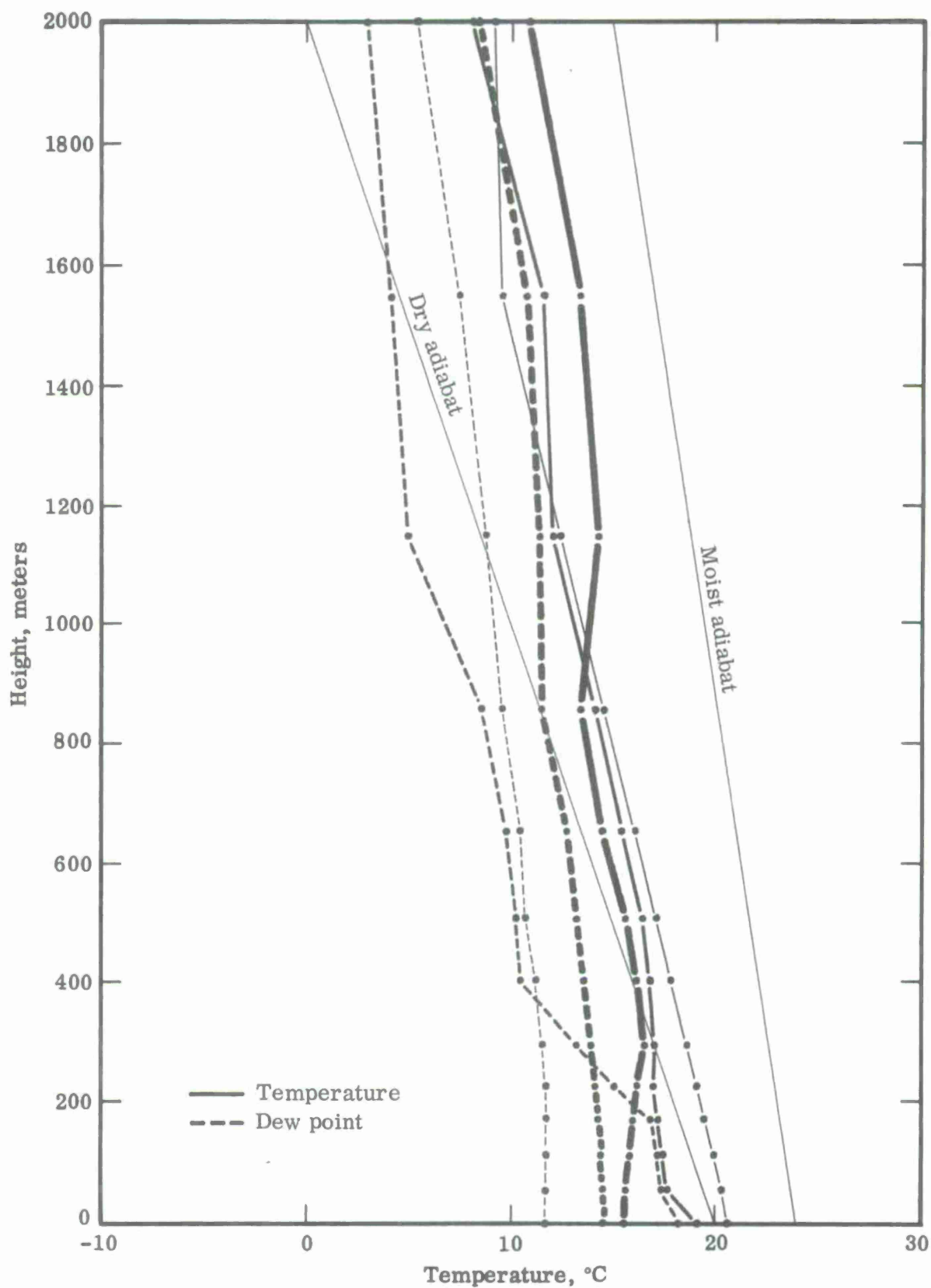


Fig. 14. Case B: temperature and dew-point observations at radiosonde station 226 for initial (fine lines) and final (heavy lines) times of the forecast, and their values (medium lines) predicted at the nearby grid point.

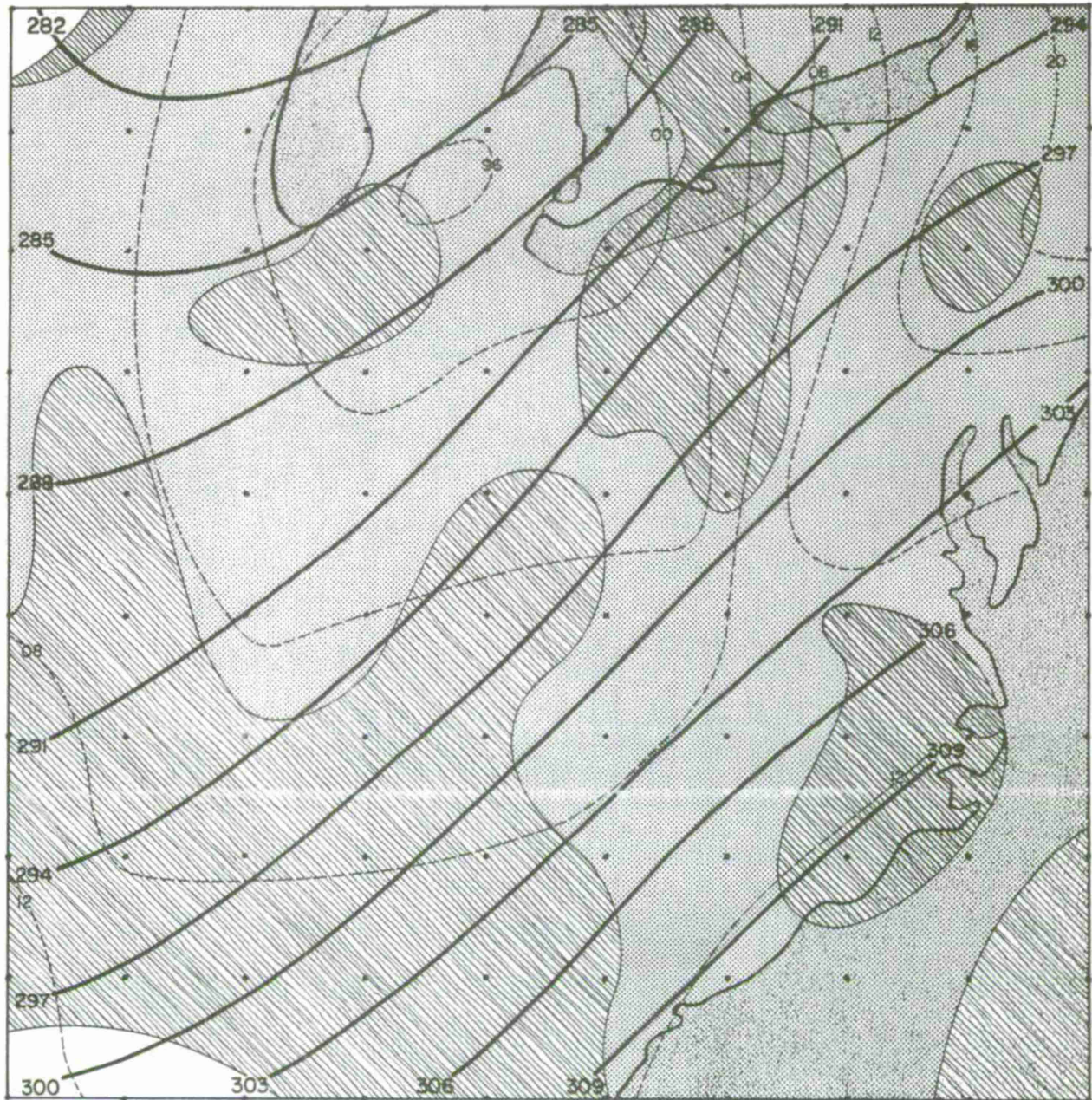




Fig. 15(a). Case C, observed data: surface isobars (mb) and 700-mb contours (tens of meters) at initial time. Shading indicates regions covered by broken or overcast low cloudiness , or experiencing precipitation .

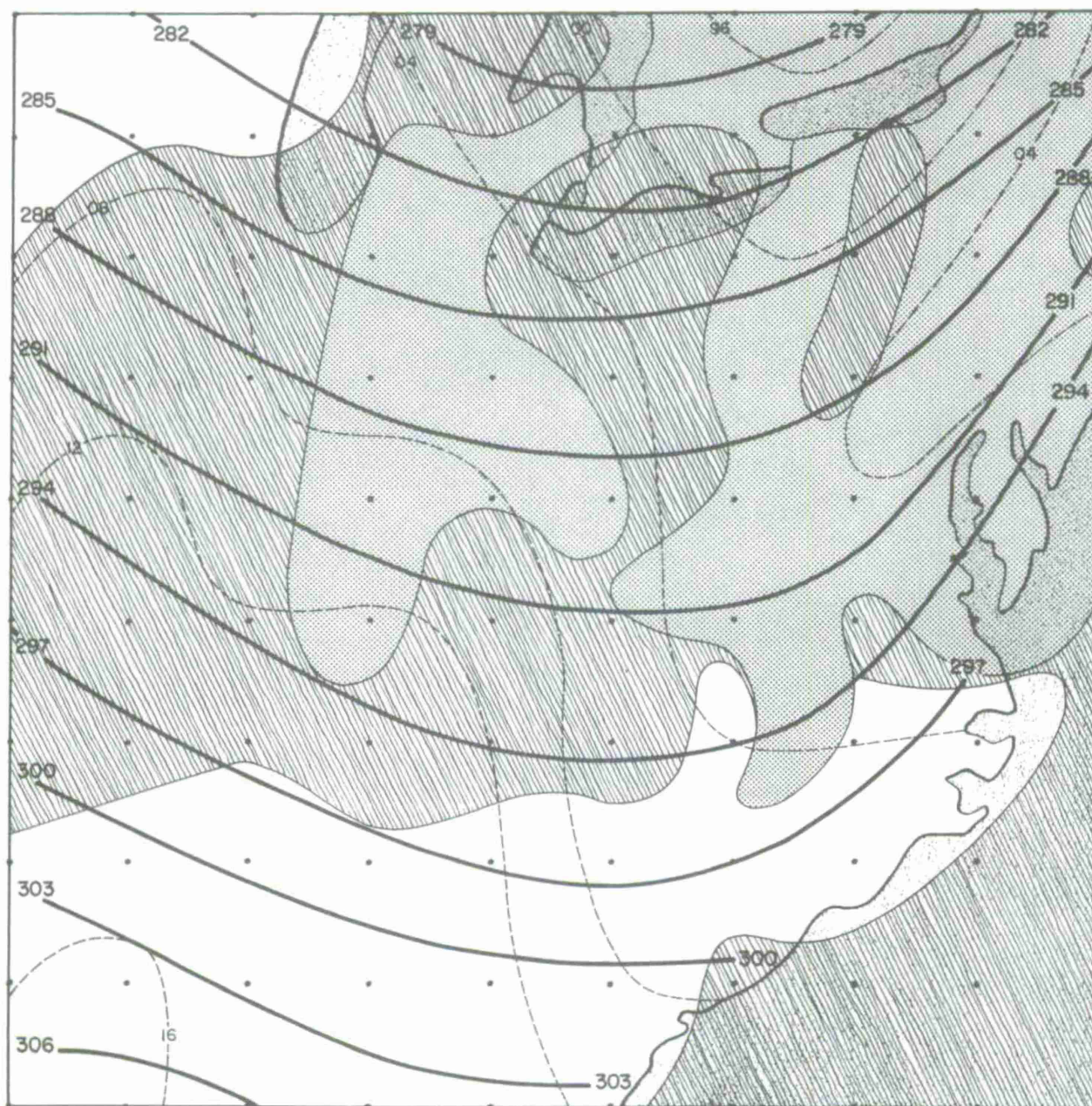




Fig. 15(b). Case C, observed data: surface isobars (mb) and 700-mb contours (tens of meters) at verification time. Shading indicates regions covered by broken or overcast low cloudiness , or experiencing precipitation .

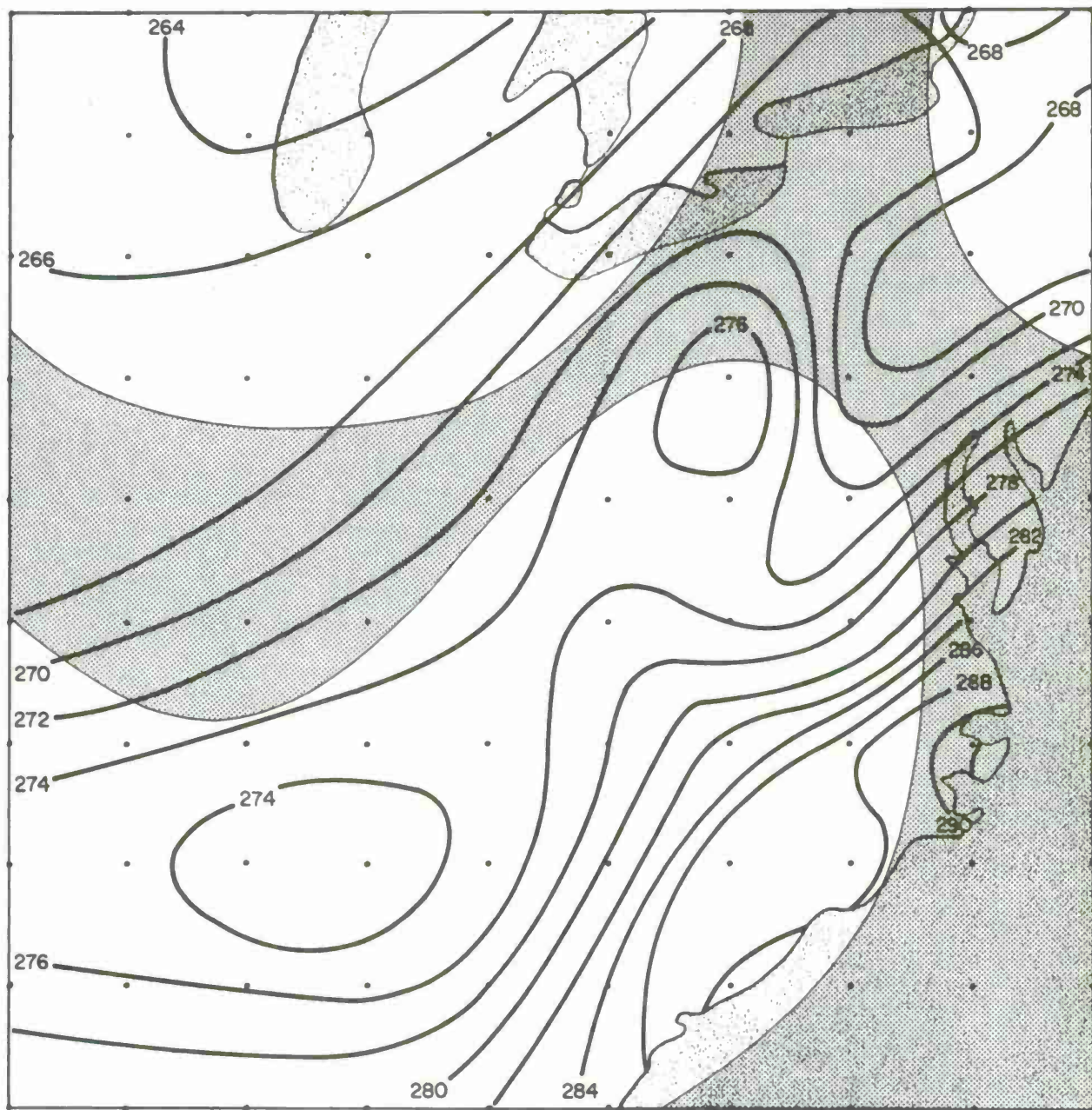


Fig. 15(c). Case C: analysis of observed temperature ($^{\circ}\text{K}$) and humidity at verification time for level 500 m above terrain height. $80\% \leq \text{RH} < 100\%$ [shaded]

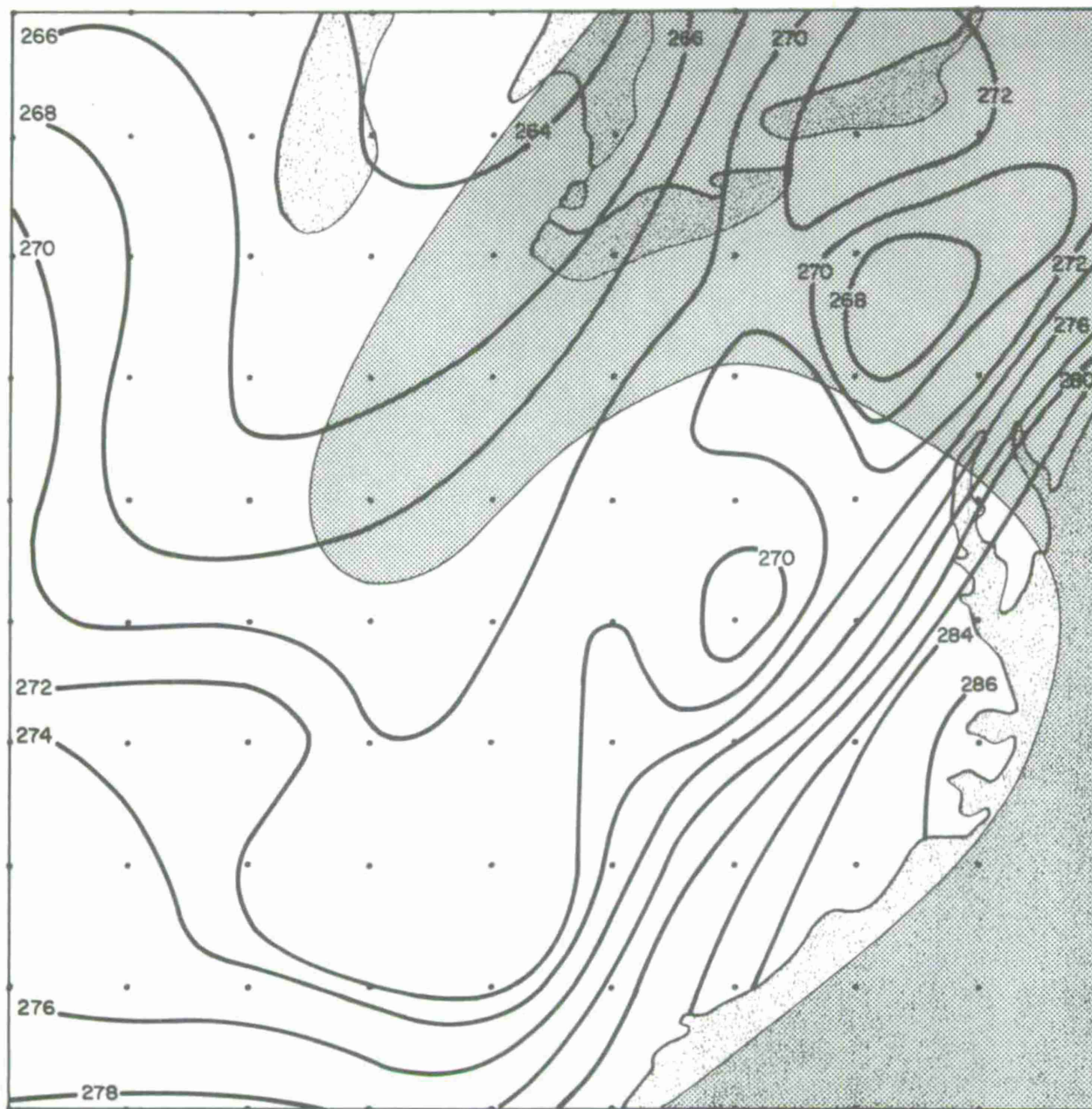



Fig. 15(d). Case C: analysis of observed temperature ($^{\circ}\text{K}$) and humidity at verification time for level 1150 m above terrain height. $80\% \leq \text{RH} < 100\%$ 

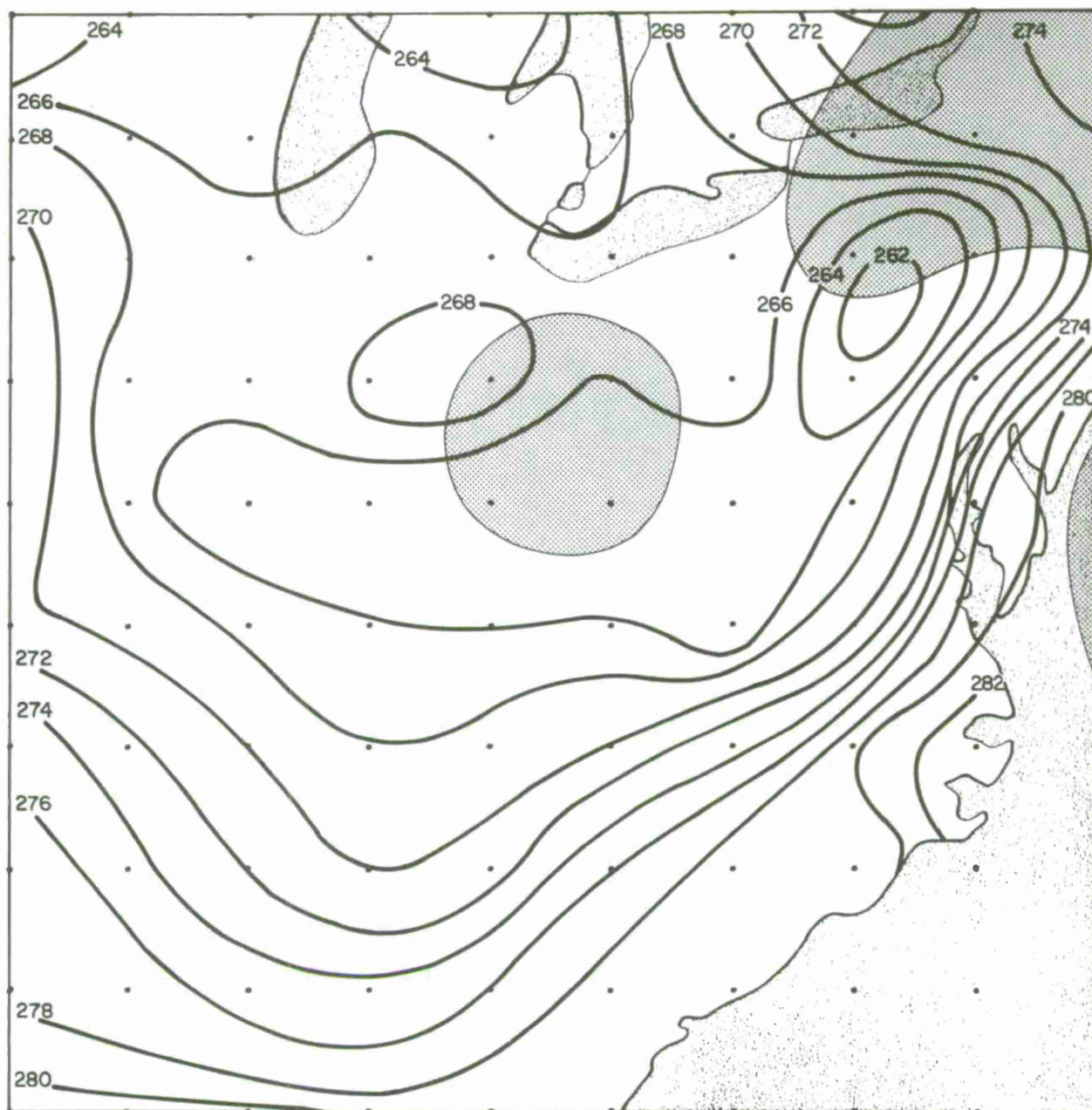



Fig. 15(e). Case C: analysis of observed temperature (°K) and humidity at verification time for level 2000 m above terrain height. $80\% \leq RH < 100\%$ 

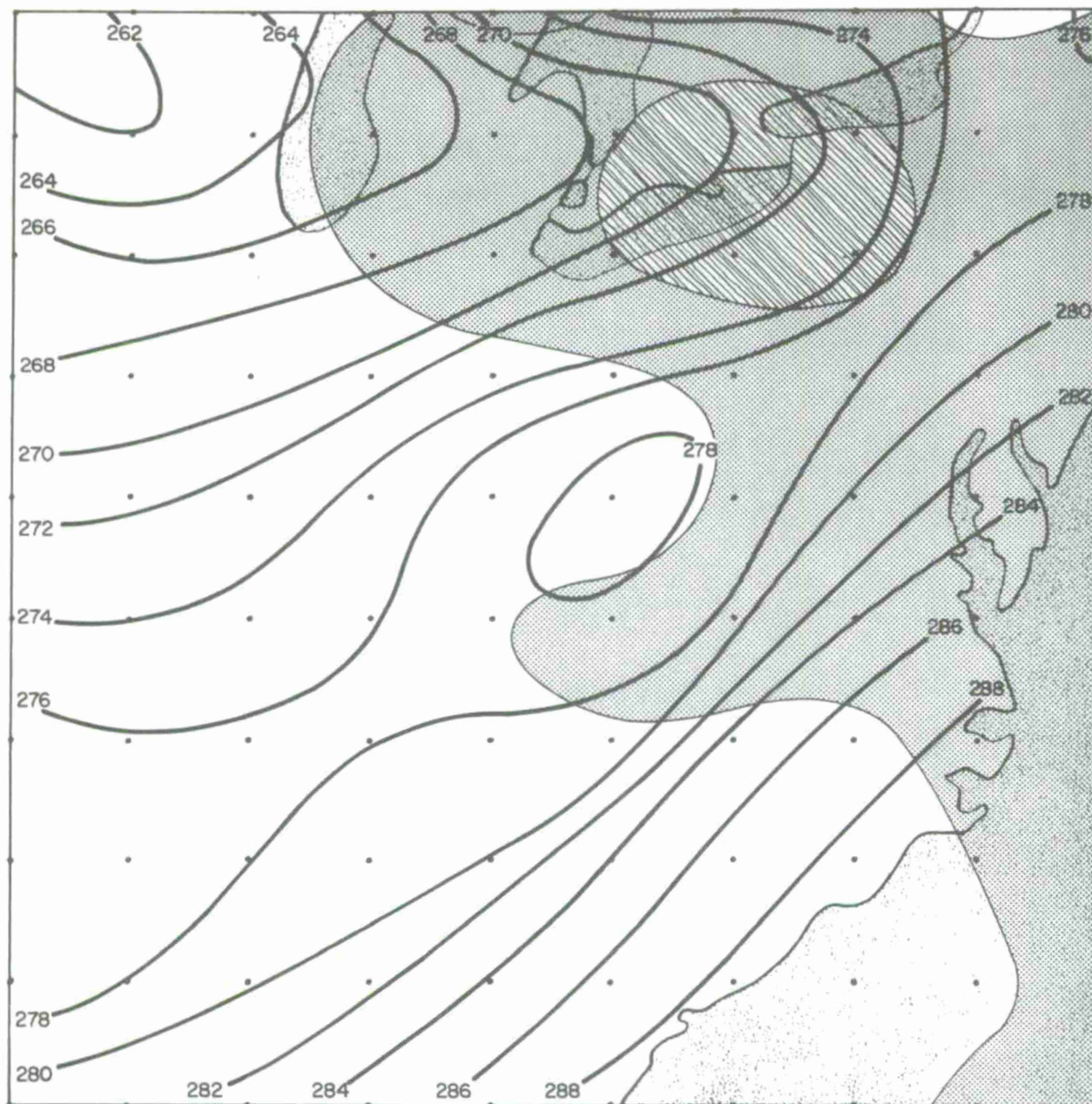




Fig. 15(f). Case C: analysis of predicted temperature ($^{\circ}\text{K}$) and humidity at verification time for level 500 m above terrain height. $80\% \leq RH < 100\%$  $RH \geq 100\%$ 

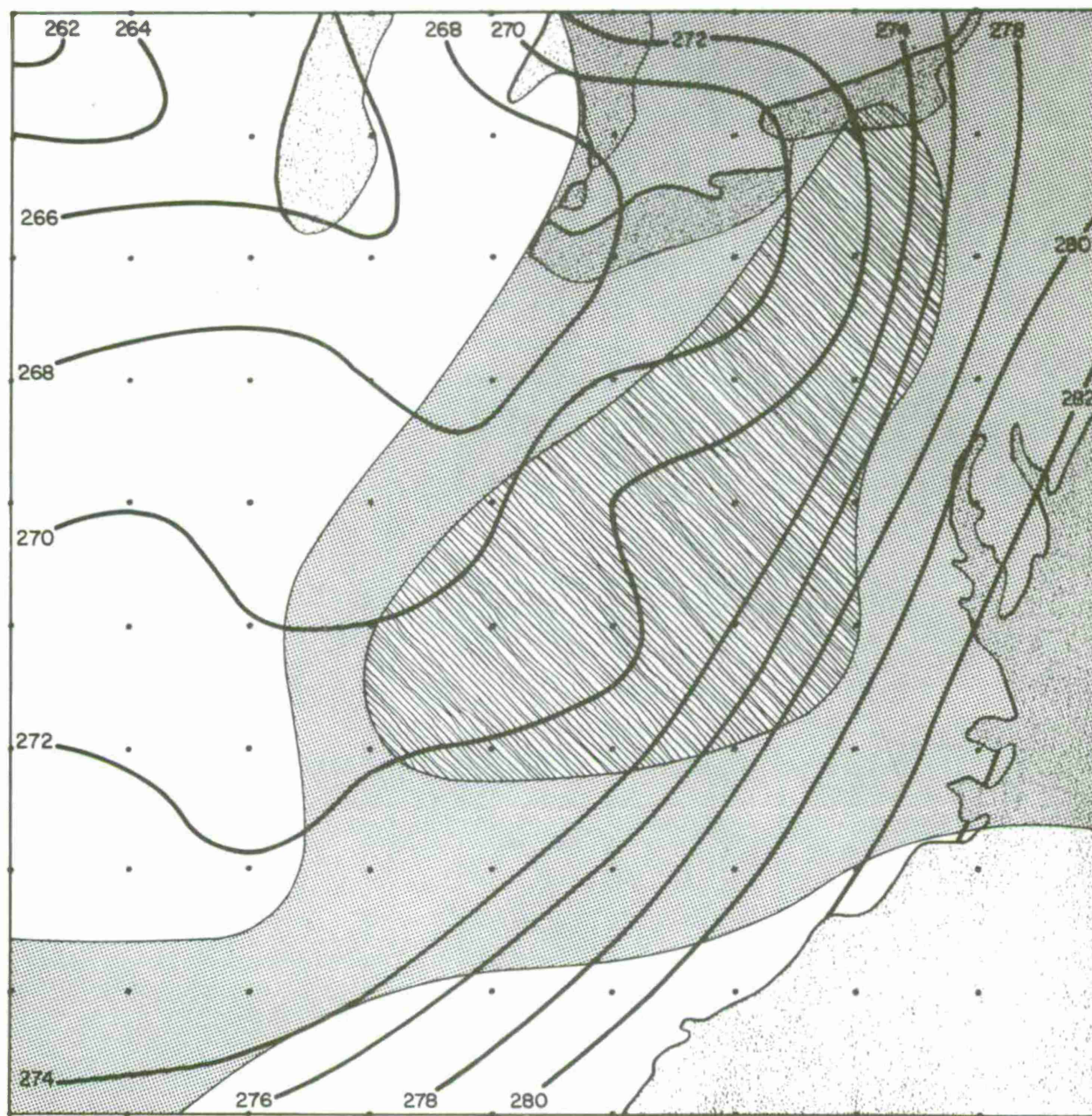






Fig. 15(g). Case C: analysis of predicted temperature ($^{\circ}\text{K}$) and humidity at verification time for level 1150 m above terrain height. $80\% \leq \text{RH} < 100\%$  $\text{RH} \geq 100\%$ 



Fig. 15(h). Case C: analysis of predicted temperature ($^{\circ}\text{K}$) and humidity at verification time for level 2000 m above terrain height. $80\% \leq \text{RH} < 100\%$ 
 $\text{RH} \geq 100\%$ 

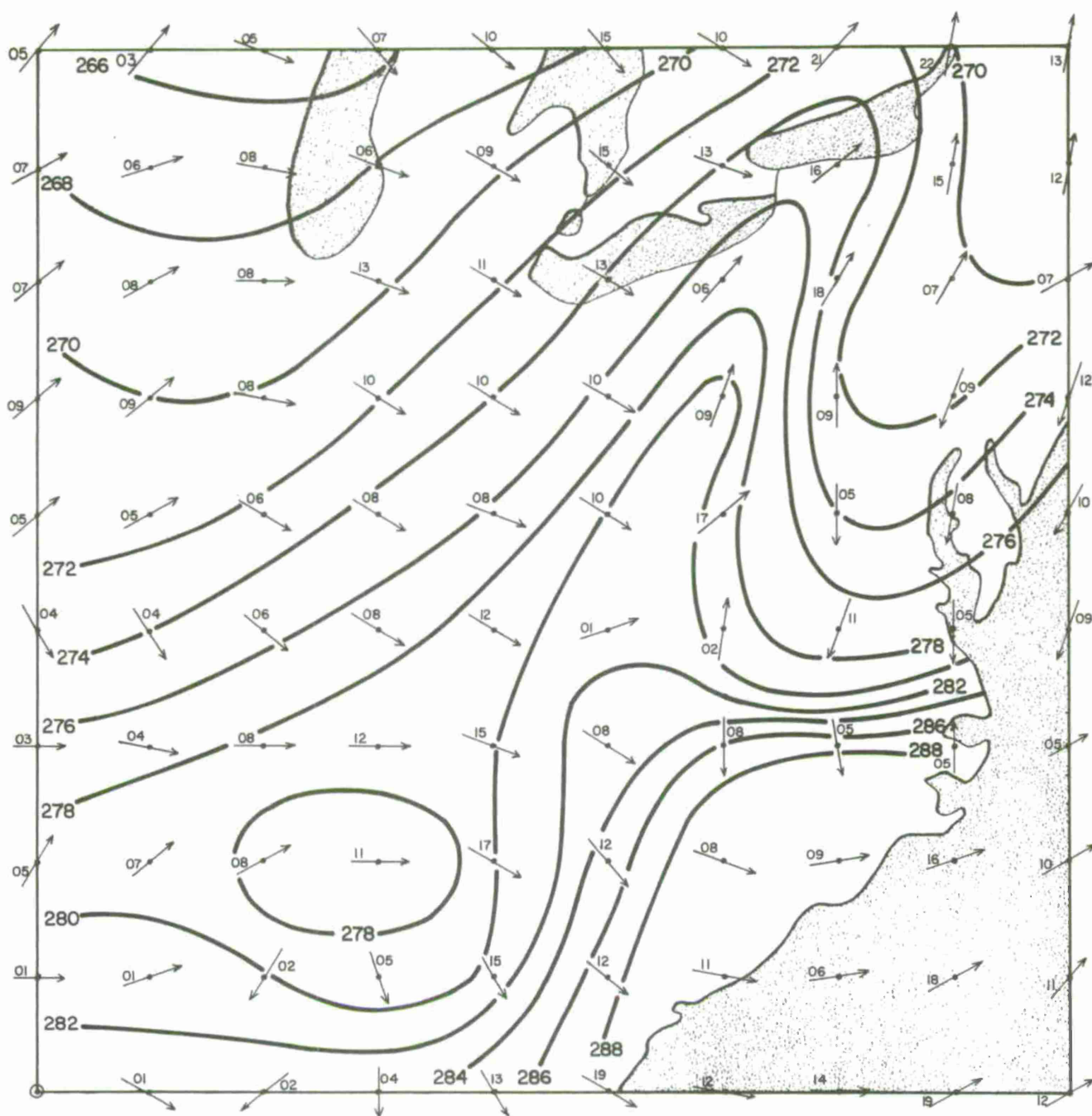


Fig. 15(i). Case C: analysis of observed surface isotherms ($^{\circ}\text{K}$) and derived 50-m wind field at verification time (arrows indicate wind direction; numbers indicate wind speed in m sec^{-1}).

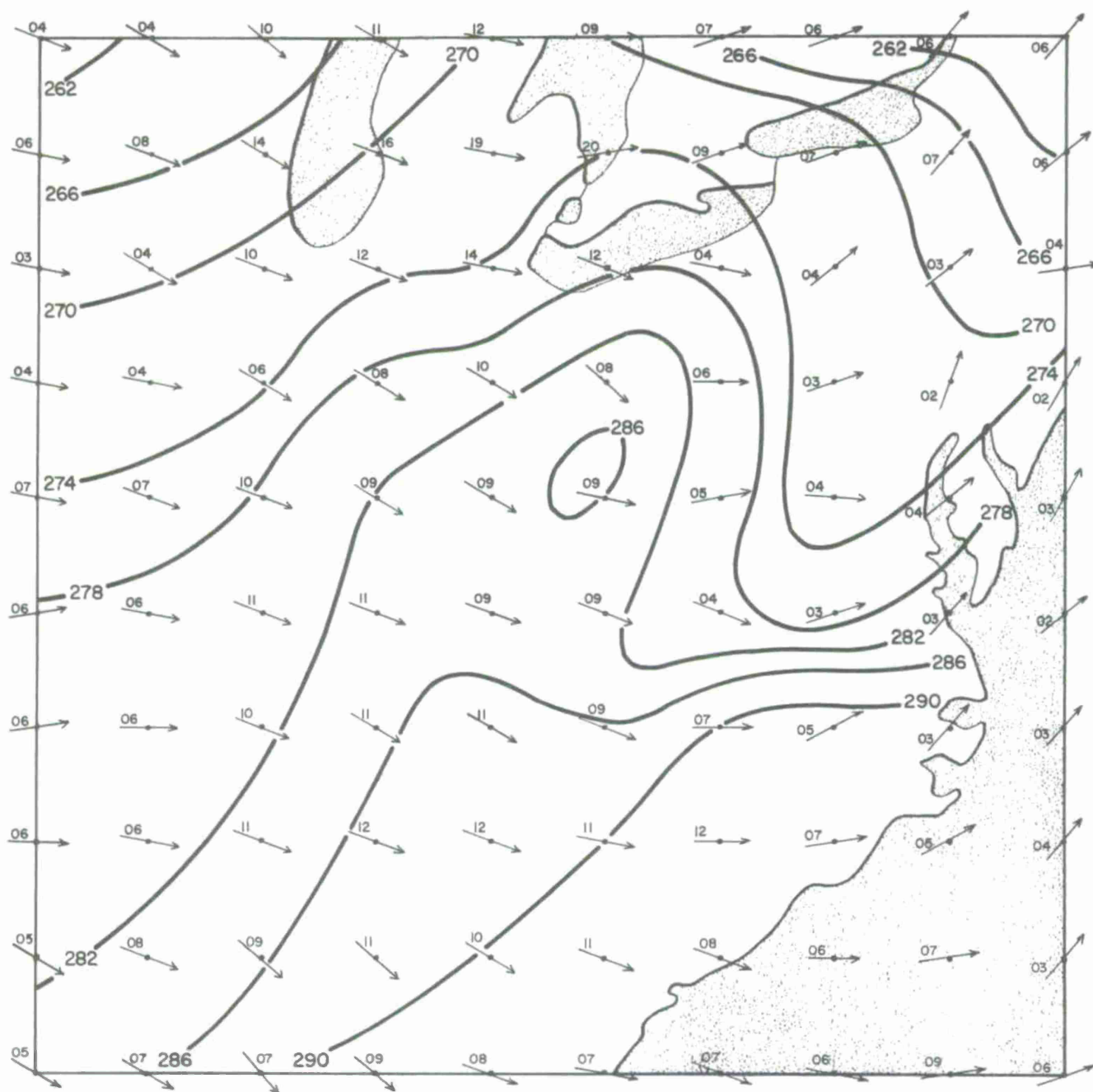


Fig. 15(j). Case C: prognosis of surface isotherms ($^{\circ}\text{K}$) and 50-m wind field valid at verification time (arrows indicate wind direction; numbers indicate wind speed in m sec^{-1}).

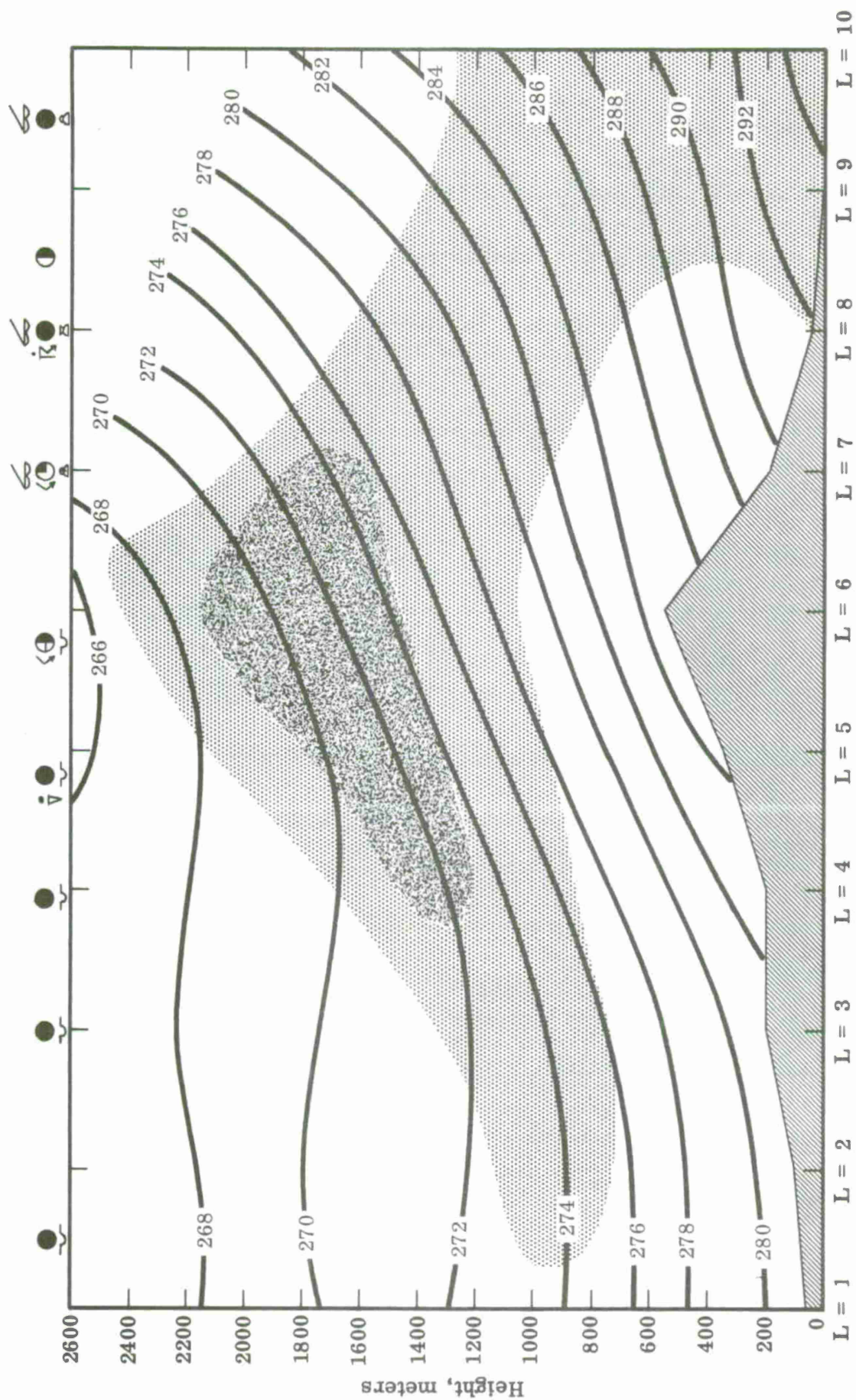


Fig. 15(k). Case C: vertical cross section along grid row M = 4 showing predicted temperature ($^{\circ}\text{K}$) and humidity, and observed sky condition and weather (at top of figure), valid at verification time. $\text{RH} < 100\%$  $\text{RH} \approx 100\%$ 

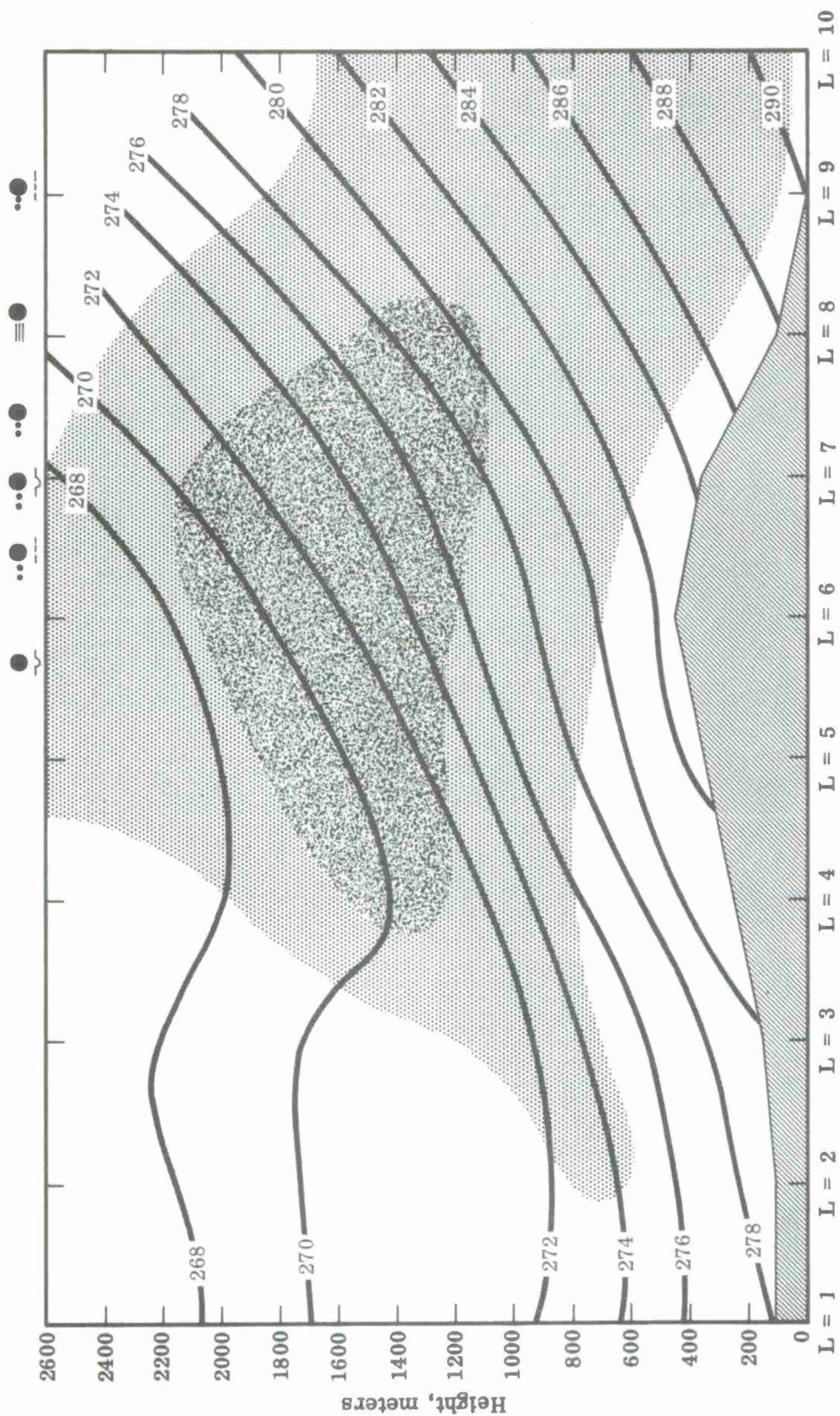


Fig. 15(1). Case C: vertical cross section along grid row M = 5 showing predicted temperature ($^{\circ}\text{K}$) and humidity, and observed sky condition and weather (at top of figure), valid at verification time. $\text{RH} < 100\%$ $\text{RH} \approx 100\%$

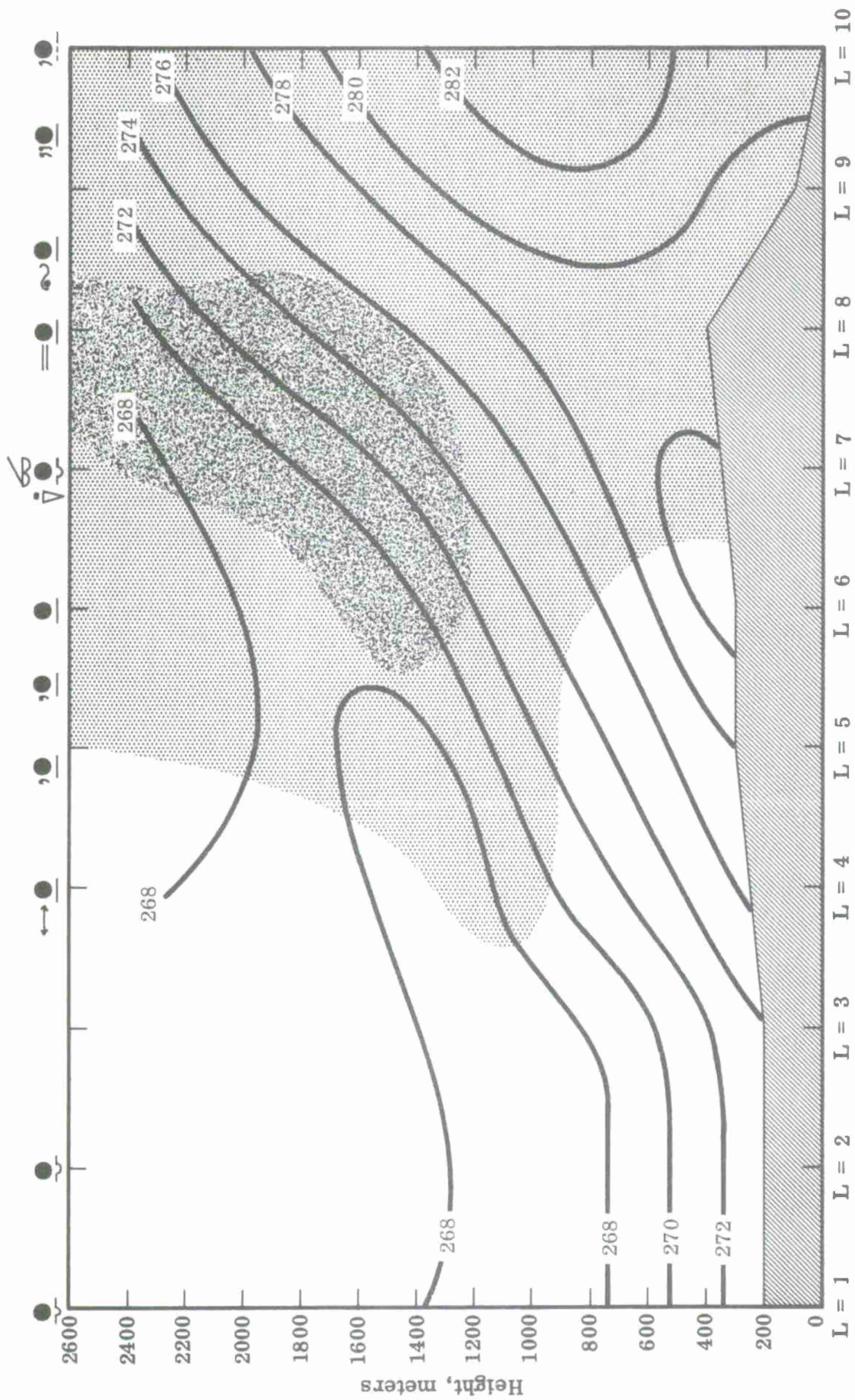




Fig. 15(n). Case C: vertical cross section along grid row $M = 7$ showing predicted temperature ($^{\circ}\text{K}$) and humidity, and observed sky condition and weather (at top of figure), valid at verification time. $RH < 100\%$  $RH \geq 100\%$ 

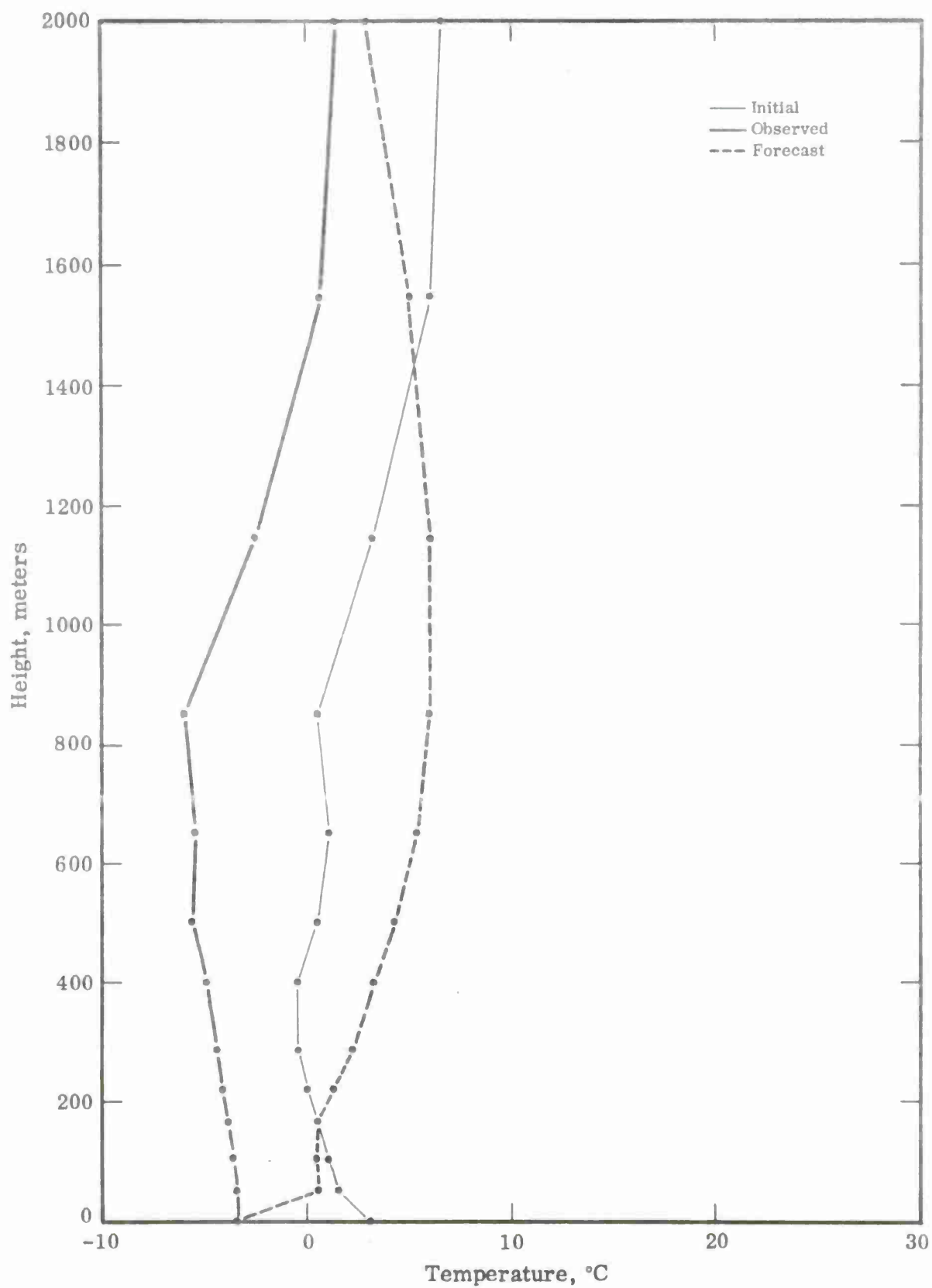


Fig. 16. Case C: observed initial-time and predicted temperature at grid-point $L = 10$, $M = 7$, and observed verification-time temperature at radiosonde station 518.

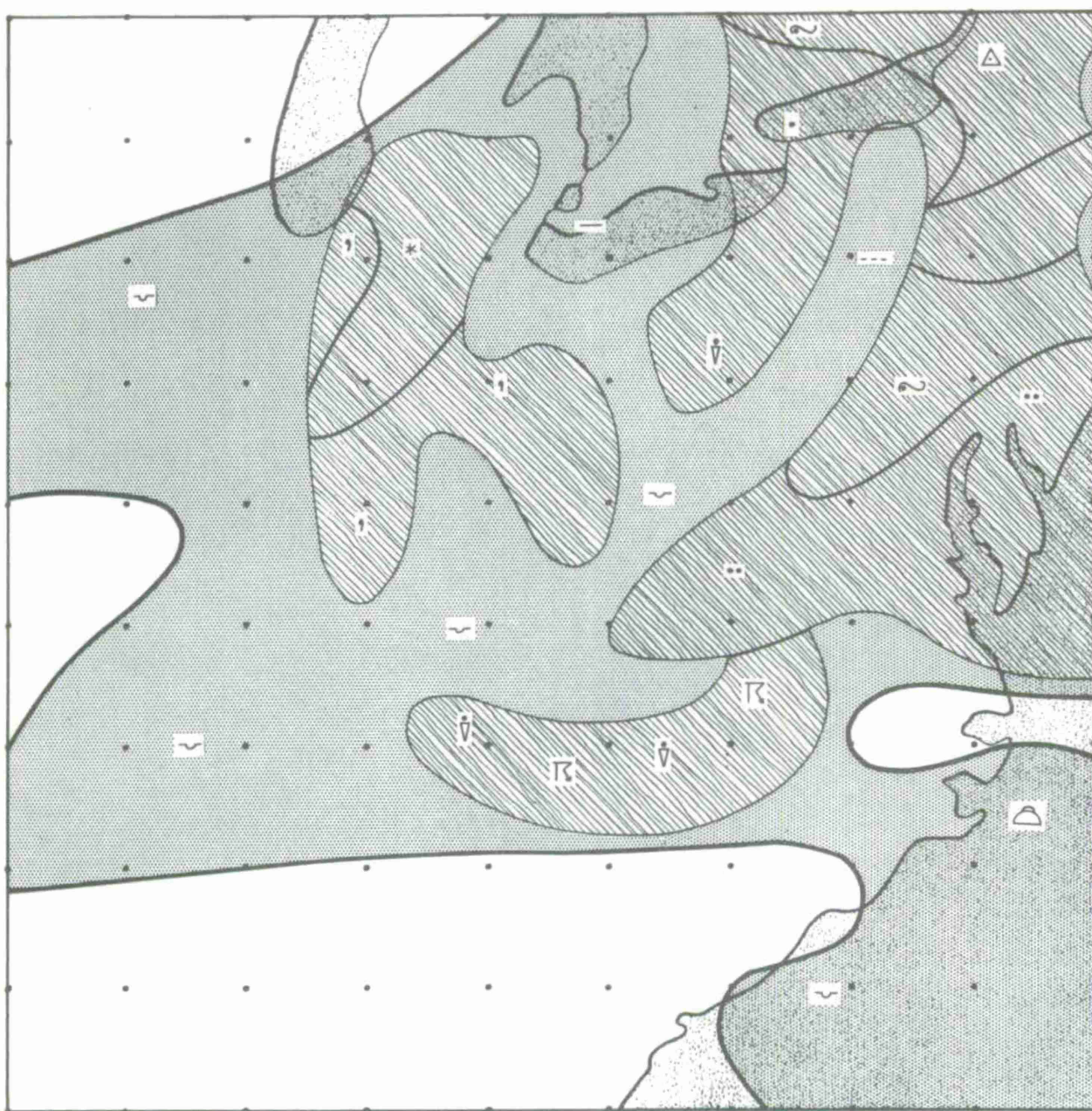




Fig. 17. Case C: regions reporting broken or overcast low cloudiness  and precipitation  at verification time. Type of precipitation is indicated.

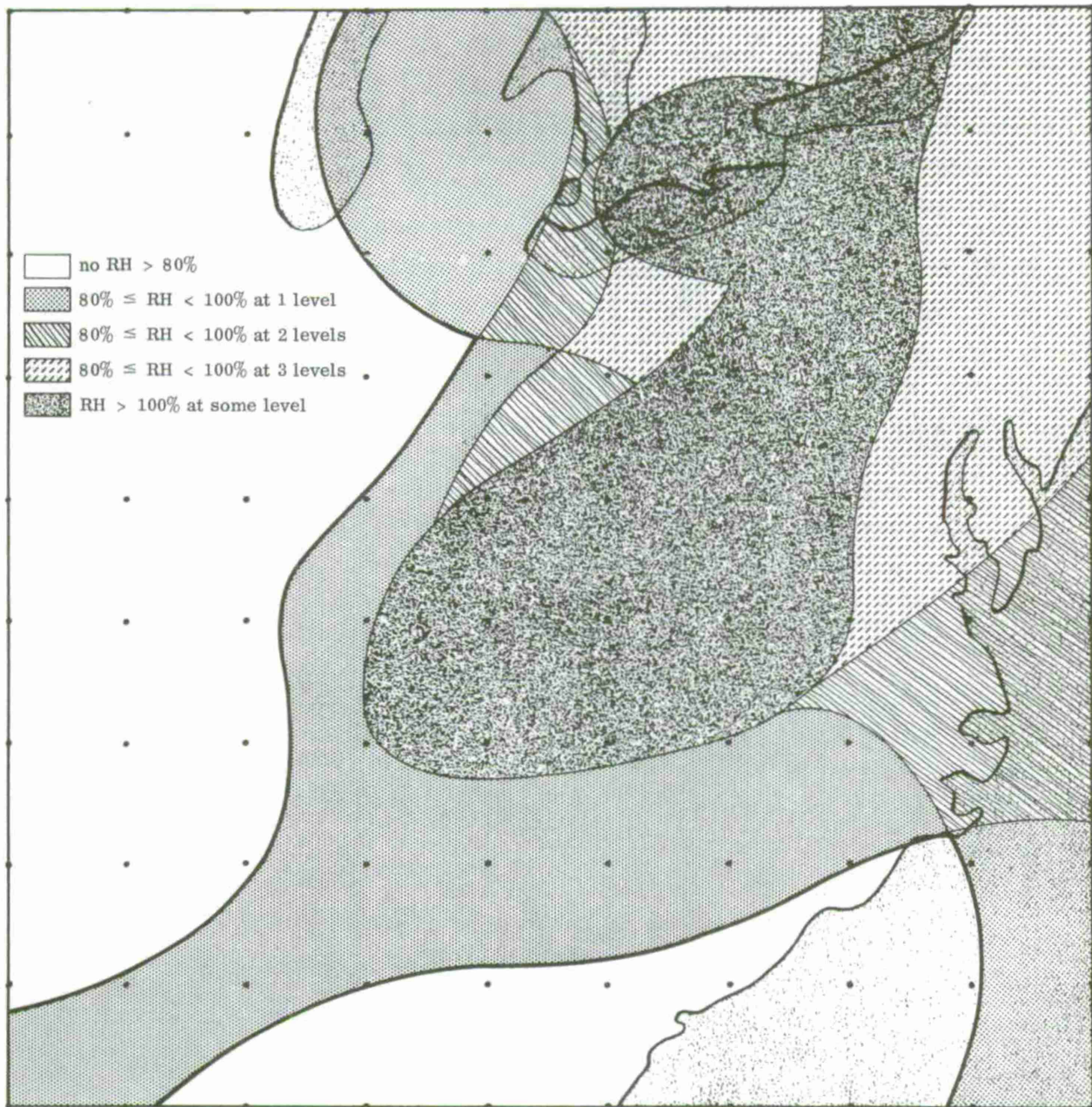


Fig. 18. Case C: composite of predicted humidity for the 500-, 1150-, and 2000-m levels.

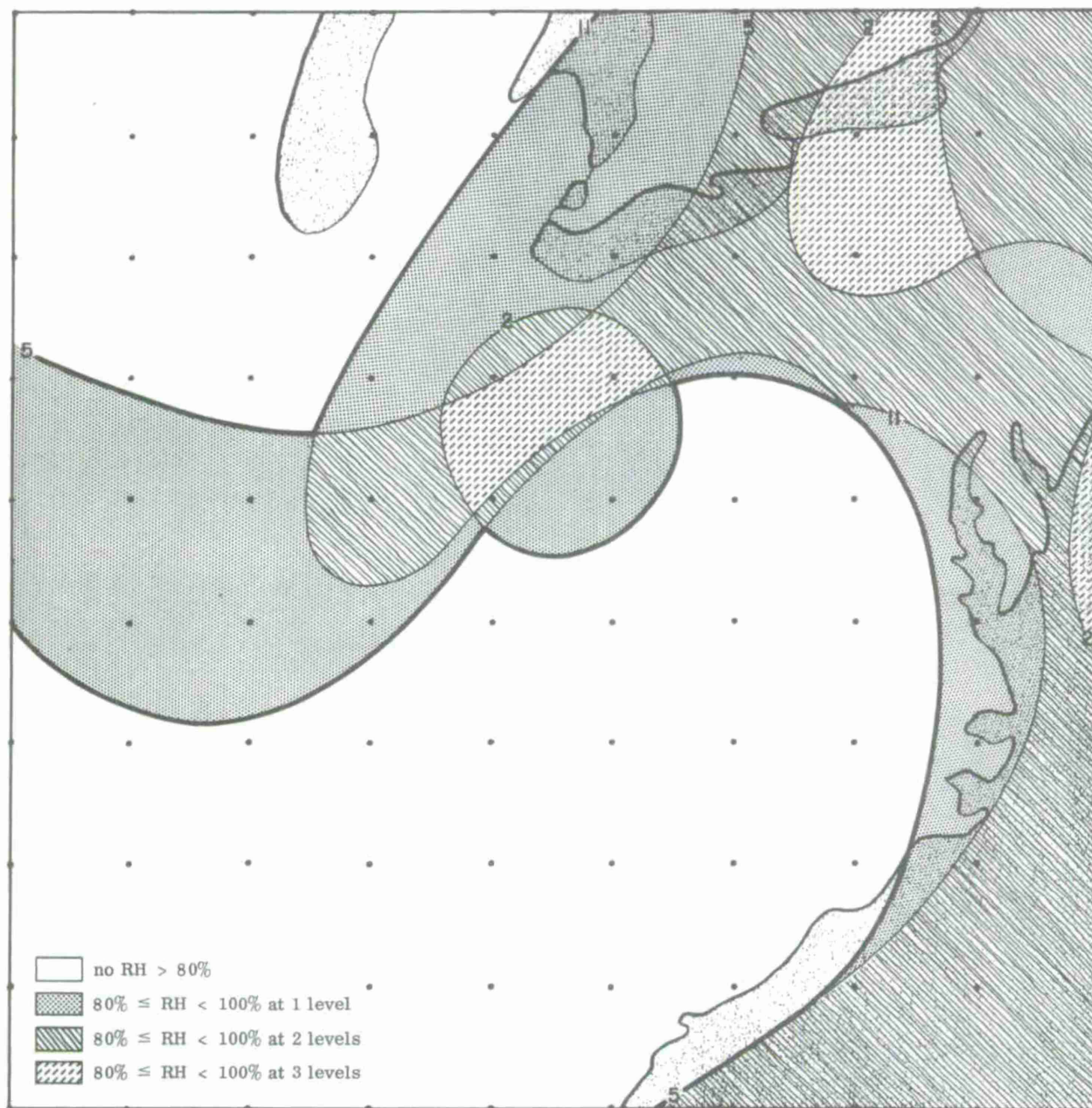


Fig. 19. Case C: composite of observed humidity for the 500-, 1150-, and 2000-m levels at verification time.

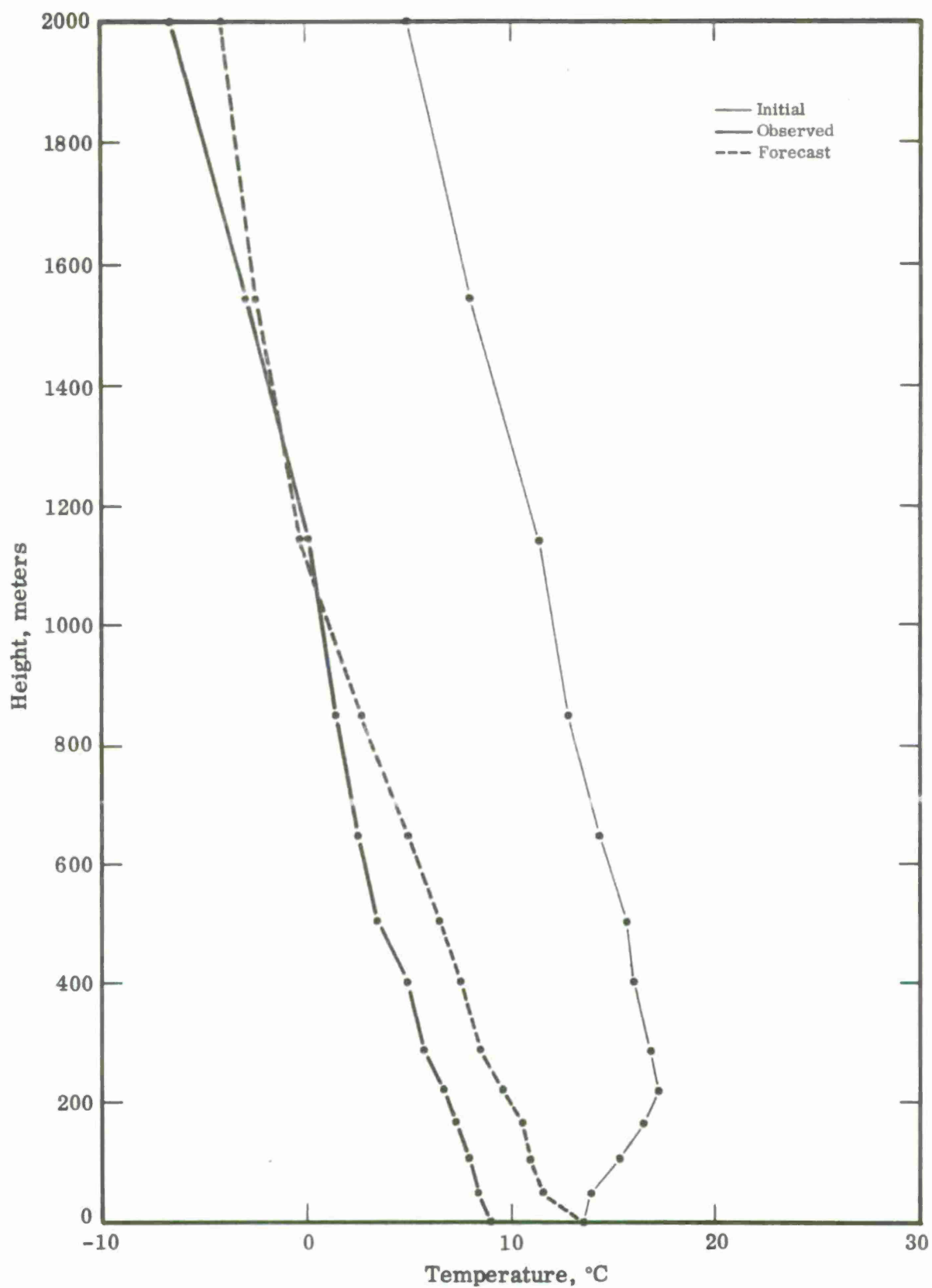


Fig. 20. Case C: initial and predicted temperature at grid point $L = 6$, $M = 6$, and observed verification-time temperature at radiosonde station 425.

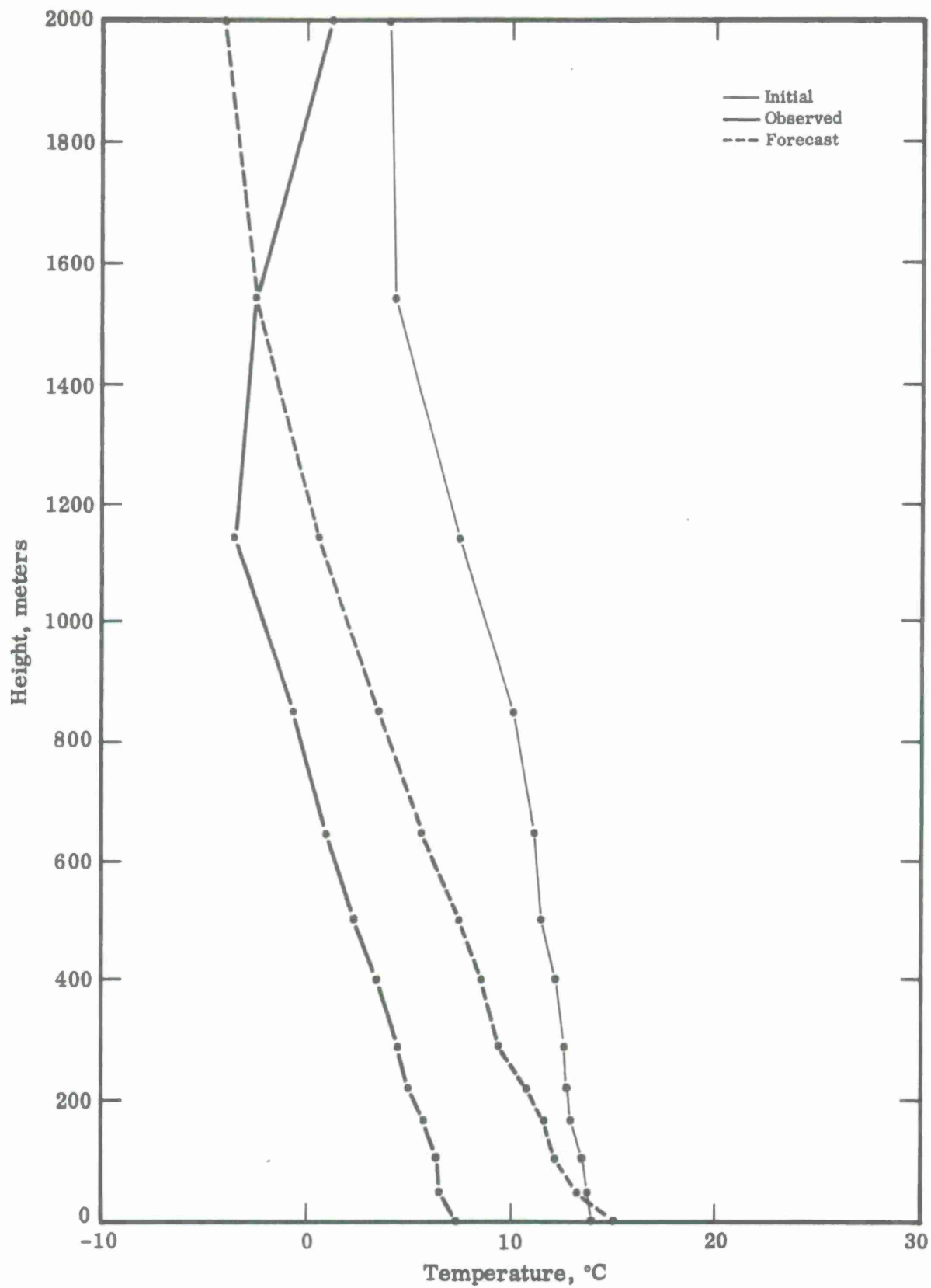


Fig. 21. Case C: initial and predicted temperature at grid point L = 5, M = 3, and observed verification-time temperature at radiosonde station 311.

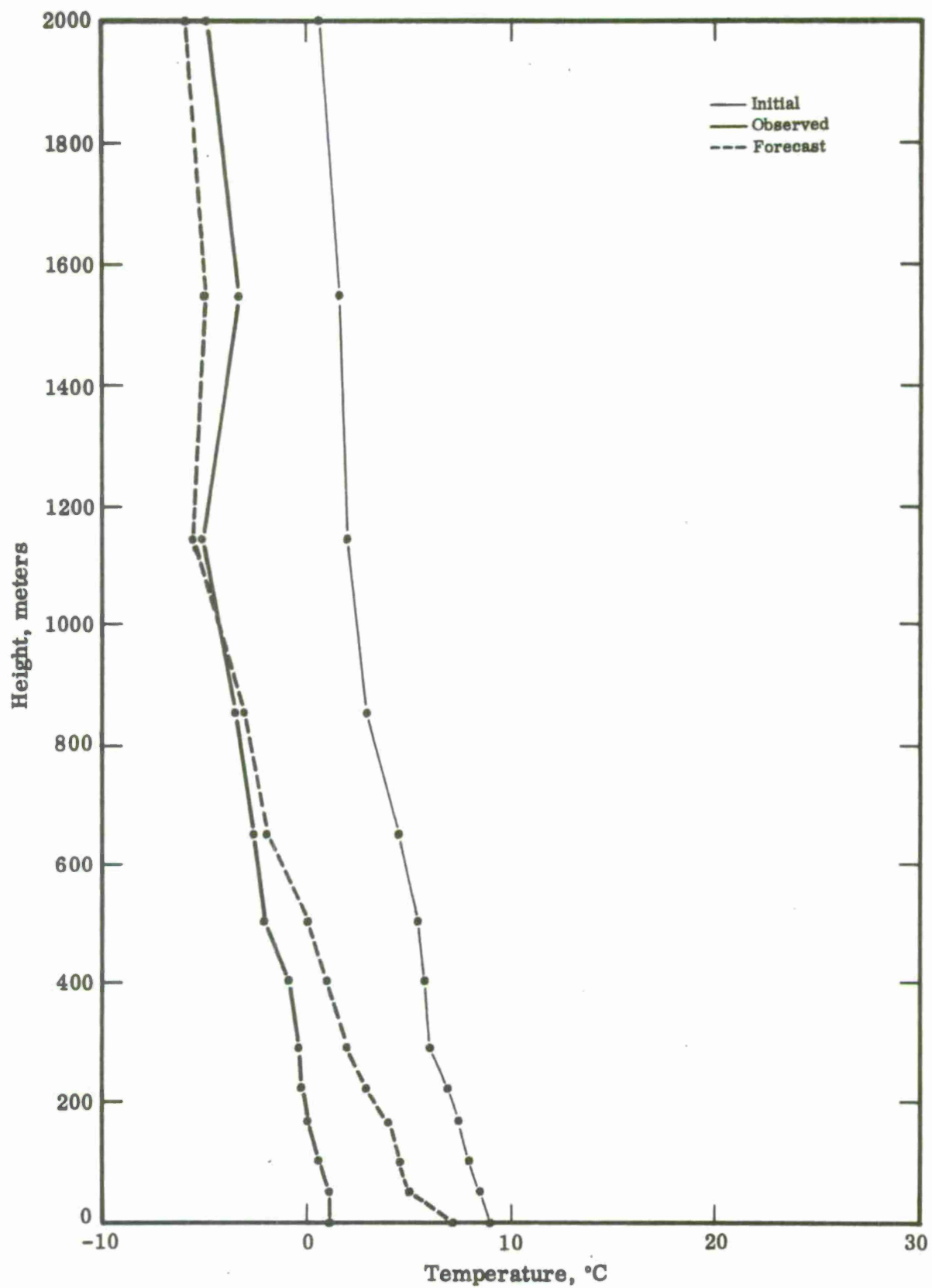


Fig. 22. Case C: initial and predicted temperature at grid point $L = 5$, $M = 7$, and observed verification-time temperature at radiosonde station 429.

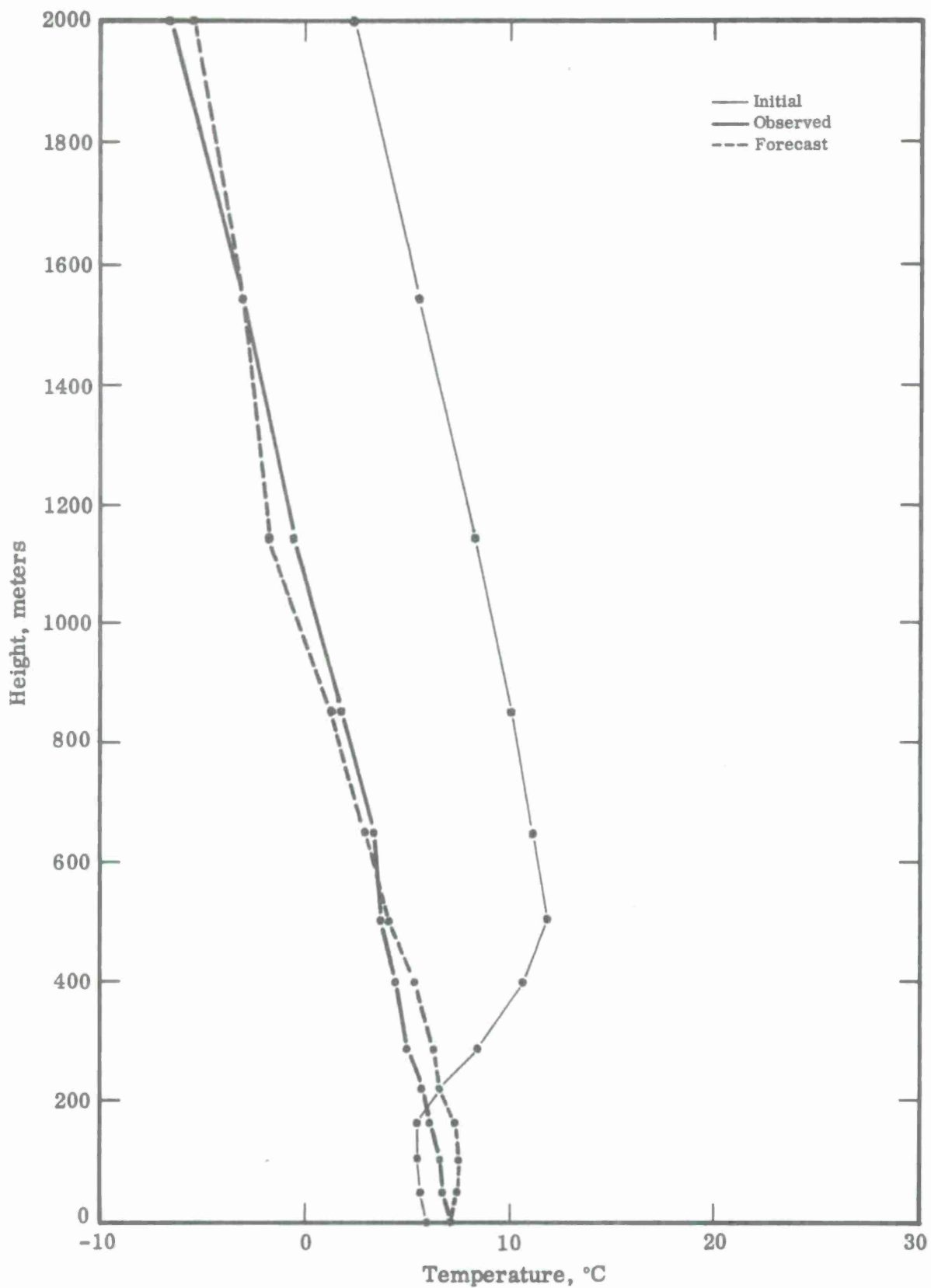


Fig. 23. Case C: initial and predicted temperature at grid point $L = 7$, $M = 7$, and observed verification-time temperature at radiosonde station 520.

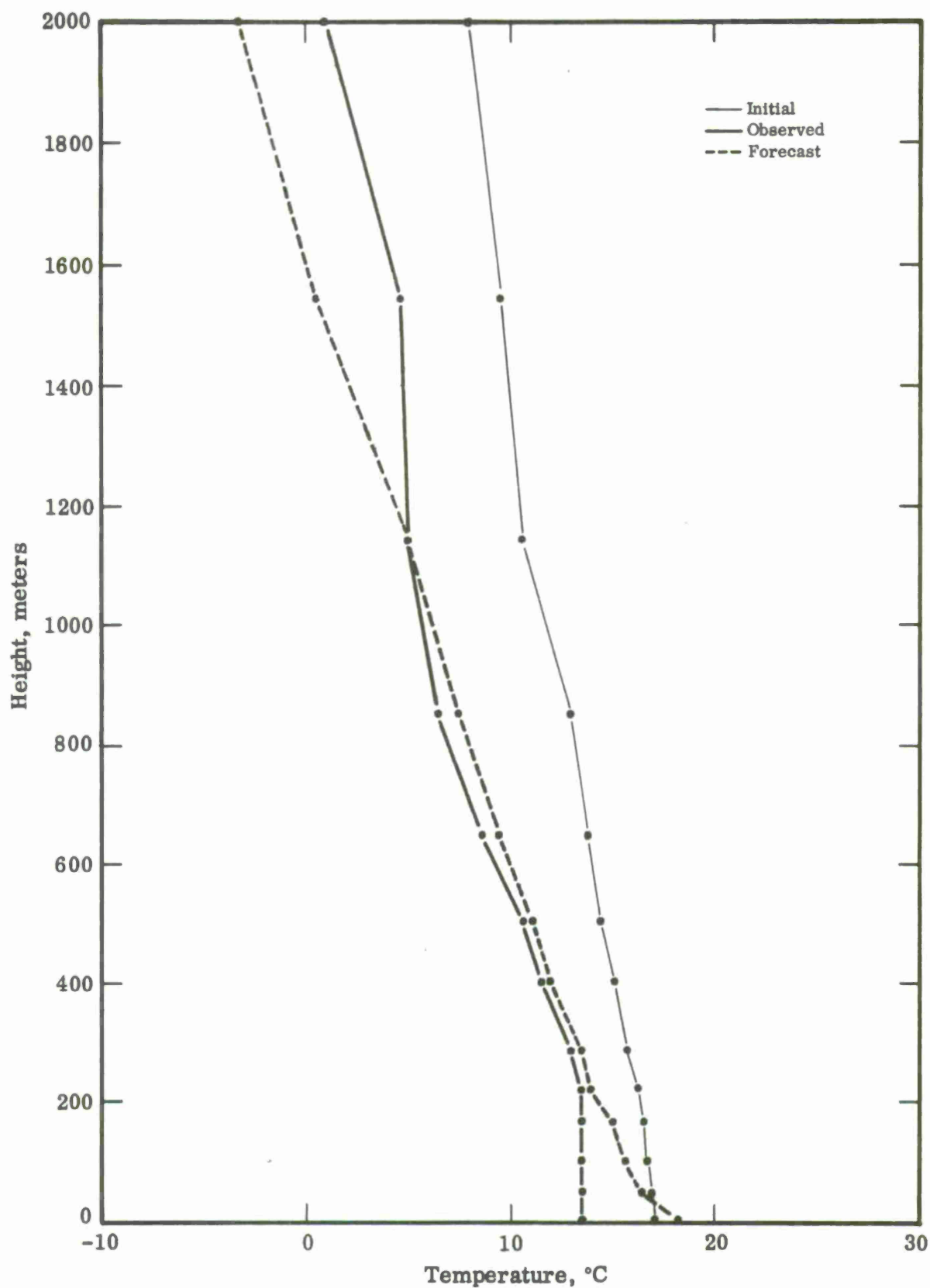


Fig. 24. Case C: initial and predicted temperature at grid point $L = 7$, $M = 4$, and observed verification-time temperature at radiosonde station 317.

SECTION V

CONCLUSIONS AND RECOMMENDATIONS

Based on the limited number of tests conducted, we may tentatively conclude that the model is capable of producing realistic and fairly accurate predictions of the structure of the atmospheric boundary layer. Our recommendations for further research using this or similar models are:

(a) Attempt to improve the strong-inversion formulation for the contact layer equations, especially in situations with warm advection.

(b) Formulate a procedure for incorporating the computation of the evaporation of large-scale precipitation within the boundary layer, and for the computation of precipitation from super-saturated portions of the boundary layer.

(c) Investigate the possibility of computing infrared radiative flux divergence for cloudy situations within the boundary layer.

(d) Examine the potential for developing improved diagnostic formulas for the horizontal wind, including the dependence of the eddy viscosity on the stability of the air.

(e) Develop objective analysis techniques for combining surface and radiosonde observations into grid-point data within the boundary layer.

It is, of course, desirable that a continuous effort be made to interpret the results of fundamental theoretical and empirical investigations of the structure of the boundary layer in the light of the requirements for synoptic-scale weather forecasts.

APPENDIX
LOGICAL AND COMPUTATIONAL
FORMULATION OF
THE NUMERICAL MODEL

APPENDIX

LOGICAL AND COMPUTATIONAL FORMULATION OF THE NUMERICAL MODEL

The equations of the boundary layer model were converted to a form suitable for solution on a digital computer. A set of specifications for a computer program was prepared to guide the programmer in writing the code. The actual program is available at the United Aircraft Research Laboratory, East Hartford, Connecticut or through request to the 433L Systems Program Office, Electronics Systems Division, Air Force Systems Command, L. G. Hanscom Field, Bedford, Mass. Including extensive output at hourly intervals, the time required for a 12-hr forecast on a 7094 computer was 27 minutes.

In this Appendix, we present the logical and computational basis for the numerical model.

Data

Input data will be provided in tabulated form. The format for the machine input is left to the discretion of the programmer.

In the table below, we indicate the symbol, name, system of units, approximate significances and magnitude, and storage requirements for the several variables used in the computation. Those quantities to be provided as input are marked with an asterisk.

TABLE VI
DEFINITIONS

Symbol	Definition	Units	Magnitude and significance	Storage
T	Air temperature*	°C	XXX.X	10·10·12·2
q	Specific humidity*	none	XX.X· Ex	10·10·12·2
r	Specific moisture*	none	XX.X· Ex	10·10·12·2
UGH1	x-component of geostrophic wind at Z=H at initial time*	cm sec ⁻¹	XX.X· Ex	10·10
UGH2	x-component of geostrophic wind at Z=H at +6 hrs*	cm sec ⁻¹	XX.X· Ex	10·10
UGH3	x-component of geostrophic wind at Z=H at +12 hrs*	cm sec ⁻¹	XX.X· Ex	10·10
VGH1	y-component of geostrophic wind at Z=H at an initial time*	cm sec ⁻¹	XX.X· Ex	10·10
VGH2	y-component of geostrophic wind at +6 hrs*	cm sec ⁻¹	XX.X· Ex	10·10
VGH3	y-component of geostrophic wind at Z=H at +12 hrs*	cm sec ⁻¹	XX.X· Ex	10·10
ICLU1	Upper cloud index 0—+6 hr*	none	X	10·10
ICLU2	Upper cloud index +6—+12 hr*	none	X	10·10
WET	Ground moisture factor*	none	X.XX	10·10
E	Height of terrain*	cm	XXX.X· Ex	10·10
Z ₀	Surface roughness factor*	cm	XX.X· Ex	10·10
XM	Map scale factor*	none	X.XXXXX	10·10
TS	Surface temperature*	°A	XXX.X	10·10
RHS	Surface relative humidity*	none	X.XX	10·10
f	Coriolis parameter*	sec ⁻¹	X.XXX· Ex	10·10
ρ	Mean value air density*	gm cm ⁻³	X.XXX· Ex	1
(DZ) _k	Vertical grid spacing*	cm	XXX.XX· Ex	13
C1	Sine of solar declination	none	X.XXXXXXX	1
C2	Cosine of solar declination*	none	X.XXXXXXX	1
C3	Tangent of solar declination*	none	X.XXXXXXX	1
D	Standard horizontal grid interval*	cm	XXX.XX· Ex	1
DT	Time step interval*	sec	XXXX.X	1
TIME 0	Initial time (EST)*	sec	XXXXX.X	1
g	Gravity acceleration*	cm sec ⁻²	XXX.X	1
C _p	Specific heat*	ergs gm ⁻¹ deg ⁻¹	X.XXXXXXX·Ex	1
γ	Ratio of g to C _p *	deg cm ⁻¹	X.XXX·Ex	1
Θ	Mean air temperature*	°A	XXX.X	1
β	Forced convection parameter*	none	XX.X	
λ	Free convection parameter*	none	X.XX	1
κ	Von Karman's constant*	none	X.XX	1
Z _i	Instrument shelter height*	cm	XXX.	10·10
SLAT	Latitude*	radians	X.XXXXXXX	10·10
SLNG	Longitude*	degrees	XXX.XX	10·10

*To be provided as input.

TABLE VI (Continued)

Symbol	Definition	Units	Magnitude and significance	Storage
RA	Radiation coefficient*	$^{\circ}\text{F hr}^{-1}$.XXXX · Ex	10·10·3
RB	Radiation coefficient*	$^{\circ}\text{F hr}^{-1}$.XXXX · Ex	10·10·3
RC	Radiation coefficient*	$^{\circ}\text{F hr}^{-1}$.XXXX · Ex	10·10·3
RD	Radiation coefficient*	$^{\circ}\text{F hr}^{-1}$.XXXX · Ex	10·10·3
K	Mixing coefficient	$\text{cm}^2 \text{sec}^{-1}$		10·10·12
\hat{K}	SFC mixing coefficient	$\text{cm}^2 \text{sec}^{-1}$		10·10
w	Frictional vertical velocity	cm sec^{-1}		10·10·13
\hat{w}	Terrain vertical velocity	cm sec^{-1}		10·10·13
u	x-component horizontal wind	cm sec^{-1}		10·10·13
v	y-component horizontal wind	cm sec^{-1}		10·10·13
I	Convection index	none		10·10
RATIO	Wind speed ratio	none		10·10
VF	Vapor flux ($U_* Q_*$)	cm sec^{-1}		10·10
HF	Heat flux ($U_* \Theta_*$)	deg cm sec^{-1}		10·10
u_*	Friction velocity	cm sec^{-1}		10·10
ϕ	Geostrophic deviation angle	none		10·10
\hat{q}	SFC specific humidity	none		10·10
Z_k	Height of k^{th} level	cm		13
a	Gaussian elimination coefficients	none		13
b	Gaussian elimination coefficients	none		13
c	Gaussian elimination coefficients	none		13
TIME 0	Initial time	sec		1
TIME	Time	sec		1
TIMER	Radiation time	hr		1
S	Wind speed at $Z = h$	cm sec^{-1}		10·10
U	x-component wind at $Z = h$	cm sec^{-1}		10·10
V	y-component wind at $Z = h$	cm sec^{-1}		10·10
U_g^H	x-component geostrophic wind at $Z = H$	cm sec^{-1}		10·10
V_g^H	y-component geostrophic wind at $Z = H$	cm sec^{-1}		10·10
U_g	x-component geostrophic wind	cm sec^{-1}		Share with
V_g	y-component geostrophic wind	cm sec^{-1}		U and V
A	Dummy field			10·10
B	Dummy field			10·10
C	Dummy field			10·10
R	Dummy field			10·10
AA	Dummy field			10·10·13
DUMYA	Dummy field			10·10
DUMYB	Dummy field			10·10

*To be provided as input.

Computations

Coordinate System and Finite Difference Notation

The independent variables are the three space dimensions (x, y, z) and time (t). The x, y coordinates are the horizontal coordinates (approximately parallel to the earth's surface). The z coordinate is directed normal to the earth's surface and counted positive toward the zenith.

We define a finite set of points in space as the finite-difference grid. The points forming this grid will have the coordinates, X_ℓ , Y_m , Z_k , with $\ell = 1, 2, \dots, L$; $m = 1, 2, \dots, M$; $k = 1, 2, \dots, K$. Thus, there will be $L M K$ grid points covering the space within which our equations are to be solved. We will compute the solution only at discrete times, t_n ; $n = 1, 2, \dots, N$.

The intervals between grid points are defined as follows:

$$\begin{aligned}(DX)_\ell &= X_\ell - X_{\ell-1} & \ell &= 2, \dots, L \\(DY)_m &= Y_m - Y_{m-1} & m &= 2, \dots, M \\(DZ)_k &= Z_k - Z_{k-1} & k &= 2, \dots, K \\(DT)_n &= t_n - t_{n-1} & n &= 2, \dots, N\end{aligned}$$

In this work, we will take,

$$\begin{aligned}D &= (DX)_\ell = (DY)_m \text{ (constant)} \\DT &= (DT)_n \text{ (constant)}\end{aligned}$$

If a dependent variable is defined [e.g., $F = F(x, y, z, t)$], we will use the following notation:

$$F_{\ell, m}^{k, n} = F(x = x_\ell, y = y_m, Z = Z_k, t = t_n).$$

If the variable depends upon fewer than four independent variables, only the indices required will be used [e.g., $F_{\ell, m}^n = F(x = x_\ell, y = y_m, t = t_n)$].

Definition of an Advection Operator

In setting up the difference form of the differential equations, we must treat advection terms of the form

$$u \frac{\partial T}{\partial X} \quad \text{and} \quad v \frac{\partial T}{\partial Y}$$

The method of upwind differencing will be applied to these terms (see [9]). We will use the symbols $[X(T)]_{\ell, m}^k$ and $[Y(T)]_{\ell, m}^k$ to represent these terms. The symbols are defined as follows:

For $\ell = 1$ and $m = 1$:

If $u_{1,1}^k > 0$, or $v_{1,1}^k > 0$, set

$$[X(T)]_{1,1}^k = [Y(T)]_{1,1}^{k,n} = 0$$

Otherwise, set

$$[X(T)]_{1,1}^k = u_{1,1}^k * \frac{XM_{1,1}}{D} * [T_{2,1}^{k,n} - T_{1,1}^{k,n}]$$

$$[Y(T)]_{1,1}^k = v_{1,1}^k * \frac{XM_{1,1}}{D} * [T_{1,2}^{k,n} - T_{1,1}^{k,n}]$$

For $\ell = L$ and $m = 1$:

If $u_{L,1}^k < 0$, or $v_{L,1}^k > 0$, set

$$[X(T)]_{L,1}^k = [Y(T)]_{L,1}^k = 0$$

Otherwise, set

$$[X(T)]_{L,1}^k = u_{L,1}^k * \frac{XM_{L,1}}{D} * [T_{L,1}^{k,n} - T_{L-1,1}^{k,n}]$$

$$[Y(T)]_{L,1}^k = v_{L,1}^k * \frac{XM_{L,1}}{D} * [T_{L,2}^{k,n} - T_{L,1}^{k,n}]$$

For $\ell = 1$ and $m = M$:

If $u_{1,M}^k > 0$, or $v_{1,M}^k < 0$, set

$$[X(T)]_{1,M}^k = [Y(T)]_{1,M}^k = 0.$$

Otherwise, set

$$[X(T)]_{1,M}^k = u_{1,M}^k * \frac{XM_{1,M}}{D} * [T_{2,M}^{k,n} - T_{1,M}^{k,n}]$$

$$[Y(T)]_{1,M}^k = v_{1,M}^k * \frac{XM_{1,M}}{D} * [T_{1,M}^{k,n} - T_{1,M-1}^{k,n}]$$

For $\ell = L$ and $m = M$:

If $u_{L,M}^k < 0$, or $v_{L,M}^k < 0$, set

$$[X(T)]_{L,M}^k = [Y(T)]_{L,M}^k = 0.$$

Otherwise, set

$$[X(T)]_{L,M}^k = u_{L,M}^k * \frac{XM_{L,M}}{D} * [T_{L,M}^{k,n} - T_{L-1,M}^{k,n}]$$

$$[Y(T)]_{L,M}^k = v_{L,M}^k * \frac{XM_{L,M}}{D} * [T_{L,M}^{k,n} - T_{L,M-1}^{k,n}]$$

For $\ell = 2, \dots, L-1$ and $m = 2, \dots, M-1$:

If $u_{\ell,m}^k \geq 0$, set

$$[X(T)]_{\ell,m}^k = u_{\ell,m}^k * \frac{XM_{\ell,m}^{k,n}}{D} * [T_{\ell,m}^{k,n} - T_{\ell-1,m}^{k,n}];$$

If $u_{\ell,m}^k < 0$, set

$$[X(T)]_{\ell,m}^k = u_{\ell,m}^k * \frac{XM_{\ell,m}^{k,n}}{D} * [T_{\ell+1,m}^{k,n} - T_{\ell,m}^{k,n}];$$

If $v_{\ell,m}^k \geq 0$, set

$$[Y(T)]_{\ell,m}^k = v_{\ell,m}^k * \frac{XM_{\ell,m}^{k,n}}{D} * [T_{\ell,m}^{k,n} - T_{\ell,m-1}^{k,n}];$$

If $v_{\ell,m}^k < 0$, set

$$[Y(T)]_{\ell,m}^k = v_{\ell,m}^k * \frac{XM_{\ell,m}^{k,n}}{D} * [T_{\ell,m+1}^{k,n} - T_{\ell,m}^{k,n}].$$

For $\ell = 1$; $m = 2, \dots, M-1$;

If $u_{1,m} > 0$, set

$$[X(T)]_{1,m}^k = [Y(T)]_{1,m}^k = 0.$$

Otherwise, set

$$[X(T)]_{1,m}^k = u_{1,m}^k * \frac{XM_{1,m}}{D} * [T_{2,m}^{k,n} - T_{1,m}^{k,n}],$$

and, if $v_{1,m}^k \geq 0$, set

$$[Y(T)]_{1,m}^k = v_{1,m}^k * \frac{XM_{1,m}}{D} * [T_{1,m}^{k,n} - T_{1,m-1}^{k,n}],$$

If $v_{1,m}^k < 0$, set

$$[Y(T)]_{1,m}^k = v_{1,m}^k * \frac{XM_{1,m}}{D} * [T_{1,m+1}^{k,n} - T_{1,m}^{k,n}].$$

For $\ell = L$; $m = 2, \dots, M - 1$:

If $u_{L,m} < 0$, set

$$[X(T)]_{L,m}^k = [Y(T)]_{L,m}^k = 0.$$

Otherwise, set

$$[X(T)]_{L,m}^k = u_{L,m}^k * \frac{XM_{L,m}}{D} * [T_{L,m}^{k,n} - T_{L-1,m}^{k,n}],$$

and, if $v_{L,m}^k \geq 0$, set

$$[Y(T)]_{L,m}^k = v_{L,m}^k * \frac{XM_{L,m}}{D} * [T_{L,m}^{k,n} - T_{L,m-1}^{k,n}],$$

If $v_{L,m}^k < 0$, set

$$[Y(T)]_{L,m}^k = v_{L,m}^k * \frac{XM_{L,m}}{D} * [T_{L,m+1}^{k,n} - T_{L,m}^{k,n}].$$

For $m = 1$, $\ell = 2, \dots, L - 1$:

If $v_{\ell,1}^k > 0$, set

$$[X(T)]_{\ell,1}^k = [Y(T)]_{\ell,1}^k = 0.$$

Otherwise, set

$$[Y(T)]_{\ell,1}^k = v_{\ell,1}^k * \frac{XM_{\ell,1}}{D} * [T_{\ell,2}^{k,n} - T_{\ell,1}^{k,n}],$$

and, if $u_{\ell, 1}^k \geq 0$, set

$$[X(T)]_{\ell, 1}^k = u_{\ell, 1}^k * \frac{XM_{\ell, 1}}{D} * [T_{\ell, 1}^{k, n} - T_{\ell-1, 1}^{k, n}],$$

If $u_{\ell, 1}^k < 0$, set

$$[X(T)]_{\ell, 1}^k = u_{\ell, 1}^k * \frac{XM_{\ell, 1}}{D} * [T_{\ell+1, 1}^{k, n} - T_{\ell, 1}^{k, n}].$$

For $m = M$; $\ell = 2, \dots, L - 1$;

If $v_{\ell, M}^k < 0$, set

$$[X(T)]_{\ell, M}^k = [Y(T)]_{\ell, M}^k = 0.$$

Otherwise, set

$$[Y(T)]_{\ell, M}^k = v_{\ell, M}^k * \frac{XM_{\ell, M}}{D} * [T_{\ell, M}^{k, n} - T_{\ell, M-1}^{k, n}],$$

and, if $u_{\ell, M}^k \geq 0$, set

$$[X(T)]_{\ell, M}^k = u_{\ell, M}^k * \frac{XM_{\ell, M}}{D} * [T_{\ell, M}^{k, n} - T_{\ell-1, M}^{k, n}],$$

If $u_{\ell, M}^k < 0$, set

$$[X(T)]_{\ell, M}^k = u_{\ell, M}^k * \frac{XM_{\ell, M}}{D} * [T_{\ell+1, M}^{k, n} - T_{\ell, M}^{k, n}].$$

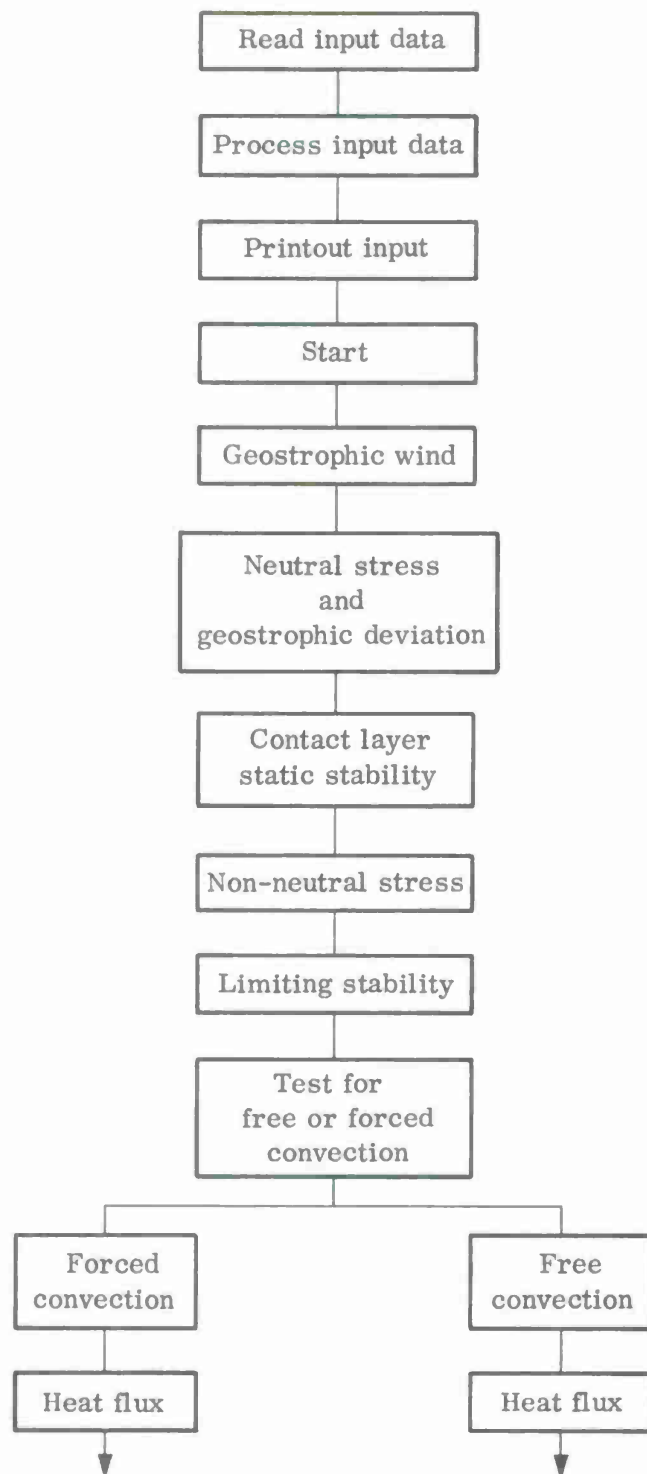


Fig. 25. Major computational steps for numerical model.

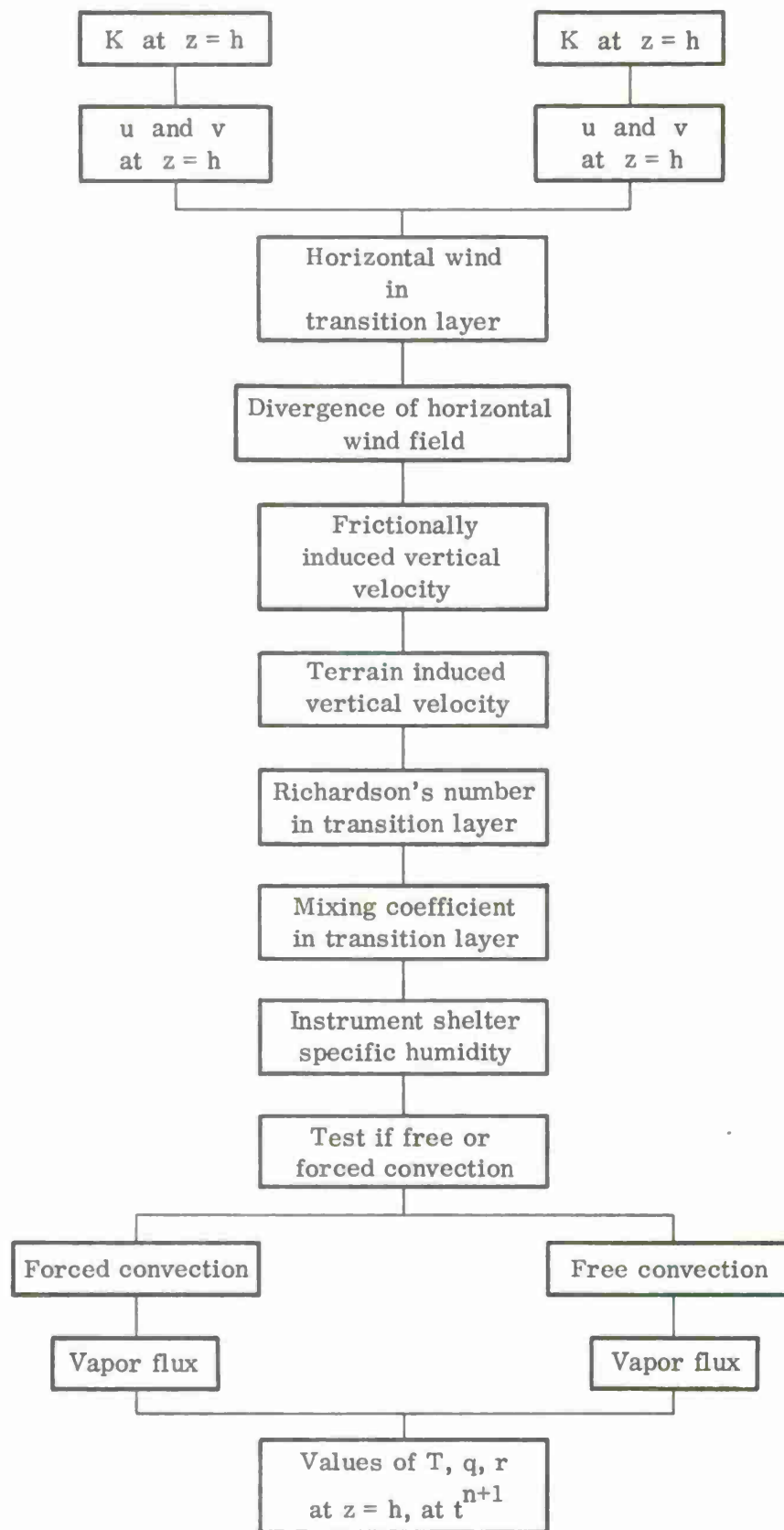


Fig. 25. (continued)

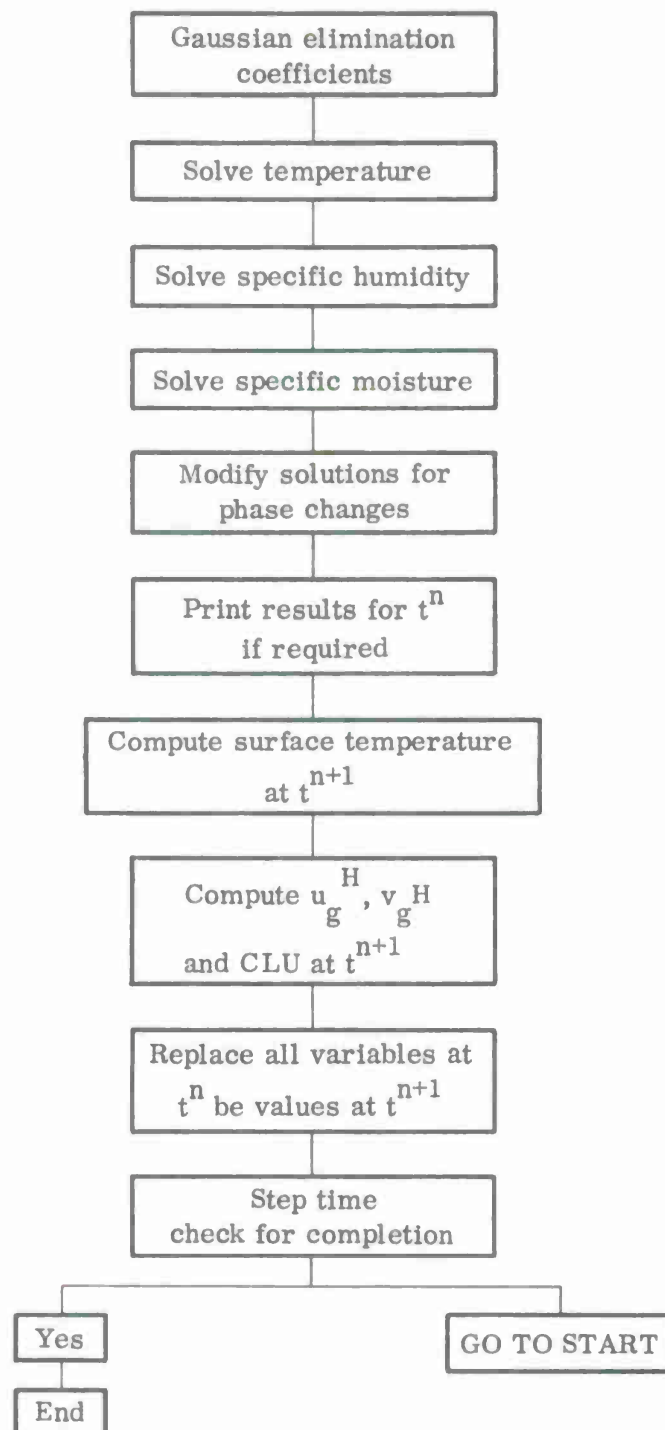


Fig. 25. (continued)

Read Input Data

The information relating to input data is given above. We will indicate here that there are two types of input quantities. The first type consists of a simple constant which will be unmodified during the computation. The second type consists of initial values of the dependent variables that are modified by the computation.

A computation is to be made which involves derivation of the height of the various levels above the ground.

$$Z_1 = (DZ)_1$$

For $k = 2, \dots, K$

$$Z_k = Z_{k-1} + (DZ)_k$$

The input values of temperature are in degrees centigrade and they are converted to degrees absolute. The coefficients, $RA_{\ell, m}^{II}$, which are given as input must be adjusted as follows:

$$RA_{\ell, m}^{II} = RA_{\ell, m}^{II} + RB_{\ell, m}^{II} \{1.8 * (TS_{\ell, m} - 273.2) + 32.0\}$$

Printout Input Data

This output is required to insure that the appropriate numerical values have been read into the computer storage. This output must include all the quantities indicated in the input data table by asterisks. It should also include Holerith characters sufficient to identify the case for which the data apply.

Geostrophic Wind

The computational formulas outlined here are used to determine the values of the geostrophic wind components which will subsequently be used to derive the actual wind components. These two wind fields may share memory locations. For clarity, we will use a subscript g on the symbols for the geostrophic components in these formulas but these may be omitted in the program.

The first step in the computation involves the evaluation of the geostrophic wind shear.

For $\ell = 1, \dots, L$; and $m = 1, \dots, M$:

$$A_{\ell, m} = \frac{0.5}{Z_k - Z_i} * \sum_{k=2}^{k=K} \left\{ (D2)_k * \left[\frac{1.0}{T_{\ell, m}^{k, n}} + \frac{1.0}{T_{\ell, m}^{k-1, n}} \right] \right\}$$

For $\ell = 2, \dots, L - 1$; $m = 2, \dots, M - 1$:

$$B_{\ell, m} = \frac{g * XM_{\ell, m}}{2.0 * D * f_{\ell, m}} * [A_{\ell, m+1} - A_{\ell, m-1}]$$

$$C_{\ell, m} = - \frac{g * XM_{\ell, m}}{2.0 * D * f_{\ell, m}} * [A_{\ell+1, m} - A_{\ell-1, m}]$$

For $\ell = 1, \dots, L$:

$$B_{\ell, 1} = B_{\ell, 2}$$

$$B_{\ell, M} = B_{\ell, M-1}$$

For $m = 1, \dots, M$:

$$C_{1, m} = C_{2, m}$$

$$C_{L, m} = C_{L-1, m}$$

For $m = 2, \dots, M - 1$:

$$B_{1, m} = B_{2, m}$$

$$B_{L, m} = B_{L-1, m}$$

For $\ell = 2, \dots, L - 1$:

$$C_{\ell, 1} = C_{\ell, 2}$$

$$C_{\ell, M} = C_{\ell, M-1}$$

Finally, we may compute the geostrophic wind field.

For $\ell = 1, \dots, L$; $m = 1, \dots, M$; $k = 1, \dots, K$:

$$\begin{aligned}
U_{g \ell, m}^{k, n} = & (U_g^H)_{\ell, m}^n * \left\{ 1.0 + \left[\frac{T_{\ell, m}^{1, n} - T_{\ell, m}^{K, n}}{T_{\ell, m}^{K, n}} \right] * \left[\frac{Z_K - Z_k}{Z_K - Z_1} \right] \right\} \\
& - T_{\ell, m}^{1, n} * B_{\ell, m} * [Z_K - Z_k] \\
& + \left(\frac{Z_K - Z_k}{Z_K - Z_1} \right) \left(\frac{T_{\ell, m}^{1, n} - T_{\ell, m}^{K, n}}{T_{\ell, m}^{K, n}} \right) \frac{g}{f} \frac{(XM)_{\ell, m}}{2.0 * D} [E_{\ell, m+1} - E_{\ell, m-1}]
\end{aligned}$$

$$\begin{aligned}
V_{g \ell, m}^{k, n} = & (v_g^H)_{\ell, m}^n * \left\{ 1.0 + \left[\frac{T_{\ell, m}^{1, n} - T_{\ell, m}^{K, n}}{T_{\ell, m}^{K, n}} \right] * \left[\frac{Z_K - Z_k}{Z_K - Z_1} \right] \right\} \\
& - T_{\ell, m}^{1, n} * C_{\ell, m} * [Z_K - Z_k] \\
& - \left(\frac{Z_K - Z_k}{Z_K - Z_1} \right) \left(\frac{T_{\ell, m}^{1, n} - T_{\ell, m}^{K, n}}{T_{\ell, m}^{K, n}} \right) * \frac{g}{f} * \frac{(XM)_{\ell, m}}{2.0 * D} * [E_{\ell+1, m} - E_{\ell-1, m}]
\end{aligned}$$

Neutral Stress and Geostrophic Deviation

The stress is symbolized by u_* and requires for its computation the value of the geostrophic wind speed at the surface. The geostrophic deviation is the angle (in radian measure) between the surface geostrophic wind and the actual wind in the contact layer.

For $\ell = 1, \dots, L$ and $m = 1, \dots, M$:

$$\begin{aligned}
A_{\ell, m} = & (u_g^H)_{\ell, m}^n * \left\{ 1.0 + \left[\frac{T_{\ell, m}^{1, n} - T_{\ell, m}^{K, n}}{T_{\ell, m}^{K, n}} \right] * \left[\frac{Z_K}{Z_K - Z_1} \right] \right\} \\
& + \frac{Z_K}{Z_K - Z_1} \left[\frac{T_{\ell, m}^{1, n} - T_{\ell, m}^{K, n}}{T_{\ell, m}^{K, n}} \right] \frac{g}{f_{\ell, m}} \frac{(XM)_{\ell, m}}{2.0 * D} [E_{\ell, m+1} - E_{\ell, m-1}] \\
& - T_{\ell, m}^{1, n} * B_{\ell, m} * Z_K
\end{aligned}$$

$$B_{\ell, m} = (v_g^H)_{\ell, m}^n * \left\{ 1.0 + \left[\frac{T_{\ell, m}^{1, n} - T_{\ell, m}^{K, n}}{T_{\ell, m}^{K, n}} \right] * \left[\frac{Z_K}{Z_K - Z_1} \right] \right\} \\ - T_{\ell, m}^{1, n} * C_{\ell, m} * Z_K \\ - \frac{Z_K}{Z_K - Z_1} \left[\frac{T_{\ell, m}^{1, n} - T_{\ell, m}^{K, n}}{T_{\ell, m}^{K, n}} \right] \frac{g}{f_{\ell, m}} \frac{(XM)_{\ell, m}}{2.0 * D} [E_{\ell+1, m} - E_{\ell-1, m}]$$

$$C_{\ell, m} = [(A_{\ell, m})^{** 2} + (B_{\ell, m})^{** 2}]^{1/2}$$

$$A_{\ell, m} = A_{\ell, m} \div C_{\ell, m}$$

$$B_{\ell, m} = B_{\ell, m} \div C_{\ell, m}$$

[Note that if $C_{\ell, m}$ is zero replace it by 100.0]

$$R_{\ell, m} = C_{\ell, m} \div [f_{\ell, m} * Z_{0 \ell, m}]$$

$$R_{\ell, m} = \ln [R_{\ell, m}] \div \ln (10.0)$$

$$u_{\ell, m}^* = C_{\ell, m} * [0.07625 - 0.00625 * R_{\ell, m}]$$

$$\phi_{\ell, m} = \frac{3.14159}{180.0} * [0.625 * (R_{\ell, m})^{** 2} - 12.75 * R_{\ell, m} + 80.625]$$

$$C_{\ell, m} = A_{\ell, m} * \cos [\phi_{\ell, m}] - B_{\ell, m} * \sin [\phi_{\ell, m}]$$

$$R_{\ell, m} = B_{\ell, m} * \cos [\phi_{\ell, m}] + A_{\ell, m} * \sin [\phi_{\ell, m}]$$

[Note that ϕ is in radians]

Contact-layer Static Stability

In order to determine the appropriate value for the stress and to decide if free- or forced-convection formulas are to be used in the contact layer, we must compute the static stability of the contact layer. We therefore evaluate

For $\ell = 1, \dots, L$ and $m = 1, \dots, M$:

$$A_{\ell, m} = [T_{\ell, m}^{1, n} - TS_{\ell, m}^n] + \gamma * [Z_1 - (Z_{0 \ell, m} + Z_{i \ell, m})]$$

Non-neutral Stress

Based on the sign of A computed in the equation above, we use one or another formula for the stress (u_*)

For $\ell = 1, \dots, L$ and $m = 1, \dots, M$:

If $A_{\ell, m} \geq 0$, set

$$u_{*, \ell, m} = 0.80 * u_{*, \ell, m}$$

If $A_{\ell, m} < 0$, set

$$u_{*, \ell, m} = 1.20 * u_{*, \ell, m}$$

The Limiting Stability

Having computed the non-neutral value of u_* , we may now determine the limiting value of the static stability for the use of forced-convection formulas.

For $\ell = 1, \dots, L$ and $m = 1, \dots, M$:

$$B_{\ell, m} = - \frac{\Theta}{g} * \frac{(u_{*, \ell, m})^{** 2}}{4.0 * \beta} * \frac{(\ln [Z_1 \div (Z_{0, \ell, m} + Z_i)])^{** 2}}{(\kappa)^{** 2} * [Z_1 - (Z_{0, \ell, m} + Z_i)]}$$

Test for Free or Forced Convection

For $\ell = 1, \dots, L$ and $m = 1, \dots, M$:

If $A_{\ell, m} > B_{\ell, m}$, set

$$I_{\ell, m} = 1$$

If $A_{\ell, m} \leq B_{\ell, m}$, set

$$I_{\ell, m} = 0$$

Free-convection Formulas

For $\ell = 1, \dots, L$ and $m = 1, \dots, M$:

If $I_{\ell, m} \neq 0$, do nothing.

If $I_{\ell, m} = 0$, set

$$HF_{\ell, m} = \left[\frac{\lambda^{2/3}}{3.0} * \frac{g}{\Theta}^{1/3} * \frac{A_{\ell, m}}{\left[\left(\frac{1}{Z_1} \right)^{1/3} - \left(\frac{1}{(Z_{0, \ell, m} + Z_i)} \right)^{1/3} \right]} \right]^{1/2}$$

$$\hat{K}_{\ell, m} = HF_{\ell, m} * \frac{g}{\Theta}^{1/3} * \lambda^{2/3} * (Z_1)^{4/3}$$

$$A_{\ell, m} = \frac{u_{*, \ell, m}}{\kappa} \ln \left[\frac{100 + Z_{0, \ell, m}}{Z_{0, \ell, m}} \right] - \left[\frac{3.0 * u_{*, \ell, m}^2 * 1.3}{\lambda^{2/3} \frac{g}{\Theta}^{1/3} HF_{\ell, m}} \right] \left[\left(\frac{1}{Z_1} \right)^{1/3} - \left(\frac{1}{Z_{0, \ell, m} + 100} \right)^{1/3} \right]$$

$$WSFC = \frac{u_{*, \ell, m}}{\kappa} \ln \left[\frac{122 + Z_{0, \ell, m}}{Z_{0, \ell, m}} \right]$$

$$(RATIO)_{\ell, m} = WSFC \div A_{\ell, m}$$

$$B_{\ell, m} = A_{\ell, m} * C_{\ell, m}$$

$$A_{\ell, m} = A_{\ell, m} * R_{\ell, m}$$

$$HF_{\ell, m} = - [(HF)_{\ell, m} ** 3.]$$

$$\text{Require } 10^4 \leq \hat{K}_{\ell, m} \leq 10^6$$

Forced-convection Formulas

For $\ell = 1, \dots, L$ and $m = 1, \dots, M$:

If $I_{\ell, m} = 0$, do nothing.

If $I_{\ell, m} \neq 0$, set

$$HF_{\ell, m} = - \left[\frac{\Theta * \ln (Z_1 \div (Z_{0, \ell, m} + Z_i)) * (u_{*, \ell, m})^3}{2.0 * g * \beta * \kappa * (Z_1 - (Z_{0, \ell, m} + Z_i))} \right] * \left\{ 1.0 - \left[1.0 + \frac{4.0 * g * \kappa^2 * (Z_1 - (Z_{0, \ell, m} + Z_i)) * A_{\ell, m}}{\Theta * (u_{*, \ell, m}) * \ln (Z_1 \div (Z_{0, \ell, m} + Z_i)) ** 2} \right]^{1/2} \right\}$$

If $A_{l,m} > 0$, compute

$$DUMYA = \left(\frac{\Theta}{\beta g} \right)^{1/2} \left[u_{*,l,m}^2 (Z_1 - Z_{i,l,m})^{1/2} \div (A_{l,m})^{1/2} \right]$$

$$DUMYB = \kappa Z_1 u_{*,l,m} \div \left[1.0 + (\beta g \kappa Z_1 HF_{l,m} \div (\Theta u_{*,l,m}^3)) \right]$$

If $DUMYA \leq DUMYB$, set

$$\hat{K}_{l,m} = 10^4$$

$$HF_{l,m} = 10^{-2} * \hat{K}_{l,m} * A_{l,m} \div [Z_1 - (Z_{i,l,m} + Z_{0,l,m})]$$

$$A_{l,m} = 0.41 * [(u_{g,l,m}^{1,n} ** 2 + v_{g,l,m}^{1,n} ** 2)^{1/2}]$$

$$RATIO_{l,m} = 2.0 * u_{*,l,m} \div A_{l,m}$$

$$B_{l,m} = A_{l,m} * C_{l,m}$$

$$A_{l,m} = A_{l,m} * R_{l,m}$$

If $DUMYA > DUMYB$, set

$$\hat{K}_{l,m} = DUMYB$$

$$A_{l,m} = \frac{u_{*,l,m} \ln \left[Z_1 \div Z_{0,l,m} \right]}{\kappa} + \left[\frac{\beta g (Z_1 - Z_{0,l,m}) HF_{l,m}}{\Theta u_{*,l,m}^2} \right]$$

$$WSFC = \frac{u_{*,l,m}}{\kappa} \ln \left[\left(122. + Z_{0,l,m} \right) / Z_{0,l,m} \right]$$

$$RATIO_{l,m} = WSFC \div A_{l,m}$$

$$B_{l,m} = A_{l,m} * C_{l,m}$$

$$A_{l,m} = A_{l,m} * R_{l,m}$$

If $A_{l,m} \leq 0$, compute

$$\hat{K}_{l,m} = \kappa Z_1 u_{*,l,m} \div \left[1.0 + \frac{\beta g \kappa Z_1 HF_{l,m}}{\Theta u_{*,l,m}^3} \right]$$

If $\hat{K}_{\ell, m} \leq 0$, set $I_{\ell, m} = 0$ and use free convection.

If $\hat{K}_{\ell, m} > 0$, compute

$$CON = \left[\frac{\lambda^{2/3}}{3.0} \left(\frac{g}{\Theta} \right)^{1/3} * \frac{A_{\ell, m}}{\left[\left(\frac{1}{Z_1} \right)^{1/3} - \left(\frac{1}{Z_{0\ell, m} + Z_{i\ell, m}} \right)^{1/3} \right]} \right]^{1/2}$$

If $ABS F(HF_{\ell, m}) < (CON)^3$, set

$I_{\ell, m} = 0$ and use free convection.

If $ABS F(HF_{\ell, m}) \geq (CON)^3$, set

$$A_{\ell, m} = \frac{u_{* \ell, m} \ln \left[Z_1 / Z_{0\ell, m} \right]}{\kappa} + \left[\frac{\beta g \left(Z_1 - Z_{0\ell, m} \right) HF_{\ell, m}}{\Theta u_{* \ell, m}^2} \right]$$

$$WSFC = \frac{u_{* \ell, m}}{\kappa} \ln \left[(122. + Z_{0\ell, m}) \div Z_{0\ell, m} \right]$$

$$RATIO_{\ell, m} = WSFC \div A_{\ell, m}$$

$$B_{\ell, m} = A_{\ell, m} * C_{\ell, m}$$

$$A_{\ell, m} = A_{\ell, m} * R_{\ell, m}$$

[Note that in each loop \hat{K} is to be forced to lie between 10^4 and 10^6 .]

Horizontal Wind in the Transition Layer

We recall here that $u_g(v_g)$ and $u(v)$ will share storage locations.

For $\ell = 1, \dots, L$ and $m = 1, \dots, M$:

$$C_{\ell, m} = A_{\ell, m} - v_{g \ell, m}^{1, n}$$

$$B_{\ell, m} = B_{\ell, m} - u_{g \ell, m}^{1, n}$$

$$A_{\ell, m} = [f_{\ell, m} \div (2.0 * \hat{K}_{\ell, m})]^{1/2}$$

For $\ell = 1, \dots, L$; $m = 1, \dots, M$; and $k = 1, \dots, K$:

$$\begin{aligned}
 u_{\ell, m}^k &= u_{g \ell, m}^k + \left[\exp \left[-A_{\ell, m} * (Z_k - Z_1) \right] \right. \\
 &\quad * \left[B_{\ell, m} * \cos \left[A_{\ell, m} * (Z_k - Z_1) \right] \right. \\
 &\quad \left. \left. + C_{\ell, m} * \sin \left[A_{\ell, m} * (Z_k - Z_1) \right] \right] \right] \\
 v_{\ell, m}^k &= v_{g \ell, m}^k + \left[\exp \left[-A_{\ell, m} * (Z_k - Z_1) \right] \right. \\
 &\quad * \left[C_{\ell, m} * \cos \left[A_{\ell, m} * (Z_k - Z_1) \right] \right. \\
 &\quad \left. \left. - B_{\ell, m} * \sin \left[A_{\ell, m} * (Z_k - Z_1) \right] \right] \right]
 \end{aligned}$$

Divergence of the Horizontal Wind Field

This computation is required as a preliminary to the calculation of the "frictionally-induced" vertical velocity.

For $\ell = 2, \dots, L - 1$; $M = 2, \dots, M - 1$; $k = 1, \dots, K$:

$$(AA)_{\ell, m}^k = \frac{XM_{\ell, m}}{2.0 * D} * \left[(u_{\ell+1, m}^k - u_{\ell-1, m}^k) + (v_{\ell, m+1}^k - v_{\ell, m-1}^k) \right]$$

Frictionally-induced Vertical Velocity

The parameter is denoted by w and is calculated as follows:

For $\ell = 2, \dots, L - 1$ and $m = 2, \dots, M - 1$:

$$\begin{aligned}
 w_{\ell, m}^1 &= 0 \\
 w_{\ell, m}^2 &= -0.5 * (DZ)_2 * \left[(AA)_{\ell, m}^2 + (AA)_{\ell, m}^1 \right]
 \end{aligned}$$

For $k = 3, \dots, K$:

$$w_{\ell, m}^k = w_{\ell, m}^{k-1} - 0.5 * (DZ)_k * \left[(AA)_{\ell, m}^k + (AA)_{\ell, m}^{k-1} \right]$$

If $\ell = 1, L$ or $m = 1, M$, $w_{\ell, m}^k \equiv 0$ for all k .

Terrain-induced Vertical Velocity

The motion of the air normal to a terrain gradient forces an ascent or descent to conform to the terrain surface. This vertical motion is computed here using the operator defined in Subsection 3.2.

For $\ell = 1, \dots, L$; $m = 1, \dots, M$; $k = 1, \dots, K$:

$$\hat{w}_{\ell, m}^k = [X(E)]_{\ell, m}^k + [Y(E)]_{\ell, m}^k$$

Richardson's Number and the Mixing Coefficients in the Transition Layer

For $\ell = 1, \dots, L$; $m = 1, \dots, M$; $k = 2, \dots, K$:

$$A = \left[\frac{T_{\ell, m}^{k, n} - T_{\ell, m}^{k-1, n}}{(DZ)_k} + \gamma \right]$$
$$P = \left[u_{\ell, m}^{k, n} - u_{\ell, m}^{k-1, n} \right]^2 + \left[v_{\ell, m}^{k, n} - v_{\ell, m}^{k-1, n} \right]^2$$

If $A > 0$,

and if $P = 0$, set

$$K_{\ell, m}^k = 10^4$$

but if $P \neq 0$, set

$$BRI = \frac{\beta g}{\Theta} (DZ)_k^2 * A \div P$$

If $BRI \geq 1.0$, set

$$K_{\ell, m}^{k, n} = 10^4$$

If $BRI < 1.0$, set

$$K_{\ell, m}^{k, n} = \left[\frac{\kappa (Z_k + Z_{k-1}) (1 - BRI)}{2.0} \right]^2 * \frac{P^{1/2}}{(DZ)_k}$$

If $A \leq 0$,

and if $P = 0$, set

$$K_{\ell, m}^{k, n} = \frac{\lambda (Z_k - Z_{k-1})^2}{4.0} \left(- \frac{gA}{\Theta} \right)^{1/2}$$

If $I_{l,m} = 1$,

and if $\hat{K}_{l,m} = 10^4$, set

$$VF_{l,m} = \hat{K}_{l,m} \left[\frac{q_{l,m}^{1,n} - \hat{q}_{l,m}}{Z_1 - (Z_{0,l,m} + Z_{i,l,m})} \right]$$

but if $\hat{K}_{l,m} > 10^4$, set

$$VF_{l,m} = \left[\frac{[q_{l,m}^{1,n} - \hat{q}_{l,m}] * u_{l,m}^* * \kappa}{\beta * \kappa * g^* [Z_1 - (Z_{0,l,m} + Z_i)] * [HF_{l,m}]} \right] \left[\ln \frac{Z_1}{Z_{0,l,m} + Z_i} + \frac{[\Theta * (u_{l,m}^*) ** 3.]}{[\Theta * (u_{l,m}^*) ** 3.]} \right]$$

Values of T, q, and r at Z = H at t = t_{n+1}

For $l = 1, \dots, L$ and $m = 1, \dots, M$:

$$T_{l,m}^{K,n+1} = T_{l,m}^{K,n} + (DT) * \left[- [X(T)]_{l,m}^K - [Y(T)]_{l,m}^K - \gamma * \left(\hat{w}_{l,m}^K + w_{l,m}^K \right) - w_{l,m}^K * \left[\frac{T_{l,m}^{K,n} - T_{l,m}^{K-1,n}}{(DZ)_K} \right] \right]$$

$$q_{l,m}^{K,n+1} = q_{l,m}^{K,n} + (DT) * \left[- [X(q)]_{l,m}^K - [Y(q)]_{l,m}^K - w_{l,m}^K * \left[\frac{q_{l,m}^{K,n} - q_{l,m}^{K-1,n}}{(DZ)_K} \right] \right]$$

$$r_{l,m}^{K,n+1} = r_{l,m}^{K,n} + (DT) * \left[- [X(r)]_{l,m}^K - [Y(r)]_{l,m}^K - w_{l,m}^K * \left[\frac{r_{l,m}^{K,n} - r_{l,m}^{K-1,n}}{(DZ)_K} \right] \right]$$

Gaussian Elimination Coefficients (Temperature, Specific Humidity, and Specific Moisture)

These four blocks are united here since a separate description of each section would be difficult and the programmer will probably use the same basic routine for

each of the 3 equations.

The differential equations to be solved are replaced by difference equations. If we let U represent a general dependent variable, the difference equations are all of the form

$$a_{\ell, m}^k U_{\ell, m}^{k-1, n+1} + b_{\ell, m}^k U_{\ell, m}^{k, n+1} + c_{\ell, m}^k U_{\ell, m}^{k+1, n+1} = d_{\ell, m}^k \quad (k = 1, \dots, K-1)$$

This is a special form of the general matrix equation,

$$A_{i, j} U_j = D_i \quad (i = 1, \dots, K - 1; \quad j = 1, \dots, K - 1)$$

in which $A_{i, j}$ is a $(K - 1) (K - 1)$ matrix. In our case, only the three main diagonals of $A_{i, j}$ are non-zero.

The method for solving the system is an adaptation of the Gaussian elimination scheme described in the book by Forsythe and Wasow [9]. In the following we will describe the method.

Method

Step 1: Find the element in $A_{i, j}$ which has the greatest absolute value.

Let the element be $A_{R, S}$ (i.e., the coefficient for which $i = R$ and $j = S$).

Step 2: Set

$$A_{R, j}^{(1)} = A_{R, j} \div A_{R, S} \quad (j = 1, \dots, K - 1)$$

and

$$D_R^{(1)} = D_R \div A_{R, S}$$

Step 3: For all i (except $i = R$) and for all j , set

$$A_{i, j}^{(1)} = A_{i, j} - A_{i, S} * A_{R, j}^{(1)}$$

and

$$D_i^{(1)} = D_i - A_{i, S} * D_R^{(1)}$$

Step 4: Find the element of the modified matrix $A_{i, j}^{(1)}$ which is greatest in absolute value; exclude from consideration all elements for which $i = R$. Let the element chosen be $A_{P, T}^{(1)}$.

Step 5: Set

$$A_{P,j}^{(2)} = A_{P,j}^{(1)} \div A_{P,T}^{(1)} \quad (j = 1, \dots, K - 1)$$

$$D_P^{(2)} = D_P^{(1)} \div A_{P,T}^{(1)}$$

Step 6: For all i (except i = P) and for all j,

$$A_{i,j}^{(2)} = A_{i,j}^{(1)} - A_{i,T}^{(1)} * A_{P,j}^{(2)}$$

$$D_{i,j}^{(2)} = D_{i,j}^{(1)} - A_{i,T}^{(1)} * D_P^{(2)}$$

Now the coefficients $A_{i,j}^{(2)}$ are scanned to determine the element largest in absolute value (those elements are excluded, however, for which i = P or R).

The basic steps are iterated until one arrives at the final coefficient matrix $A_{i,j}^{(K-1)}$. This matrix will have just one non-zero element in each row which will have the value unity. The solution for the U_j is found then as follows:

If $A_{I,J}^{(K-1)}$ is unity,

$$U_J = D_J^{(K-1)}.$$

We note that at each horizontal grid point, each of the three unknowns must be obtained by an application of this method using the appropriate coefficients.

Derivation of the Temperature Difference Equations

If we omit the term, $(dT/dt)_w$, the differential equation may be replaced as follows:

For $k = 1$, $\ell = \lambda$, $m = \mu$:

$$\begin{aligned} \frac{T_{\lambda,\mu}^{1,n+1} - T_{\lambda,\mu}^{1,n}}{(DT)} = & - [X(T)]_{\lambda,\mu}^1 - [Y(T)]_{\lambda,\mu}^1 - \gamma \hat{w}_{\lambda,\mu}^1 \\ & + \frac{2.0}{(DZ)_2} * \left[K_{\lambda,\mu}^2 * \left[\gamma + \frac{T_{\lambda,\mu}^{2,n+1} - T_{\lambda,\mu}^{1,n+1}}{(DZ)_2} \right] - HF_{\lambda,\mu} \right] \end{aligned}$$

For $k = 2, \dots, K - 1; \ell = \lambda, m = \mu$:

$$\begin{aligned} \frac{T_{\lambda, \mu}^{k, n+1} - T_{\lambda, \mu}^{k, n}}{(DT)} = & - [X(T)]_{\lambda, \mu}^k - [Y(T)]_{\lambda, \mu}^k - \gamma^* \left[\hat{w}_{\lambda, \mu}^k + w_{\lambda, \mu}^k \right] \\ & - w_{\lambda, \mu}^k * \left[\frac{T_{\lambda, \mu}^{k+1, n+1} - T_{\lambda, \mu}^{k-1, n+1}}{[(DZ)_{k+1} + (DZ)_k]} \right] \\ & + \frac{2.0}{[(DZ)_{k+1} + (DZ)_k]} * \left[K_{\lambda, \mu}^{k+1} * \left[\gamma + \frac{T_{\lambda, \mu}^{k+1, n+1} - T_{\lambda, \mu}^{k, n+1}}{(DZ)_{k+1}} \right] \right. \\ & \left. - K_{\lambda, \mu} * \left[\gamma + \frac{T_{\lambda, \mu}^{k, n+1} - T_{\lambda, \mu}^{k-1, n+1}}{(DZ)_k} \right] \right] \end{aligned}$$

Combining the coefficients of the unknowns, $T_{\lambda, \mu}^{k, n+1}$ ($k = 1, \dots, K - 1$), the system of algebraic equations may be written

$$a_{\lambda, \mu}^k T_{\lambda, \mu}^{k-1, n+1} + b_{\lambda, \mu}^k T_{\lambda, \mu}^{k, n+1} + c_{\lambda, \mu}^k T_{\lambda, \mu}^{k+1, n+1} = d_{\lambda, \mu}^k$$

in which the coefficients are defined as follows:

For $k = 1$

$$\begin{aligned} a_{\lambda, \mu}^1 &= 0 \\ b_{\lambda, \mu}^1 &= - \left[\frac{1}{(DT)} + \frac{2.0 * K_{\lambda, \mu}^2}{[(DZ)_2]^2} \right] \\ c_{\lambda, \mu}^1 &= \frac{2.0 * K_{\lambda, \mu}^2}{[(DZ)_2]^2} \\ d_{\lambda, \mu}^1 &= \gamma * \hat{w}_{\lambda, \mu}^1 + [X(T)]_{\lambda, \mu}^1 + [Y(T)]_{\lambda, \mu}^1 \\ &\quad - \frac{T_{\lambda, \mu}^{1, n}}{(DT)} - \frac{2.0 * \gamma * K_{\lambda, \mu}^2}{(DZ)_2} + \frac{2.0 * HF_{\lambda, \mu}}{(DZ)_2} \end{aligned}$$

For $k = 2, \dots, K - 2$:

$$\begin{aligned}
 a_{\lambda, \mu}^k &= \left[0.5 w_{\lambda, \mu}^k + \frac{K_{\lambda, \mu}^k}{(DZ)_k} \right] \div \left[0.5 * [(DZ)_{k+1} + (DZ)_k] \right] \\
 b_{\lambda, \mu}^k &= - \left[\frac{1}{(DT)} + \left[\frac{2.0}{(DZ)_{k+1} + (DZ)_k} \right] * \left[\frac{K_{\lambda, \mu}^{k+1}}{(DZ)_{k+1}} + \frac{K_{\lambda, \mu}^k}{(DZ)_k} \right] \right] \\
 c_{\lambda, \mu}^k &= \left[-0.5 w_{\lambda, \mu}^k + \frac{K_{\lambda, \mu}^{k+1}}{(DZ)_{k+1}} \right] \div \left[0.5 * [(DZ)_{k+1} + (DZ)_k] \right] \\
 d_{\lambda, \mu}^k &= \gamma * \left(w_{\lambda, \mu}^k + \hat{w}_{\lambda, \mu}^k \right) + [X(T)]_{\lambda, \mu}^k + [Y(T)]_{\lambda, \mu}^k \\
 &\quad - \frac{T_{\lambda, \mu}^{k, n}}{(DT)} + \frac{2.0 * \gamma}{(DZ)_{k+1} + (DZ)_k} * \left(K_{\lambda, \mu}^k - K_{\lambda, \mu}^{k+1} \right)
 \end{aligned}$$

For $k = K - 1$:

$$\begin{aligned}
 a_{\lambda, \mu}^{K-1} &= \left[0.5 w_{\lambda, \mu}^{K-1} + \frac{K_{\lambda, \mu}^{K-1}}{(DZ)_{K-1}} \right] \div \left[0.5 * [(DZ)_K + (DZ)_{K-1}] \right] \\
 b_{\lambda, \mu}^{K-1} &= - \left[\frac{1}{(DT)} + \left[\frac{2.0}{[(DZ)_K + (DZ)_{K-1}]} \right] * \left[\frac{K_{\lambda, \mu}^K}{(DZ)_K} + \frac{K_{\lambda, \mu}^{K-1}}{(DZ)_{K-1}} \right] \right] \\
 c_{\lambda, \mu}^{K-1} &= 0 \\
 d_{\lambda, \mu}^{K-1} &= \gamma * \left[w_{\lambda, \mu}^{K-1} + \hat{w}_{\lambda, \mu}^{K-1} \right] + [X(T)]_{\lambda, \mu}^{K-1} + [Y(T)]_{\lambda, \mu}^{K-1} \\
 &\quad - \frac{T_{\lambda, \mu}^{K-1, n}}{(DT)} + \frac{2.0 * \gamma}{[(DZ)_K + (DZ)_{K-1}]} * \left[K_{\lambda, \mu}^{K-1} - K_{\lambda, \mu}^K \right] \\
 &\quad + \left[0.5 w_{\lambda, \mu}^{K-1} - \frac{K_{\lambda, \mu}^K}{(DZ)_K} \right] * T_{\lambda, \mu}^{K, n+1} \div \left[0.5 * [(DZ)_K + (DZ)_{K-1}] \right]
 \end{aligned}$$

[Note that $T_{\lambda, \mu}^{K, n+1}$ is a known quantity.]

Derivation of the Specific Humidity Equation

Again, neglecting the additive term, $(dq/dt)_c$, the differential equation governing the specific humidity, q , may be replaced by the difference equations

For $k = 1, \ell = \lambda; m = \mu$:

$$\begin{aligned} \frac{q_{\lambda, \mu}^{1, n+1} - q_{\lambda, \mu}^{1, n}}{(DT)} = & - [X(q)]_{\lambda, \mu}^1 - [Y(q)]_{\lambda, \mu}^1 \\ & + \frac{2.0}{(DZ)_2} * \left[K_{\lambda, \mu}^2 * \left[\frac{q_{\lambda, \mu}^{2, n+1} - q_{\lambda, \mu}^{1, n+1}}{(DZ)_2} \right] - VF_{\lambda, \mu} \right] \end{aligned}$$

For $k = 2, \dots, K - 1; \ell = \lambda; m = \mu$:

$$\begin{aligned} \frac{q_{\lambda, \mu}^{k, n+1} - q_{\lambda, \mu}^{k, n}}{(DT)} = & - [X(q)]_{\lambda, \mu}^k - [Y(q)]_{\lambda, \mu}^k \\ & - w_{\lambda, \mu}^k * \left[\frac{q_{\lambda, \mu}^{k+1, n+1} - q_{\lambda, \mu}^{k-1, n+1}}{(DZ)_{k+1} + (DZ)_k} \right] \\ & + \frac{2.0}{[(DZ)_{k+1} + (DZ)_k]} \left[K_{\lambda, \mu}^{k+1} * \frac{q_{\lambda, \mu}^{k+1, n+1} - q_{\lambda, \mu}^{k, n+1}}{(DZ)_{k+1}} \right] \\ & - K_{\lambda, \mu}^k * \left[\frac{q_{\lambda, \mu}^{k, n+1} - q_{\lambda, \mu}^{k-1, n+1}}{(DZ)_k} \right] \end{aligned}$$

Combining the coefficients of the unknowns, $q_{\lambda, \mu}^{k, n+1}$ ($k = 1, \dots, K - 1$), one may put the system of difference equations in the form

$$a_{\lambda, \mu}^k q_{\lambda, \mu}^{k-1, n+1} + b_{\lambda, \mu}^k q_{\lambda, \mu}^{k, n+1} + c_{\lambda, \mu}^k q_{\lambda, \mu}^{k+1, n+1} = e_{\lambda, \mu}^k, \quad (k = 1, \dots, K - 1)$$

The coefficients a, b , and c are defined as for the temperature equation. The coefficients $e_{\lambda, \mu}^k$ are defined as follows:

$$e_{\lambda, \mu}^1 = [X(q)]_{\lambda, \mu}^1 + [Y(q)]_{\lambda, \mu}^1 - \frac{q_{\lambda, \mu}^{\ell, n}}{(DT)} + \frac{2.0 VF_{\lambda, \mu}}{(DZ)_2}$$

For $k = 2, \dots, K - 2$:

$$e_{\lambda, \mu}^k = [X(q)]_{\lambda, \mu}^k + [Y(q)]_{\lambda, \mu}^k - \frac{q_{\lambda, \mu}^{k, n}}{(DT)}$$

For $k = K - 1$

$$e_{\lambda, \mu}^{K-1} = [X(q)]_{\lambda, \mu}^{K-1} + [Y(q)]_{\lambda, \mu}^{K-1} + \frac{w_{\lambda, \mu}^{K-1} * q_{\lambda, \mu}^{K, n+1}}{(DZ)_K + (DZ)_{K-1}} - \frac{2.0 * K_{\lambda, \mu}^K * q_{\lambda, \mu}^{K, n+1}}{(DZ)_K * [(DZ)_K + (DZ)_{K-1}]} - \frac{q_{\lambda, \mu}^{K-1, n}}{(DT)}$$

Derivation of the Specific Moisture Equation

The differential equation governing the specific moisture r is replaced by the system of difference equations.

For $k = 1, \ell = \lambda, m = \mu$:

$$\frac{r_{\lambda, \mu}^{1, n+1} - r_{\lambda, \mu}^{1, n}}{(DT)} = - [X(r)]_{\lambda, \mu}^1 - [Y(r)]_{\lambda, \mu}^1 + \frac{2.0}{(DZ)_2} * \left[K_{\lambda, \mu}^2 * \left[\frac{r_{\lambda, \mu}^{2, n+1} - r_{\lambda, \mu}^{1, n+1}}{(DZ)_2} \right] - VF_{\lambda, \mu} \right]$$

For $k = 2, \dots, K - 1; \ell = \lambda; m = \mu$:

$$\begin{aligned} \frac{r_{\lambda, \mu}^{k, n+1} - r_{\lambda, \mu}^{k, n}}{(DT)} = & - [X(r)]_{\lambda, \mu}^k - [Y(r)]_{\lambda, \mu}^k \\ & - w_{\lambda, \mu}^k * \left[\frac{r_{\lambda, \mu}^{k+1, n+1} - r_{\lambda, \mu}^{k-1, n+1}}{(DZ)_{k+1} + (DZ)_k} \right] \\ & + \frac{2.0}{[(DZ)_{k+1} + (DZ)_k]} * \left[K_{\lambda, \mu}^{k+1} \left[\frac{r_{\lambda, \mu}^{k+1, n+1} - r_{\lambda, \mu}^{k, n+1}}{(DZ)_{k+1}} \right] \right. \\ & \left. - K_{\lambda, \mu}^k * \left[\frac{r_{\lambda, \mu}^{k, n+1} - r_{\lambda, \mu}^{k-1, n+1}}{(DZ)_k} \right] \right] \end{aligned}$$

Combining the coefficients of the unknowns $r_{\lambda, \mu}^{k, n+1}$ ($k = 1, \dots, K - 1$), the system of difference equations may be put in the form

$$a_{\lambda, \mu}^k r_{\lambda, \mu}^{k-1, n+1} + b_{\lambda, \mu}^k r_{\lambda, \mu}^{k, n+1} + c_{\lambda, \mu}^k r_{\lambda, \mu}^{k+1, n+1} = g_{\lambda, \mu}^k \quad (k = 1, \dots, K - 1)$$

The coefficients a , b , and c are identical to those defined above. The coefficients g are defined as follows:

For $k = 1$:

$$g_{\lambda, \mu}^1 = [X(r)]_{\lambda, \mu}^1 + [Y(r)]_{\lambda, \mu}^1 - \frac{r_{\lambda, \mu}^{1, n}}{(DT)} + \frac{2.0 \text{ V F}_{\lambda, \mu}}{(DZ)_2}$$

For $k = 2, \dots, K - 2$:

$$g_{\lambda, \mu}^k = [X(r)]_{\lambda, \mu}^k + [Y(r)]_{\lambda, \mu}^k - \frac{r_{\lambda, \mu}^{k, n}}{(DT)},$$

For $k = K - 1$:

$$g_{\lambda, \mu}^{K-1} = [X(r)]_{\lambda, \mu}^{K-1} + [Y(r)]_{\lambda, \mu}^{K-1} + \frac{w_{\lambda, \mu}^{K-1} * r_{\lambda, \mu}^{K, n+1}}{(DZ)_K + (DZ)_{K-1}} - \frac{2.0 * K_{\lambda, \mu}^K * r_{\lambda, \mu}^{K, n+1}}{(DZ)_K * [(DZ)_K + (DZ)_{K-1}]} - \frac{r_{\lambda, \mu}^{K-1, n}}{(DT)}$$

Modify Solutions for Phase Changes

Application of the method outlined above will yield values for T , r , and q at $t = t_{n+1}$. These values are now subject to an examination to determine if they should be modified due to phase changes in the water substance. We will repeat the technique here to insure compatibility in our notation.

For $k = 1, \dots, K$; $\ell = 1, \dots, L$ and $m = 1, \dots, M$:

$$TG = T_{\ell, m}^{k, n+1}, \quad QG = q_{\ell, m}^{k, n+1}, \quad RG = r_{\ell, m}^{k, n+1}$$

$$QS = \frac{3.8 * 10^{-3}}{1.013 - 1.065 * 10^{-6} * [Z_k + E_{\ell, m}]} * \exp \left[17.25 * \frac{TG - 273.0}{TG - 35.7} \right]$$

$$CT = \frac{[QG - QS] * [TG ** 2]}{5.394 * 10^3 * QS + 4.01 * 10^{-4} * [TG ** 2]}$$

$$CQ = - 4.01 * 10^{-4} * CT$$

One next performs the logic and computations shown in Fig. 26.

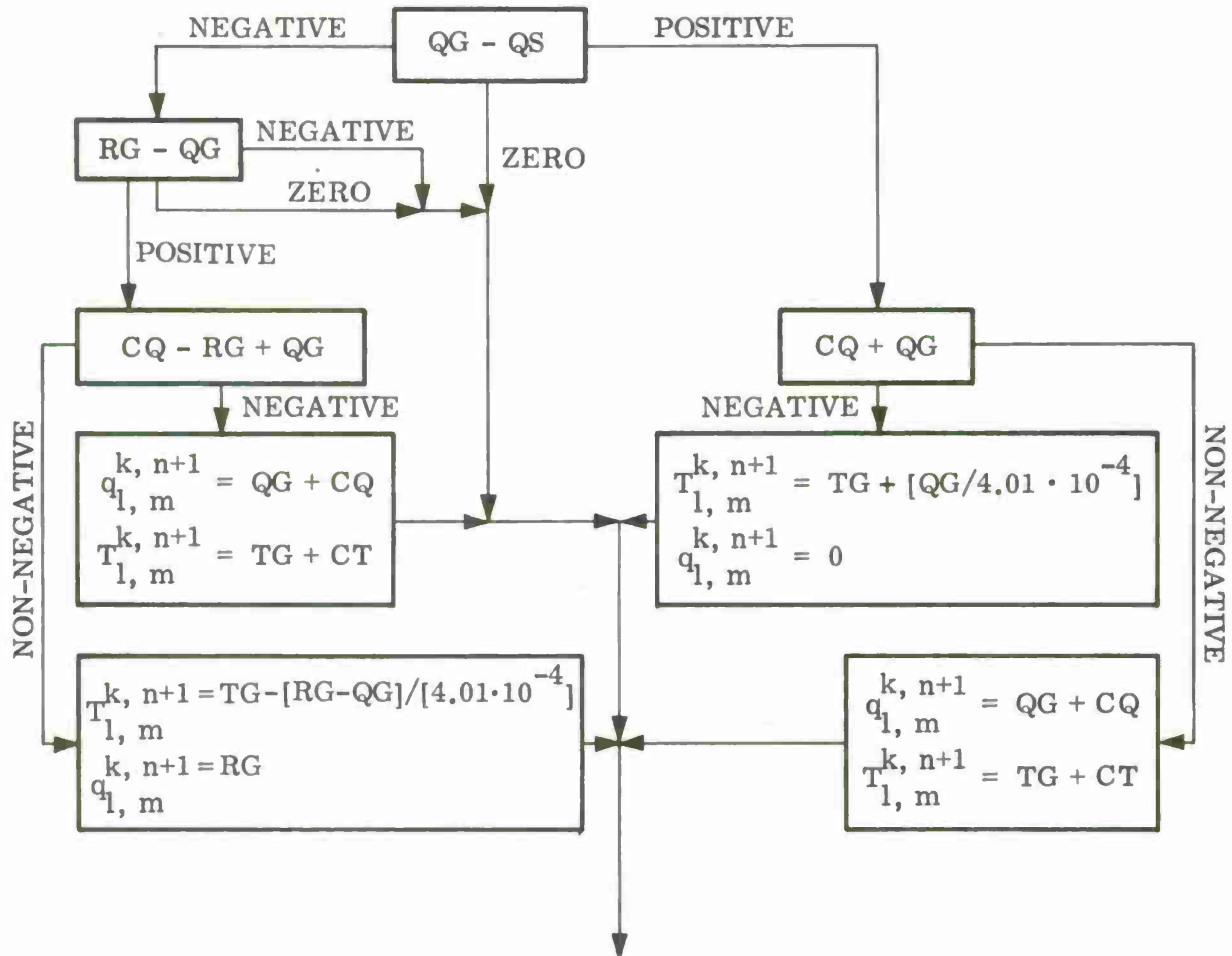


Fig. 26. Logic and computations.

Print Results

In the section on output, we indicate the character of the output which is desired. This point in the computational procedure appears to be a good point at which to print the results obtained up to $t = t_n$.

Surface Temperature at $t = t_{n+1}$

The value of the air temperature at the level of the instrument shelter (denoted by TS) will be permitted to change in response to diurnal radiation and to thermal advection. The computation is carried out as follows.

For $\ell = 1, \dots, L$ and $m = 1, \dots, M$:

(Not performed for grid points over the ocean for which $Z_i = 0$.)

$$TLAT = \text{TANF} (SLAT_{\ell, m})$$

$$P = \text{SQRTF} [1. - (C3 * (TLAT)_{\ell, m})^{** 2}]$$

$$R = 6.0 + 12.0 * [\text{SQRTF} (1.0 - P)] * [1.5707288 - 0.2121144 * P + 0.0742610 * (P^{**2}) - 0.0187293 * (P^{**3})] / [3.14159]$$

$$E = \text{TIME} / 3600.0$$

$$XMR = (SLNG_{\ell, m} - 75.) / 15.$$

$$\text{TIMER} = E - XMR$$

$$\text{If } \text{TIMER} \geq 24 \text{ set } \text{TIMER} = \text{TIMER} - 24$$

$$TX = \text{TIMER} - R$$

$$XX = 0.$$

If $0 \leq TX \leq 2.0 * (12.0 - R)$, set

$$XX = 1$$

$$ST = XX * [C1 \sin (SLAT_{\ell, m}) - C2 * \cos (SLAT_{\ell, m}) * \cos (3.14159 * \text{TIMER} / 12.0)]$$

$$YY = 0$$

If $0 \leq TX \leq 12.0 - R$, set

$$YY = 1$$

$$RT = YY * 3.14159 * C2 * \cos (SLAT_{\ell, m}) * \sin (3.14159 * \text{TIMER} / 12.0)$$

$$II = ICLU_{\ell, m}^n$$

For $k = 1, \dots, K$:

$$QS = \frac{3.8 \times 10^{-3}}{1.013 - 1.065 \times 10^{-6} (Z_{0\ell, m} + Z_{i\ell, m} + E_{\ell, m})} \\ * \exp \left[17.25 * \left[\frac{T_{\ell, m}^{k, n+1} - 273.0}{T_{\ell, m}^{k, n+1} - 35.7} \right] \right]$$

If $q_{\ell, m}^{k, n+1} \div QS > 0.8$ for any k , set

$$II = 3$$

$$RADCHG = \frac{0.5556 (DT)}{3600} \left[-1.8 * RB_{\ell, m}^{II} * TS_{\ell, m} \right. \\ + 459.67 * RB_{\ell, m}^{II} + RA_{\ell, m}^{II} + RC_{\ell, m}^{II} * ST \\ \left. + RD_{\ell, m}^{II} * RT \right]$$

$$ADVCHG = (DT) * RATIO_{\ell, m} * [- X(TS)_{\ell, m}^1 - Y(TS)_{\ell, m}^1 - \hat{w}_{\ell, m}^1 * \gamma]$$

$$TS_{\ell, m} = TS_{\ell, m} + RADCHG + ADVCHG$$

Surface Relative Humidity at $t = t_{n+1}$

The value of the relative humidity at the level of the instrument shelter is computed as follows.

For $\ell = 1, \dots, L$; $m = 1, \dots, M$:

$$QS = \frac{3.8 \times 10^{-3}}{[1.013 - 1.065 \times 10^{-6} (Z_{0\ell, m} + Z_i + E_{\ell, m})]} \\ * \exp \left[17.25 * \left[\frac{TS_{\ell, m} - 273.}{TS_{\ell, m} - 35.7} \right] \right]$$

$$RHS_{\ell, m} = [(1 - (WET)_{\ell, m}) * q_{\ell, m}^{1, n+1} / QS] + (WET)_{\ell, m}$$

Compute u_g^H , v_g^H , and ICLU at $t = t_{n+1}$

The values of u_g^H and v_g^H at $t = t_{n+1}$ are to be computed by quadratic interpolation between input quantities given at six-hour intervals. Let us denote these input quantities by $UGH1_{\ell,m}$; $UGH2_{\ell,m}$; $UGH3_{\ell,m}$; $VGH1_{\ell,m}$; $VGH2_{\ell,m}$; $VGH3_{\ell,m}$. The computation may then proceed as follows: set

$$TAU = (n + 1) * (DT) / (6.0 * 3600.0)$$

For $\ell = 1, \dots, L$; and $m = 1, \dots, M$:

$$AF = [4. * UGH2_{\ell,m} - UGH3_{\ell,m} - 3. * UGH1_{\ell,m}] / 2.0$$

$$BF = [UGH3_{\ell,m} - 2.0 * UGH2_{\ell,m} + UGH1_{\ell,m}] / 2.0$$

$$u_{g\ell,m}^H = UGH1_{\ell,m} + AF * TAU + BF * (TAU ** 2)$$

$$AF = [4. * VGH2_{\ell,m} - VGH3_{\ell,m} - 3. * VGH1_{\ell,m}] / 2.0$$

$$BF = [VGH3_{\ell,m} - 2.0 * VGH2_{\ell,m} + VGH1_{\ell,m}] / 2.0$$

$$v_{g\ell,m}^H = VGH1_{\ell,m} + AF * TAU + BF * (TAU ** 2)$$

To compute the appropriate value of ICLU at $t = t_{n+1}$ we make use of characteristic values of ICLU over six-hour intervals. Let these input quantities be denoted by $ICLU1_{\ell,m}$ and $ICLU2_{\ell,m}$.

Having computed TAU as above, $ICLU_{\ell,m}$ is determined as follows:

If $TAU \leq 1$, set

$$ICLU_{\ell,m} = ICLU1_{\ell,m}$$

If $TAU > 1$, set

$$ICLU_{\ell,m} = ICLU2_{\ell,m}$$

Replace Values at t_n by Values at t_{n+1}

The newly-computed time-dependent quantities may now replace the values previously stored at level n . The old values are lost. The locations reserved for the unknowns at $n + 1$ should now be set equal to zero.

Step Time

Set $\text{TIME} = \text{TIME} + \text{DT}$ and adjust indices as required.

(Check if Computation is Completed)

REFERENCES

1. Appleby, J. F. and W. D. Ohmstede, 1964: Numerical Solution of the Distribution of Wind and Turbulence in the Planetary Boundary Layer, Meteorol. Res. Notes No. 8, Meteorol. Dept., USAERDA, Fort Huachuca, Ariz.
2. Árnason, G., J. P. Gerrity, and A. Pavlowitz, 1963: Large-scale cloud Prediction: A Survey and an Appraisal, Tech. Rpt. 7045-45, Contract AF19(626)-16, The Travelers Research Center, Inc.
3. Blackadar, A. K., 1963: "The Vertical Distribution of Wind in a Baroclinic Adiabatic Atmosphere Boundary Layer," Unpubl. Manuscript, Dept. of Meteorol., Pennsylvania State University.
4. Berkofsky, L. and E. A. Bertoni, 1960: Topographic Charts at One-degree Intersections for the Entire Earth, GRD Res. Notes No. 42, 43 pp., AFCRL, Bedford, Mass.
5. Bryan, J. G., 1964: "Short-range Hour by Hour Forecast of Temperature by Projecting the Characteristic Curve with Constants Fitted by Immediately Preceding Data," Unpubl. Manuscript, The Travelers Research Center, Inc.
6. Dyer, A. J., 1965: "The Flux-gradient Relation for Turbulent Heat Transfer in the Low Atmosphere," Quart. J. Roy. Meteorol. Soc., Vol. 91, No. 388, pp. 151-157.
7. Estoque, M., 1963: "A Numerical Model of the Atmospheric Boundary Layer," J. Geophys. Res., Vol. 68, No. 4, pp. 1103-1113.
8. Fisher, E. L., and P. Caplan, 1963: "An Experiment in Numerical Prediction of Fog and Stratus," J. Atmos. Sci., Vol. 20, No. 5, pp. 425-437.
9. Forsythe, G. and W. Wasow, 1960: Finite Difference Methods for Partial Differential Equations, J. Wiley, New York.
10. Gambo, K., 1963: "The Vertical Tilt of the Planetary Waves and its Time Change," J. Meteorol. Soc. of Japan, Vol. 41, No. 4, pp. 218-232.
11. —, 1963: "The Role of Sensible and Latent Heats in the Baroclinic Atmosphere," J. Meteorol. Soc. of Japan, Vol. 41, No. 4, pp. 233-245.
12. Gerrity, J. P., 1965: A Physical Model for the Prediction of Large-scale Low Cloudiness, Tech. Rpt. 7463-150, The Travelers Research Center, Inc.

13. Halstead, M. H., et al., 1957: "A Preliminary Report on the Design of a Computer for Micrometeorology," J. Meteorol., Vol. 14, No. 4, pp. 308—325.
14. Haurwitz, B., 1941: Dynamic Meteorology, McGraw-Hill Book Co., New York.
15. Kimbal, S. J., N. N. Richardson, and D. H. Frey, 1964: The Use of Diurnal Temperature and Dew-point Curves, Sci. Services Tech. Note 7, Headquarters 3D Weather Wing, Offutt Air Force Base, Nebraska.
16. Kung, E. C-T., 1963: Climatology of Aerodynamic Roughness Parameter and Energy Dissipation in the Planetary Boundary Layer over the Northern Hemisphere, Annual Report, Contract DA-36-039-AMC-00878, Dept. of Meteorol., University of Wisconsin.
17. Lettau, H. H., 1959: "Wind Profile, Surface Stress, and Geostrophic Drag Coefficients in the Atmospheric Surface Layer," Advances in Geophysics, Vol. 6, Academic Press, New York.
18. —, and B. Davidson, 1957: Exploring the Atmosphere's First Mile, 2 vols., Pergamon Press, New York.
19. Lumley, J. L. and H. A. Panofsky, 1964: The Structure of Atmospheric Turbulence, Interscience Publ., New York.
20. Marcus, B., 1964: A New Approach to the Numerical Solution of Wind Spirals, Meteorol. Res. Notes No. 6, Meteorol. Dept., USAERDA, Fort Huachuca, Arizona.
21. Matveev, L. T., 1964: "On the Formation and Development of Layer Clouds," Tellus, Vol. 16, No. 2, pp. 139—146.
22. McDonald, J. E., 1963: "The Saturation Adjustment in the Numerical Modeling of Fog," J. Atmos. Sci., Vol. 20, No. 5, p. 476.
23. Monin, A. S., 1958: "The Structure of Atmospheric Turbulence," (Translated by R. A. Silverman), Theory of Probability and its Appl., Vol. 111, No. 3.
24. Pandolfo, J. P., D. S. Cooley, and E. A. Newburg, 1963: Preliminary Investigations of Numerical Models for the Short-period Prediction of Wind, Temperature and Moisture in the Atmospheric Boundary Layer, Final Rpt. 7047-80, The Travelers Research Center, Inc.
25. Priestley, C. H. B., 1959: Turbulent Transfer in the Lower Atmosphere, The University of Chicago Press, Chicago.

26. Smagorinsky, J. and G. Collins, 1955: "On the Numerical Prediction of Precipitation," Mo. Weath. Rev., Vol. 83, pp. 53—68.

27. Sutton, O. G., 1953: Micrometeorology, McGraw-Hill Book Co., New York.

DOCUMENT CONTROL DATA - R&D		
(Security classification of title, body of abstract and indexing annotation must be entered when the overall report is classified)		
1. ORIGINATING ACTIVITY (Corporate author) The Travelers Research Center, Inc. 250 Constitution Plaza, Hartford, Connecticut 06103		2a. REPORT SECURITY CLASSIFICATION Unclassified
		2b. GROUP
3. REPORT TITLE A PHYSICAL LOW-CLOUD PREDICTION MODEL		
4. DESCRIPTIVE NOTES (Type of report and inclusive dates) Final Report, January-August, 1965		
5. AUTHOR(S) (Last name, first name, initial) Gerrity, Joseph P.		
6. REPORT DATE October 1965	7a. TOTAL NO. OF PAGES 135	7b. NO. OF REFS 27
8a. CONTRACT OR GRANT NO. AF19(628)-3437 (15107)	9a. ORIGINATOR'S REPORT NUMBER(S) 7463-182	
b. PROJECT NO. 1.0		
c. Task 1.2	9b. OTHER REPORT NO(S) (Any other numbers that may be assigned this report)	
d. Milestone 1.2.3	ESD-TR-65-476	
10. AVAILABILITY/LIMITATION NOTICES Availability Notice (1) and Legal Notice (1)		
11. SUPPLEMENTARY NOTES	12. SPONSORING MILITARY ACTIVITY Electronics Systems Division	
13. ABSTRACT A physical model for the prediction of large-scale low cloudiness [ESD-TR-65-3] was modified. Results of three 12-hour forecasts (for different synoptic situations), computed with the new model, are presented. Equations for the contact layer were derived for the forced convection, free convection, and strong inversion regimes. The requirement for upper boundary conditions is reduced; only the geostrophic wind components and upper-level cloudiness are required from a free-air model. Empirical methods were developed for computing the instrument shelter level temperature and relative humidity. The eddy diffusion coefficient for heat and water is a function of the Richardson number throughout the boundary layer. The linear geostrophic wind shear within the boundary layer is computed from the predicted temperature. The model has not been thoroughly tested: preliminary results suggest that, given a careful analysis of routine observational data, this boundary layer model will serve operationally-meaningful diagnostic and predictive functions. The logic used in constructing the computer program for the model is presented.		

14. KEY WORDS	LINK A		LINK B		LINK C	
	ROLE	WT	ROLE	WT	ROLE	WT
Numerical Prediction Model						
Low Cloud Prediction						
Boundary Layer Model						

INSTRUCTIONS

1. **ORIGINATING ACTIVITY:** Enter the name and address of the contractor, subcontractor, grantee, Department of Defense activity or other organization (*corporate author*) issuing the report.

2a. **REPORT SECURITY CLASSIFICATION:** Enter the overall security classification of the report. Indicate whether "Restricted Data" is included. Marking is to be in accordance with appropriate security regulations.

2b. **GROUP:** Automatic downgrading is specified in DoD Directive 5200.10 and Armed Forces Industrial Manual. Enter the group number. Also, when applicable, show that optional markings have been used for Group 3 and Group 4 as authorized.

3. **REPORT TITLE:** Enter the complete report title in all capital letters. Titles in all cases should be unclassified. If a meaningful title cannot be selected without classification, show title classification in all capitals in parenthesis immediately following the title.

4. **DESCRIPTIVE NOTES:** If appropriate, enter the type of report, e.g., interim, progress, summary, annual, or final. Give the inclusive dates when a specific reporting period is covered.

5. **AUTHOR(S):** Enter the name(s) of author(s) as shown on or in the report. Enter last name, first name, middle initial. If military, show rank and branch of service. The name of the principal author is an absolute minimum requirement.

6. **REPORT DATE:** Enter the date of the report as day, month, year, or month, year. If more than one date appears on the report, use date of publication.

7a. **TOTAL NUMBER OF PAGES:** The total page count should follow normal pagination procedures, i.e., enter the number of pages containing information.

7b. **NUMBER OF REFERENCES:** Enter the total number of references cited in the report.

8a. **CONTRACT OR GRANT NUMBER:** If appropriate, enter the applicable number of the contract or grant under which the report was written.

8b, 8c, & 8d. **PROJECT NUMBER:** Enter the appropriate military department identification, such as project number, subproject number, system numbers, task number, etc.

9a. **ORIGINATOR'S REPORT NUMBER(S):** Enter the official report number by which the document will be identified and controlled by the originating activity. This number must be unique to this report.

9b. **OTHER REPORT NUMBER(S):** If the report has been assigned any other report numbers (*either by the originator or by the sponsor*), also enter this number(s).

10. **AVAILABILITY/LIMITATION NOTICES:** Enter any limitations on further dissemination of the report, other than those

imposed by security classification, using standard statements such as:

- (1) "Qualified requesters may obtain copies of this report from DDC."
- (2) "Foreign announcement and dissemination of this report by DDC is not authorized."
- (3) "U. S. Government agencies may obtain copies of this report directly from DDC. Other qualified DDC users shall request through _____."
- (4) "U. S. military agencies may obtain copies of this report directly from DDC. Other qualified users shall request through _____."
- (5) "All distribution of this report is controlled. Qualified DDC users shall request through _____."

If the report has been furnished to the Office of Technical Services, Department of Commerce, for sale to the public, indicate this fact and enter the price, if known.

11. **SUPPLEMENTARY NOTES:** Use for additional explanatory notes.

12. **SPONSORING MILITARY ACTIVITY:** Enter the name of the departmental project office or laboratory sponsoring (*paying for*) the research and development. Include address.

13. **ABSTRACT:** Enter an abstract giving a brief and factual summary of the document indicative of the report, even though it may also appear elsewhere in the body of the technical report. If additional space is required, a continuation sheet shall be attached.

It is highly desirable that the abstract of classified reports be unclassified. Each paragraph of the abstract shall end with an indication of the military security classification of the information in the paragraph, represented as (TS), (S), (C), or (U).

There is no limitation on the length of the abstract. However, the suggested length is from 150 to 225 words.

14. **KEY WORDS:** Key words are technically meaningful terms or short phrases that characterize a report and may be used as index entries for cataloging the report. Key words must be selected so that no security classification is required. Identifiers, such as equipment model designation, trade name, military project code name, geographic location, may be used as key words but will be followed by an indication of technical context. The assignment of links, roles, and weights is optional.



